# Dissertation

submitted to the
Combined Faculties for the Natural Sciences and for Mathematics
of the Ruperto-Carola University of Heidelberg, Germany
for the degree of
Doctor of Natural Sciences

Put forward by
Diplom-Physikerin Eva Rittweger
born in Cologne

Oral examination: 16$^{\text{th}}$ December 2009

Maximizing far-field optical microscopy resolution through selected fluorophore transitions
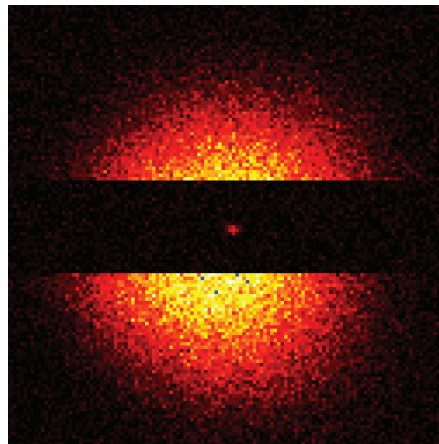
Referees: Prof. Dr. Stefan W. Hell
            Prof. Dr. Jürgen Wolfrum

Abstract:

Stimulated emission depletion (STED) microscopy and related nanoscopy techniques, which utilize a saturable optical transition between a bright and a dark state, overcome the diffraction barrier by confining one of the states to an area smaller than the Airy disk. Scanning this area across the specimen yields sub-diffraction images by registering inseparable fluorescent markers sequentially in time. Despite the progress made in nanoscopy so far, maximizing the resolution has been hampered by the efficiency of the utilized optical transition and the photostability of the fluorophores. Here, the optical transition responsible for breaking the barrier was studied in order to maximize its efficiency. For a range of fluorophores (dyes, proteins, quantum dots, color centers) the nature of the responsible process could be clarified. It was also investigated whether heat could serve as an imaging contrast to provide an alternative to fluorescence. This work demonstrates a resolving power of down to $6\,\text{nm}$ in unprocessed recordings, corresponding to $\lambda/135$, which is to date the highest obtained in far-field optics. These measurements, which show no sign of photobleaching or blinking, were performed with diamond color centers using STED and ground state depletion (GSD) microscopy.

Zusammenfassung:

Die STED- (engl. "stimulated emission depletion") Mikroskopie und verwandte Nanoskopie-Methoden, die einen sättigbaren optischen Übergang zwischen einem hellen und einem dunklen Zustand benutzen, überwinden die Beugungsgrenze, in dem sie einen dieser Zustände räumlich enger als die Beugungsgrenze einschränken. Überaufgelöste Bilder erhält man, indem man diesen Bereich über die Probe rastert und so benachbarte fluoreszienende Marker zeitlich sequentiell aufnimmt. Trotz vieler Fortschritte in der Nanoskopie war die Auflösung in der Anwendung beschränkt durch die Effizienz des verwendenten optischen Übergangs und die Photostabilität der Fluorophore. In dieser Arbeit wurde der optische Übergang, der die Überwindung der Beugungsgrenze ermöglicht, untersucht, um seine Effizienz zu steigern. Es konnte für eine Reihe von Fluorophoren (Farbstoffe, Proteine, Quanten-Dots, Farbzentren) die Frage des zugrundeliegenden Prozesses geklärt werden. Desweiteren wurde untersucht, ob sich Wärme als alternativer Bildkontrast zu Fluoreszenz eignet. Es wurde ein Auflösungsvermögen von bis zu $6\,\text{nm}$ in Rohdaten, entsprechend $\lambda/135$, erreicht, was die zur Zeit höchste Auflösung im Fernfeld darstellt. Diese Messungen, die weder Photobleichen oder Blinken aufweisen, wurden an Diamant-Farbzentren durchgeführt unter Anwendung der STED- und der GSD- (engl. "ground state depletion") Mikroskopie.

Contents

Abbreviations

1D	one-dimensional
2D	two-dimensional
3D	three-dimensional
AC	alternating current
A.D.	anno Domini
B.C.	before Christ
CVD	chemical vapour deposition
CW	continuous wave
Exc	excitation
Eff	effective
DC	direct current
Φ_{STED}	photon flux density in the depletion focus
$\widehat{\Phi}_{\mathrm{STED}}$	photon flux density per laser pulse in the depletion focus
FWHM	full width at half maximum
GSD	ground state depletion
GSDIM	ground state depletion followed by individual molecule return
h_{c}	confocal point spread function
h_{exc}	excitation point spread function
h_{det}	detection point spread function
I_{STED}	maximum intensity in the depletion focus
$I_{\mathrm{STED}}(x)$	intensity near the depletion focus at position x
k_{fl}	decay rate for spontaneous emission ($k_{\mathrm{fl}} = 1/\tau_{\mathrm{fl}}$)
λ_{STED}	wavelength of the STED beam
λ_{exc}	wavelength of the excitation beam
η	fluorescence suppression by STED
NA	numerical aperture of a lens
NV	nitrogen vacancy
NV^{-}	negatively charged nitrogen vacancy
NV^{0}	neutral nitrogen vacancy
PALM	photoactivation localization microscopy
PSF	point spread function
RESOLFT	reversible saturable optical (fluorescence) transitions
SNR	signal to noise ratio

SPEM	saturated pattern excitation microscopy
STED	stimulated emission depletion
STORM	stochastic optical reconstruction microscopy
σ_em	stimulated emission cross section
σ_esa	excited state absorption cross section
τ_fl	fluorescence lifetime
Ti:sapphire	Titanium-Sapphire
UV	ultraviolet (light)

Chapter 1

Introduction

The fascination to visualize the world of the small goes back to the time of ancient Greece and Rome. Aristophanes, who lived in the 4th century B.C., described globules of glass called burning spheres. In the first century A.D. Seneca, wrote about the magnification of letters through a transparent globe filled with water. However, if a microscope is considered to be an instrument with which one can observe objects which are too minute to be visible to the naked eye, then the microscope is a comparatively modern invention. In 1590 the Dutch lens grinders Hans and Zacharias Janssen built the first compound microscope by placing two lenses in a tube. Several technical innovations in the 18th century e.g. achromatic lenses made microscopes better and easier to handle. Ever since, the microscope has been an important tool in the life science, material science, and other fields. For example the analysis by Albert Einstein [1], which lead to the empirical evidence for the existence of atoms, was founded on the observation of Brownian motion of pollen in water by optical microscopy.

A major milestone in microscopy was due to Ernst Abbe who formulated the first comprehensive theoretical description of optical image formation. In 1873, he published his landmark paper that connected the microscope resolution Δr with the wavelength of light λ [2]:

$$\Delta r = \frac{\lambda}{2\,\mathrm{NA}},\tag{1.1}$$

with r being a lateral direction and $\mathrm{NA} = n\sin\alpha$ the numerical aperture of the optical system with a refractive index n and half opening angle α.

This formula calculates the resolution limit of a light microscope as dictated by the wave nature of light. Due to diffraction, the smallest lateral spot size is about $200\,\mathrm{nm}$ for visible light. Because the resolution scales with the wavelength, ultraviolet (UV) light is favorable in terms of high resolving power. Electron matter waves have even smaller wavelengths due to the higher electron mass. However, in electron microscopy, the limiting factor for the resolution is often given by the quality of the electron optical system, which is hampered by aberrations, still allowing resolutions of down to a few nanometers. Ernst Ruska

and Max Knoll built the first electron microscope in 1932 [3]. Despite the high resolution, electron microscopy has many disadvantages: electrons interact more strongly with the specimen, it has limited 3D capability, it is mainly used under vacuum conditions, requires complicated sample preparation, and specific molecular labeling as well as multi-color staining is very limited. For these reasons light microscopy is still the most extensively used microscopy technique in the life sciences.

In 1928 a different approach to extend the resolution was described for the first time [4]: work in the near-field optical regime rather than in the far-field. Synge suggested to direct the light field through a tiny aperture which is smaller than the wavelength. If an object is placed at a distance to the aperture also smaller than the wavelength, the resolution is not limited by the wavelength but by the size of the light source. This was realized for the first time in an aperture scanning microscope with microwaves yielding a resolution of $\lambda/60$ in 1972 [5]. Later it was also implemented for visible light described in two papers in 1984 [6, 7]. It is technically very challenging to work in the near-field regime and one is restricted to surface studies. The resolution of other raster scanning methods like scanning tunnel microscopy or scanning force microscopy is given by the size of the scanning probe and its interaction with the sample, which can be of atomic size. These instruments however have similar restrictions as the optical near-field technique.

The first far-field optical microscopy technique which truly overcame the diffraction limit (1.1) was stimulated emission depletion (STED) microscopy [9]. Since its invention in 1994 this method has been developed into a powerful tool for biological imaging. It has been shown to work under live cell conditions [10], in three dimensions deep inside the specimen [11], with video-rate recording [12] as well as with two-color staining [13] combining the advantages of light mi-
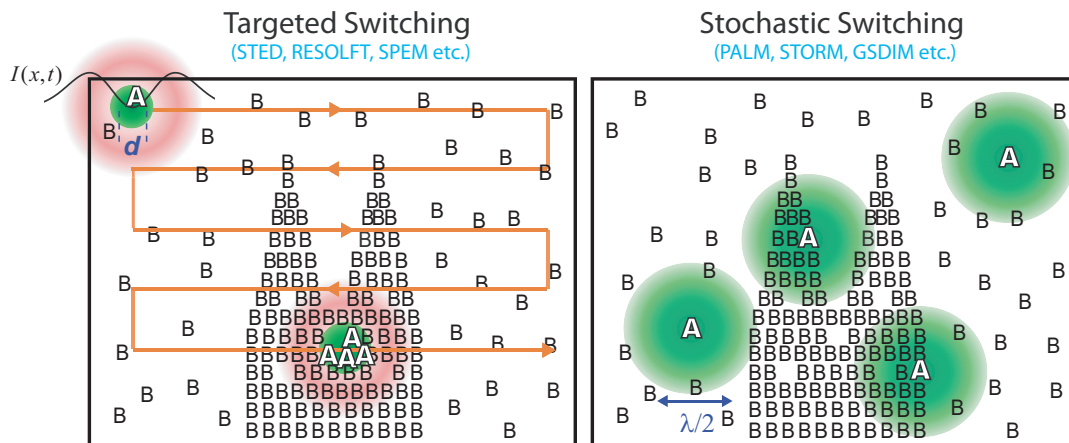

Figure 1.1: Read-out schemes of nanoscopy techniques. B refers to a non-detectable state of the marker and A to a detectable state. In both schemes it is ensured that the fluorescence can be attributed to an area smaller than the Airy disk [8].

croscopy with a resolution down to 20-80 nm. Besides STED microscopy several other nanoscopy concepts [14, 15, 16, 17, 18, 19] have been reported which all rely on targeted or stochastic read-out to separate markers within a diffraction spot by toggling them from a non-detectable (non-fluorescent) B to a detectable (fluorescent) state A. The crucial point behind these nanoscopy techniques is that one cannot change the wave nature of light, but it is possible to make sure that markers at a distance closer than the diffraction limit are recorded at different points in time. Therefore it is guaranteed that the detected fluorophores, whose image is also diffraction limited, can be attributed to a spot smaller than the Airy disk. In this manner an optical resolution beyond the diffraction limit is obtained. In Figure 1.1 the two different detection modes are contrasted with each other [20, 8].

The power of STED microscopy to achieve high resolutions of $\lambda/23$ in the axial direction [21] and about $\lambda/50$ in a lateral direction [22] had been shown in the past. The aim of this work was to investigate strategies to improve the optical resolution beyond the previous efforts. For achieving this goal it is essential to understand the photophysics of the light-driven transition between the states A and B. As presented in the second chapter, pump-probe spectroscopy of this transition was carried out to study the underlying photophysical mechanisms for several fluorophores used in STED/RESOLFT microscopy to clarify the question which process is responsible for the transition. In the third chapter, heat in contrast to fluorescence was investigated to serve as an imaging contrast. The question of whether the states A and B could be an absorbing and a non-absorbing state rather than fluorescent and non-fluorescent is addressed. The heat produced by absorption was used as a contrast by detecting the change in refractive index due to the temperature change. In the fourth chapter it is shown that imaging of diamond color centers with nanometric resolution is possible by STED as well as ground state depletion (GSD) microscopy. An almost text book like implementation of STED and GSD has been realized with the highest resolving power of 6 nm obtained so far in the optical far-field corresponding to $\lambda/135$.

Chapter 2

Mechanisms for fluorescence switching in nanoscopy

All super-resolution microscopy techniques, that have been successfully implemented and applied so far, utilize a definite transition between a dark and a bright state. The goal of the work presented in this chapter was to study the photophysics behind these transitions to build a solid foundation for their understanding.

2.1 Motivation

STED microscopy has been developed over the last decade into a powerful tool for optical imaging, providing spatial resolution well beyond the diffraction limit. This is achieved by employing a diffracted, focused laser beam that excites the fluorescent molecules in the sample. A second red-shifted beam with a doughnut-shaped intensity profile withdraws the molecules' ability to fluoresce in the periphery of the focal spot, allowing only the molecules in the very center to contribute to the image. Hence the effective spot size is smaller than the Airy disk.

To increase the resolution of the microscope the efficiency of this process is essential. To find ways and means to improve this efficiency, it is important to understand the underlying mechanism. Many spectroscopic studies of laser dyes and biological fluorescent markers support that the de-excitation process is realized via stimulated emission [23, 24, 25, 26, 27]. However, the photophysics of such dyes, as applied to fluorescence inhibition in microscopy, has been still controversial.

Several papers [28, 29, 30, 31] have proposed an alternative process, termed up-conversion, by which the excited molecules are quenched by the doughnut-shaped beam: the molecules are further excited from S_1 to higher excited singlet states S_n, from which they relax non-radiatively to S_1 via vibrational relaxation or internal conversion. If several photons are absorbed by the same molecule during the second pulse, the molecule can be excited from S_1 several times, each time
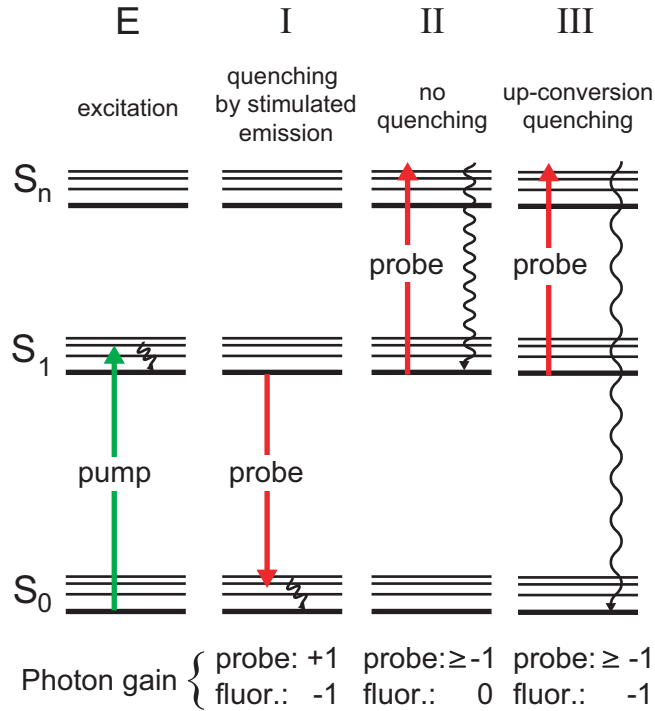
Figure 2.1: Jabłonski Diagram showing three different possible transitions caused by interaction of the probe pulse after excitation (E): (I) Quenching by stimulated emission; (II) up-conversion without fluorescence quenching; (III) up-conversion with fluorescence quenching. Bottom: gain and loss of photons in probe beam and fluorescence light.

relaxing back to S_1 vibrationally and dissipating heat into its local environment [32]. This heating could lower the quantum efficiency of the dye (e.g. by 10% for Rhodamine 6G for $\Delta T = 40°C$ [33]), causing it to relax non-radiatively to S_0 via internal conversion. It was proposed that in this manner the fluorescence is quenched [34, 35].

To clarify the question of which process, whether stimulated emission or up-conversion, is dominant in the quenching of fluorescence for different fluorophores used in super-resolving microscopy, a pump-probe technique was used. Both the fluorescence quenching and the change in number of photons in the probe beam was simultaneously measured. This allows one to distinguish between the possible dominant transitions which may be driven by the probe pulse after the molecules have been excited to the S_1 level. Figure 2.1 shows the possible processes and how they would affect the two signals. Process (I), stimulated emission, would increase the number of photons in the probe beam and reduce the fluorescence signal. Process (II), excitation to higher levels and internal conversion to S_1, would remove a photon in the probe beam, but the fluorescence signal would

not be affected since the molecule quickly ($< 3\,\mathrm{ps}$) returns to the S_1 state. The last process (III), excitation to higher levels and internal conversion to S_0, would reduce both signals.

Processes (I) and (III) would lead to fluorescence quenching. In order to break the diffraction barrier a strong, saturated transition is required. Process (II) opens a possible channel for bleaching which is disastrous for resolution enhancement and image quality. As the up-conversion process would be a combination of multiple excited state absorption (II) and process (III), it is possible to discriminate the two possible depletion mechanisms clearly from one another by considering whether photons are gained or lost in the probe beam.

2.2   Pump-Probe Setup

In Figure 2.2 a schematic diagram of the experimental setup is depicted. The white-light spectrum of a supercontinuum fiber laser (Fianium, Southampton, UK) was divided by a dichroic mirror into the spectral regions A and B (see figure 2.2), from which the wavelengths for the pump and probe beams were selected using interchangeable bandpass filters (bandwidth $10\,\mathrm{nm}$; AHF Analysentechnik, Tübingen, Germany). The pulse lengths were between 100-200 ps with longer pulses in the red part of the spectrum. The pulse repetition rate was $40\,\mathrm{MHz}$. This design allows flexible measurements of different dyes over the whole visible range. Recombined by a second identical dichroic mirror, the two collinear beams were focused into the cuvette containing the dye solution where the two foci superimpose. The timing between the two pulses was controlled by a linear translation stage (Owis, Staufen, Germany).

Two measurements were performed: the reduction of fluorescence and the change in the number of photons in the probe beam. In each case a small change in the signal had to be discriminated from the baseline signal. Therefore a lock-in amplifier (Model 7265, Signal Recovery, Wokingham, United Kingdom) was used for noise reduction in both cases [36]. A description of the principle behind the lock-in detection can be found in Appendix A. For measuring the change in the number of photons in the probe and the fluorescence quenching, a beam chopper was placed in the excitation and the probe beam paths respectively. To eliminate the noise due to laser power fluctuations, the probe beam was detected with an auto-balanced detector (Nirvana detector, New Focus, San Jose, USA) in comparison to a reference beam from the laser.

For both measurements one has to consider the background signals. In the gain measurements, some fluorescence is inevitably detected which cannot be filtered out since the wavelength of the probe pulse lies within the emission band of the dye. Second, for the fluorescence quenching, an additional background can arise due to excitation induced by the probe beam. To separate the signal of interest from background, it was measured while the probe pulse came ahead of the pump pulse. This configuration ensured that no excited molecules were present
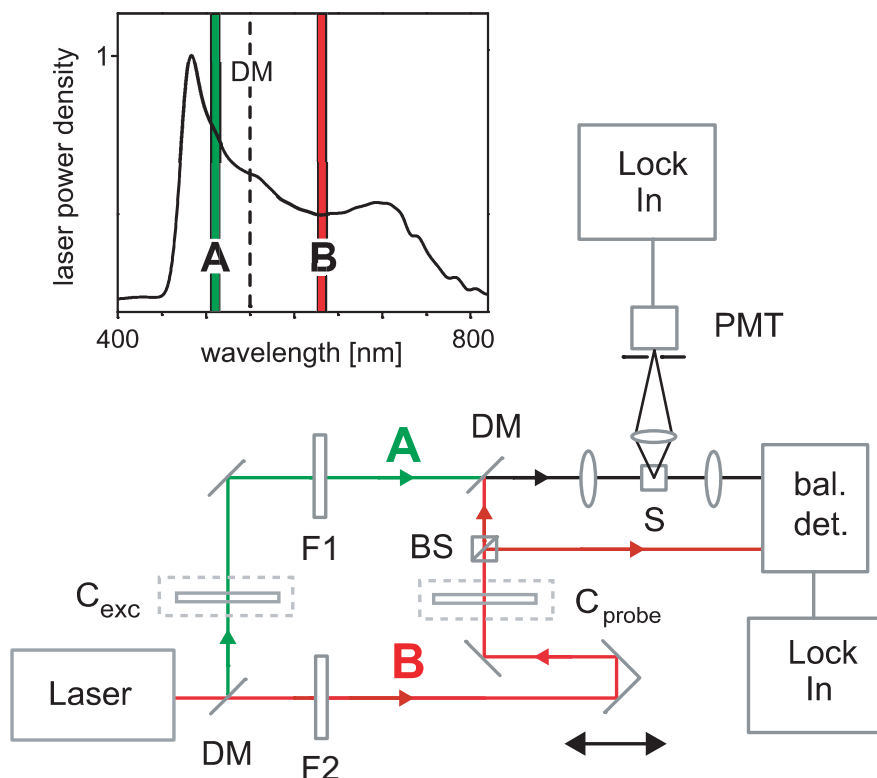
Figure 2.2: Laser spectrum and setup; A: pump beam, B: probe beam, DM: dichroic mirror, F1/F2: bandpass filters, C_{exc}: chopper position for measuring the change in the number of photons in the probe beam, C_{probe}: chopper position for fluorescence quenching measurement, S: cuvette with dye solution, bal. det.: balanced detector, BS: beam splitter.

by the time the probe pulse arrived. In this manner the pure background signal was measured. In order to ensure a defined detection volume, the fluorescence signal was imaged onto a pinhole in front of the detector. Thus the measurement was restricted to the region with the highest concentration of quenched molecules, which is the focus, the area of high light intensity and high density of excited molecules. A magnetic stirrer was used to exchange the dye solution in the focal volume. This ensures that the concentration of potentially bleached molecules or molecules in the triplet state can be neglected.

2.3   Results

2.3.1   Fluorescent markers: dyes, proteins, quantum dots

The two signals and their wavelength dependence were measured for eight fluorescent dyes covering different dye families used in STED microscopy: the xanthenes Rhodamine 6G and ATTO 532, the acridine dye ATTO 495, the carbopyronine

derivative ATTO 647 N, the styryl dye Pyridine 2 as well as three fluorescent proteins which are used for many biological applications: EGFP, EYFP and DsRed. ATTO 532 was used for many STED applications in the visible range [37, 38]. EGFP and EYFP were recently used for the first time in a STED microscope [39]. The concentration of the dye solutions was about 200 μM. The different solvents used are given in Figure 2.3. The fluorescent proteins were expressed in Escherichia coli strain HMS 174 (DE3) using the expression plasmids pRSETa-EGFP, pRSETa-EYFP and pRSETa-DsRed. Cells expressing the protein were disrupted by Lysozym treatment and sonication. For the presented measurements the whole protein extract was used.

The fluorescence was quenched upon switching on the probe pulse, which is consistent with observations applying the STED technique. Furthermore, photons were always gained in the probe beam, proving that stimulated emission is the dominant process.

Further tests were performed which are consistent with the STED mechanism: The temporal evolution of fluorescence quenching and signal gain were identical and matched the fluorescence decay of the dye. Secondly, the anisotropy of both the fluorescence emission and STED gain were found to coincide with the rotational correlation time, thus proving that the signal depends on the orientation of the dipole moment of the molecules to the polarization axis of the light. Both signals depended linearly on the power of the pump and the probe beam as expected when measuring far away from saturation.

It would be preferable to analyze the two signals in absolute terms, i. e. to compare the number of photons lost in fluorescence and gained in the STED beam. This is difficult to achieve because it must be ensured that the detection volume for both measurements is identical. This is not easily realizable experimentally and is subject to high uncertainties. Furthermore, the detection efficiencies are not exactly known and even vary for different measurements. Therefore both signals were measured relative to their unperturbed values (which is the signal from the total probe beam for the photon gain measurement and the full fluorescence signal in case of the quenching measurement). The detector efficiencies, especially the wavelength dependence of the two detectors, the PMT and the balanced detector, therefore cancel out.

These relative measurements were performed for various wavelengths of the probe beam. In this way the experimental conditions remain constant, while the signal strength varies with the wavelength-dependent cross section. The only correction needed is to account for the different focal spot size of each wavelength of the probe beam. For this correction, the beam waists were measured with the knife-edge method [40].

If stimulated emission were the quenching process, the spectral dependence of the fluorescence quenching would follow that of the cross section of stimulated emission σ_{em}. Two effects contribute to the signal change of the probe beam: stimulated emission σ_{em} and excited state absorption σ_{esa}. Thus the gain signal
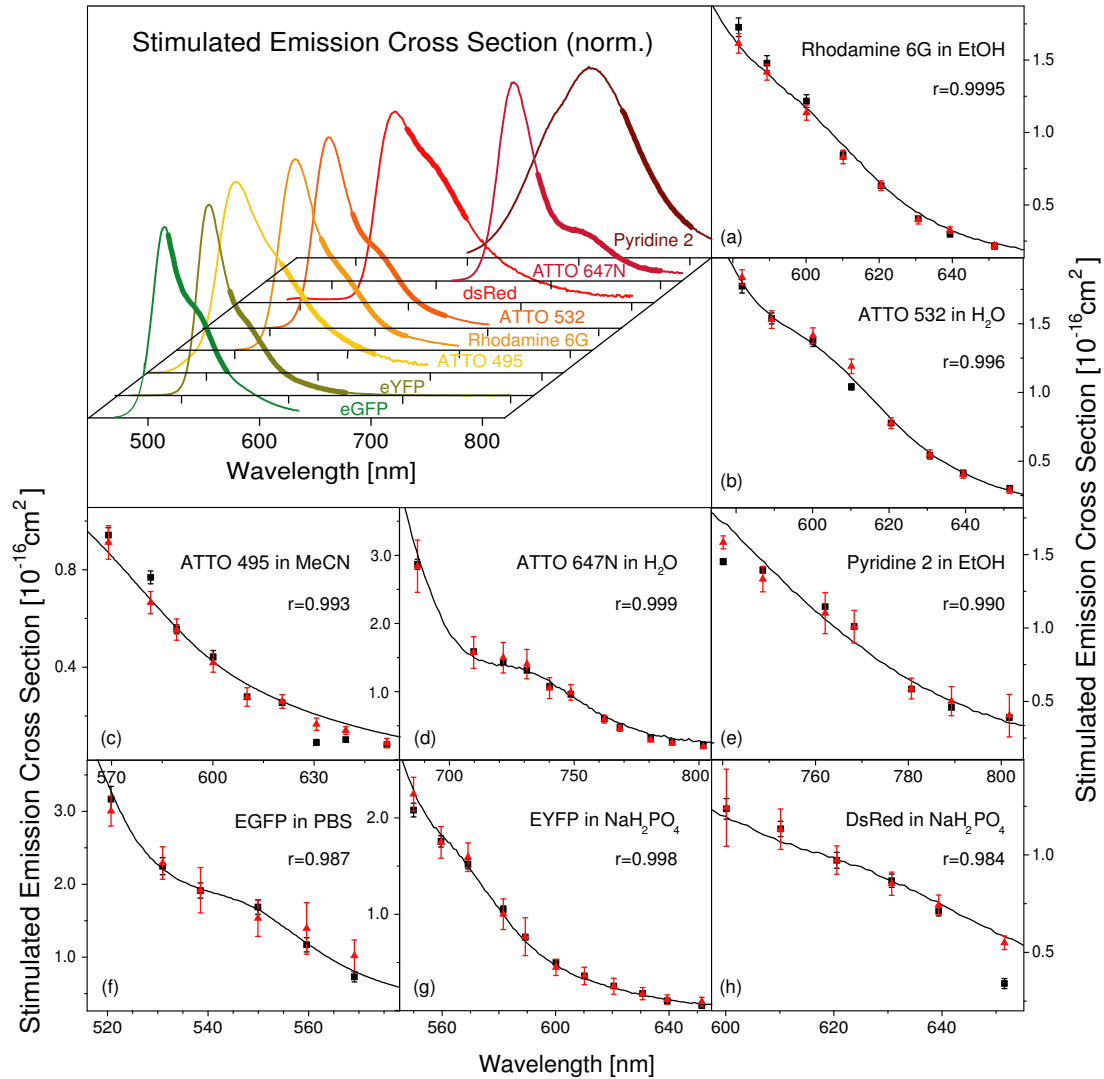
Figure 2.3: Above left: Normalized stimulated emission cross section for seven different dyes; the bold parts mark the areas which are shown in detail (a)-(h): stimulated emission cross section (thin line), relative measurement of STED gain (■, black) and fluorescence quenching (▲, red) and the values of their correlation. The results agree very well with each other which proves that stimulated emission is the dominant process for fluorescence quenching.

is proportional to the difference of the two cross sections:

$$P_{\text{probe}} \propto (\sigma_{\text{em}} - \sigma_{\text{esa}}). \tag{2.1}$$

Only in the case of a vanishing amount of excited state absorption does the gain signal follow the spectral dependence of σ_{em}, given by [23]:

$$\sigma_{\text{em}}(\lambda) = \frac{\lambda^4 E(\lambda)}{8\pi c n^2 \tau}, \tag{2.2}$$

with c the speed of light in vacuum, n the refractive index and τ the lifetime of the excited state S_n. This expression can be understood from the difference between the Einstein coefficients for spontaneous and stimulated emission. A derivation of this expression can be found in Appendix C.

The line shape function $E(\lambda)$ was determined from the measured fluorescence emission spectrum for the different dye solutions ($Q = \int E(\lambda)\,d\lambda$, where Q is the quantum efficiency). The wavelength dependence of the employed spectrometer (Cary Eclipse, Varian, Palo Alto, USA) was taken into account. The result for every dye is depicted in Figure 2.3 (thin line).

The results from the pump-probe measurements are also depicted in the same figure. To associate a wavelength position for each data point, the weighted mean of the transmission of each filter was determined. The results show that the fluorescence quenching (▲, red) and the STED gain (■, black) have the same wavelength dependence for each dye within the accuracy of the measurement. Moreover, both follow the curve for the stimulated emission cross section. A strong correlation between the STED gain, the fluorescence quenching and the stimulated emission cross section was found. The three pairwise correlations were determined resulting in Pearson correlation coefficients between 0.973 and 0.9995 with a median of 0.997.

These results are in very good agreement with the assumption that stimulated emission is responsible for the fluorescence quenching and that there is no substantial portion of excited state absorption. A similar outcome was obtained for laser dyes by a spectroscopic study of rhodamines [41]. If there is excited state absorption, the wavelength dependence must follow that for stimulated emission, which would be extremely coincidental, or the cross section for the S_1-S_n transitions must be very small to be consistent within the accuracy of the measurement. A small probability of excited state absorption is essential for a good STED dye to minimize bleaching via higher excited states.

From the fact that we always observe a positive signal change in the probe beam and from equation (2.1), the conclusion can be drawn that $\sigma_{\text{em}} > \sigma_{\text{esa}}$. Because the up-conversion process is a cyclic-multiphotonic absorption process, many absorbed probe photons are needed to bring one excited molecule back to S_0. Using an upper limit, one can assume that $< 10\%$ of the molecules undergoing excited state absorption return radiationlessly to the ground state [31]. For the limiting case that both cross sections for stimulated emission and excited state

absorption are equal, which would mean that 50% of the molecules which are effected by the probe beam undergo stimulated emission and the other half excited state absorption, at maximum 5% of these affected molecules would be quenched by an up-conversion process which would be 9% of all quenched molecules. That means, even for this limiting case, stimulated emission is the dominant process. Considering the good agreement of the measured data with the values for the stimulated emission cross section, a more realistic ratio for the cross sections would be $\sigma_{esa}/\sigma_{em} < 10\%$. From these numbers it follows that more than 99% of the quenched molecules are quenched by stimulated emission.

Mn-doped ZnSe quantum dots

Even though stimulated emission is definitely responsible for the fluorescence quenching in the case of fluorescent dyes and proteins, it does not mean that up-conversion quenching mechanisms do not exist. Even though one had believed that it is impossible to quench the fluorescence of quantum dots (QDs) through stimulated emission because of their overlapping excitation and emission spectra [42], it was demonstrated that special Mn-doped ZnSe quantum dots show fluorescence quenching via a second red-shifted laser beam. Detailed information about the properties of these quantum dots can be found in Appendix B. This inhibition process is efficient enough to implement sub-diffraction imaging of these QDs [43]. Because of their pronounced Stokes shift, it was suspected that this mechanism is based on stimulated emission. However, even for depletion wavelengths far away from the emission spectrum, fluorescence quenching is still observed.

To determine the responsible photophysical mechanism, a pump-probe measurement similar to the one described before was carried out. The same setup as described in section 2.2 was used with a 405 nm laser diode (PicoQuant, Berlin, Germany) for the excitation. Again the spectral dependence of the change in signal in the probe beam as well as the fluorescence quenching was measured. The sample consisted of a concentrated solution of the Mn-doped quantum dots (20 μM in toluene) to ensure adequate signal level.

For the whole spectral region from 470-800 nm, a loss in the probe beam was observed clearly indicating that excited state absorption (ESA) processes dominate.

These losses in the white light continuum probe are converted to units of ESA cross section σ_{esa} using the following formula:

$$P_t = P_i \exp(-\sigma_{esa} c_N l), \tag{2.3}$$

where P_t is the power transmitted through the sample, P_i is the input power, c_N is the concentration of excited quantum dots, and l is the effective path length.

This formula is rearranged to solve for σ_{esa}:

$$\sigma_{\text{esa}} = \frac{\ln(P_{\text{t}}/P_{\text{i}})}{c_{\text{N}}l}. \tag{2.4}$$

The difference between input power and transmitted power can be expressed as an infinitesimal quantity $P_{\text{t}} = P_{\text{i}} - \Delta P$ which allows equation 2.4 to be simplified according to a Taylor series expansion of the natural logarithm function:

$$\sigma_{\text{esa}} = \frac{\Delta P}{P_{\text{i}}c_{\text{N}}l}. \tag{2.5}$$

The concentration of excited quantum dots c_{N} within the focal volume of the excitation beam is estimated from the intensity of the excitation radiation, the absorption cross section of the quantum dots, and their fluorescence lifetime, while the interaction length l is taken to be the Rayleigh range of the excitation beam.

The spectral dependence of the fluorescence quenching was also measured to compare it to the ESA spectrum. Here the fluorescence signal was filtered before detection (60 nm band-pass centered at 575 nm, AHF Analysentechnik) to eliminate large amounts of scattered light, which also limited the spectral measurement range to 630-800 nm. Below 545 nm, a large fluorescence signal overwhelmed the ESA signal, which is believed to stem from transient population of the $^6\text{A}_1$ level. The results of the relative fluorescence change are shown in Figure 2.4 along with the results of the ESA measurement and indicate that fluorescence
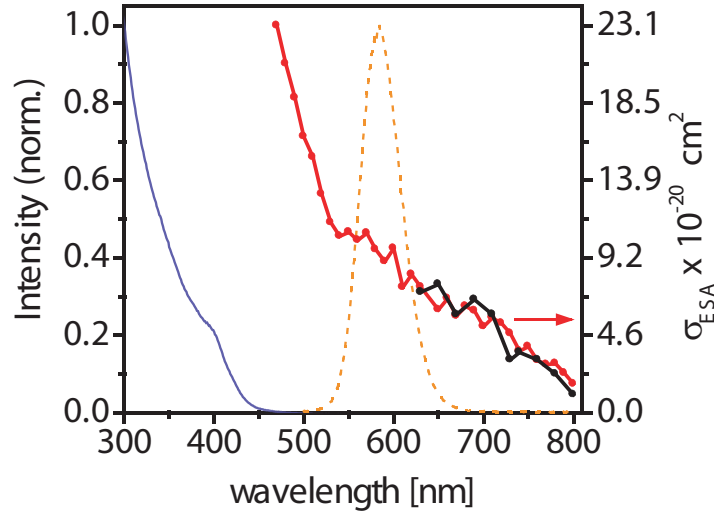

Figure 2.4: Absorption (solid blue line), emission (dotted orange line), and ESA spectra (red line and circles, right vertical scale) as well as the relative measurement of fluorescence quenching of the Mn-QDs (black line and circles). Note that for the fluorescence quenching and ESA follow the same spectral dependence while the ones for fluorescence and ESA are clearly distinct from each other.

depletion follows the ESA. This provides strong evidence that the fluorescence depletion results from ESA transitions originating from the $^4T_1$ upper fluorescent state.

The value of the excited state absorption cross section $\sigma_{esa} = 6.1 \cdot 10^{-20} \, cm^2$ (at 676 nm) shown in Figure 2.4 compares well with the estimated value from the depletion curve measured at 676 nm for previous RESOLFT measurements $\sigma_q = 2.1 \cdot 10^{-20} \, cm^2$ [43] and those determined for other Mn^{2+} ion/host systems [44]. The fact that σ_{esa} and σ_q have the same order of magnitude indicates that a significant amount of electronic cycling does not occur.

A time-correlated single-photon counting module (Picoquant, Berlin, Germany) was used to determine the fluorescence lifetime of the QDs. The data from this experiment can be found in Appendix B where it is observed that the fluorescence decay is multi-exponential. A triple exponential fit to the data and indicates three decay regimes of $2 \, \mu s$, $21 \, \mu s$, and $90 \, \mu s$. This long lifetime, which is about four to five orders of magnitude longer than that of a typical dye molecule, yield a stimulated emission cross section which is smaller by the same order of magnitude according to expression (2.2). From this assessment it can be concluded that the stimulated emission cross section is smaller than the excited state absorption cross section determined above which is in agreement with the fact that excited state absorption processes dominate the transition.

2.3.2   NV color center in diamond

Besides fluorescent dyes and proteins as well as semiconductor nano crystals, there are other fluorescent systems: color centers inside a solid state host. They originate from crystal defects – impurities, vacancies and complexes – which create electronic energy levels within the bandgap. There are more than 500 different defect centers in diamond [45]. The nitrogen vacancy (NV) center is the most popular and the most intensively studied color center in diamond. It is present
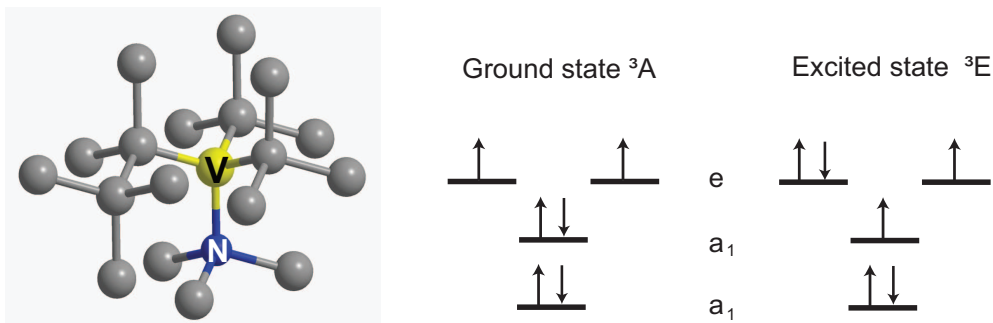

Figure 2.5: Left: An NV color center consists of a substitution nitrogen atom next to a charged vacancy inside the diamond lattice which is built out of carbon atoms (gray spheres). Right: Electron configuration for the triplet ground and excited state of the NV^- center.

even in natural diamond where nitrogen is the most common impurity [46]. The NV center stands out due to several remarkable properties: it is bright (single centers can be observed at room temperature), it is extremely photostable and the optical transition is driven from a ground triplet state, whose spin states can be polarized and detected optically. For theses reasons NV centers are explored for numerous applications e.g. as single photon sources for quantum cryptography [47], as Q-bits for quantum computation [48], as sensitive magnetic sensors [49, 50] or as marker for bioimaging in the form of nanocrystals [51, 52].

Structure and optical properties

A NV center comprises a substitution nitrogen atom next to a vacancy (Fig. 2.5) and forms a molecular like system inside the crystal. It exists in two charge states: neutral (NV^0) and negatively charged (NV^-) [53]. If not indicated otherwise, the expression NV refers to the negatively charged form. The first fluorescence spectrum was published in 1971 [54] and the optical transition was identified in 1976 to be likely due to the NV defect center [55]. Despite this early discovery and ongoing studies, the electronic structure has still not been definitively determined.

The model accepted today draws upon many theoretical and experimental studies and is consistent with the observed data [57]. Six electrons occupy the dangling bonds associated with the vacancy complex. The symmetry is trigonal because of the substitution nitrogen, which yields, in C_{3v} notation, two a_1 and one e orbitals. With six electrons the $a_1^2 a_1^2 e^2$ is the lowest energy configuration (see Figure 2.5). This can also be described as an e^2 hole system. The spin-orbit
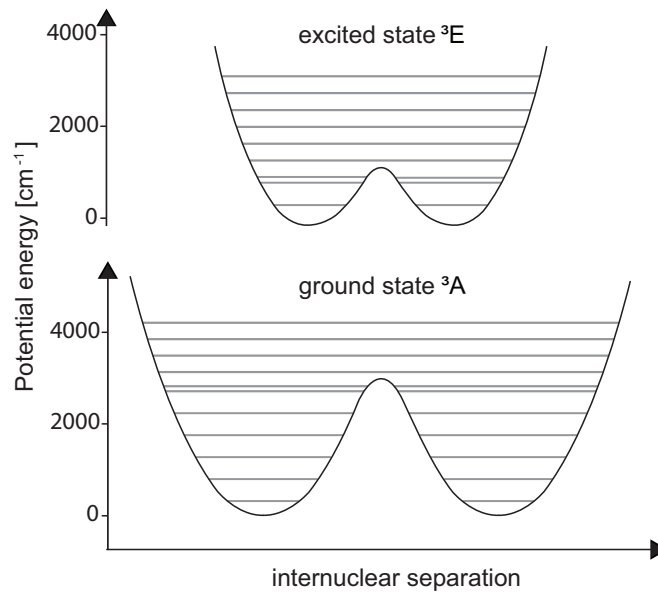

Figure 2.6: Double well potential and vibronic levels of the NV center according to [56].
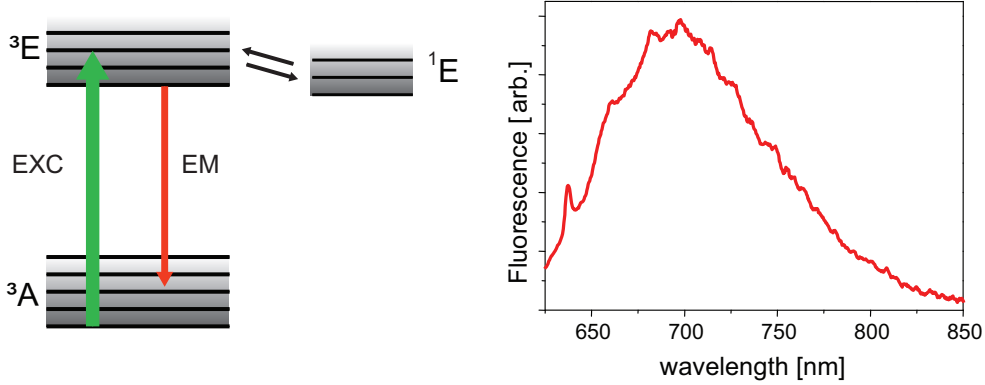
Figure 2.7: Left: Energy diagram of NV center in diamond with the triplet ground state (^{3}A) and the fluorescent state (^{3}E) along the the dark singlet state (^{1}E) and the transitions of excitation (EXC) and emission (EM). Right: Fluorescence spectrum of a single center with zero phonon line (ZPL) at 637 nm.

wave functions for the e^2 configuration give ^{3}A, ^{1}A and ^{1}E states, the ea_1 gives ^{3}E and ^{1}E states and the a_1^2 configuration an ^{1}A. The optical transition is associated to triplets. Therefore the ground state is attributed to the ^{3}A (e^2) state and the excited state to the ^{3}E (ea_1) state. The singlets ^{1}A (e^2), ^{1}E (e^2) and ^{1}E (ea_1) could lie in the same energy range as the triplets. Sometimes ^{1}A as well as ^{1}E are referred to the dark singlet state.

Absorption at 532 nm elevates the NV center from its ground (^{3}A) state to the excited state (^{3}E) of $\tau = 11.6$ ns lifetime, which emits at 600-850 nm virtually without bleaching or blinking (Figure 2.7). In Figure 2.6 a schematic diagram of the potential is shown. It is a double well potential with almost harmonic potentials around the equilibrium positions of the nitrogen and vacancy lattice sites [56]. The vibronic levels are equidistant and the level close to the potential barrier has a small splitting like in ammonia. Due to the shifted equilibrium position of the excited state, the transition probability for excitation is higher for higher vibronic levels of the excited electronic state. This is the Franck Condon principle. Due to vibronic coupling, the system relaxes to the lowest vibronic state of (^{3}E) from which fluorescence occurs as in case of fluorescent dye molecules yielding a strong Stokes shift. The emission spectrum is continuous due to coupling to lattice phonons.

Centers with magnetic quantum number $m_s = 0$ show about 30% higher fluorescence signal than their $m_s = 1$ counterparts, because centers with $m_s = 1$ have an increased tendency to convert into a dark singlet state (^1E). This feature allows the detection of the spin state by optical means. Furthermore, the probability is high that the center is coming back from the singlet state to $m_s = 0$. This means that after serveral excitation cycles the center is in the $m_s = 0$ state. Therefore it is possible to polarise the center in $m_s = 0$ by illumination [58].

Much of the fundamental work has been performed on native color centers in either single-crystal or nanodiamond particles. Native samples have the dis-

advantage that the concentration as well as the position of color centers cannot be controlled. It is possible to produce NV centers by radiating nitrogen rich diamond (Type Ib) with for example protons. Annealing treatment leads to migration of vacancies which form together with nitrogen defects NV centers which concentration can be regulated by several parameters like for example irradiation dosage and annealing time. Controlled Implantation of nitrogen ions into diamond crystals with low nitrogen concentration (Type IIa) allows to produce patterns of color centers [59, 60] which are a requirement for quantum computing applications.

Fluorescence quenching in NV centers

Due to their remarkable properties NV color centers are very interesting fluorescent systems. However, to be able to apply them to sub-diffraction imaging, their fluorescence has to be controllable by light. Therefore the first step was to investigate the ability of fluorescence inhibition through an optical transition.

To measure the depletion behavior of the NV centers an existing setup was used (courtesy of K. Y. Han). A CW laser (Verdi, Coherent Inc., Santa Clara, CA, USA) at $532\,\mathrm{nm}$ served as the excitation source, which was combined by a dichroic mirror with a CW Titanium sapphire laser (Mira, Coherent Inc., Santa Clara, CA, USA). The two beams were focused into the diamond crystal by an oil immersion lens (NA=1.4, Leica mircosystems, Wetzlar, Germany) which also collected the fluorescence signal detected by a single photon counting device (Perkin Elmer, Waltham, MA, USA).

Figure 2.8 shows the fluorescence signal of a single NV color center recorded with an excitation intensity $I_{\mathrm{exc}} = 8.5\,\mathrm{kW/cm^2}$ and a depletion intensity of $I_{\mathrm{STED}} = 6.5\,\mathrm{MW/cm^2}$ at $770\,\mathrm{nm}$. The red beam was toggled on/off every 30 data aquisitions which resulted in dark regions when it was on, which shows se-
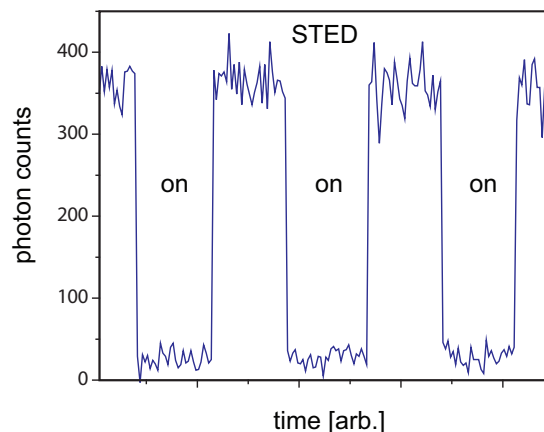

Figure 2.8: Fluorescence signal of a single NV center with and without STED. The dark regions demonstrate the capability to actively and reversibly control fluorescence emitted from the NV center.
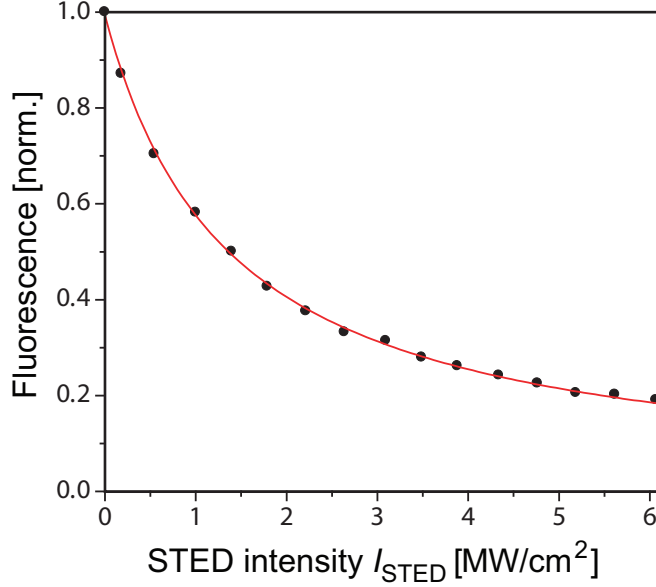
Figure 2.9: Depletion curve recorded at an excitation intensity of $I_{\text{exc}} = 85\,\text{kW/cm}^2$ and quenching wavelength 775 nm. The red curve is a fit of equation (2.9). The statistical errors are to small to be visible in the graph.

lective fluorescence inhibition. This emphasizes the degree of optical control over the fluorescence as well as its reversible nature.

The aim of the photophysical study presented in this section was to investigate the mechanism behind this fluorescence quenching.

Determination of the depletion cross section

Because in this case the fluorophores are located inside a crystal and their concentration is quite low, it would be very difficult to carry out a similar pump-probe experiment as described in section 2.2. Therefore the wavelength dependent quenching cross section was determined from depletion curves acquired from a single color center for wavelengths ranging from 745 nm up to 825 nm. Each data point of such a curve is the fluorescence signal at a certain quenching intensity corrected by the background counts, when no color center is located at the focus, normalized to the fluorescence signal, when the red beam is blocked. These values were compared to the stimulated emission cross section spectrum obtained from the NV emission spectrum using equation (2.2).

In Figure 2.9 an exemplary depletion curve is depicted. To describe such a depletion curve one has to consider the competing rates of excitation k_{exc}, fluorescence k_{fl} and stimulated emission k_{STED} to determine the time dependent occupation probability of the first excited state N_1:

$$\dot{N}_1 = k_{\text{exc}} N_0 - (k_{\text{fl}} + k_{\text{STED}})N_1, \tag{2.6}$$

with N_0 being the occupation probability of the ground state. Assuming a simple
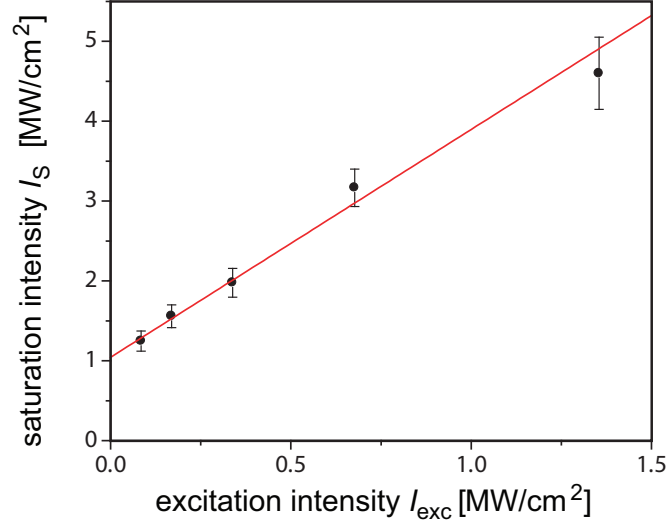
Figure 2.10: STED saturation intensity with increasing excitation intensity. The linear behavior is expected for a simple two level system under CW conditions (equation (2.10)).

two level system and a normalized overall population, the sum of the population in the ground and excited state equals unity ($N_0 + N_1 = 1$). The equilibrium is reached when $\dot{N}_1 = 0$.

Substituting,

$$0 \;=\; k_{\text{exc}}(1 - N_1) - (k_{\text{fl}} + k_{\text{STED}})N_1 \tag{2.7}$$

$$\Leftrightarrow\; N_1 \;=\; \frac{k_{\text{exc}}}{k_{\text{exc}} + k_{\text{fl}} + k_{\text{STED}}} \tag{2.8}$$

Normalizing this fluorescence signal to the fluorescence without the STED beam yields:

$$\eta = \frac{N_1}{N_1(k_{\text{STED}} = 0)} = \frac{1}{1 + \frac{k_{\text{STED}}}{k_{\text{exc}} + k_{\text{fl}}}} = \frac{1}{1 + \frac{\sigma_{\text{STED}}}{k_{\text{exc}} + k_{\text{fl}}}\Phi_{\text{STED}}} = \frac{1}{1 + \frac{I_{\text{STED}}}{I_{\text{S}}}}, \tag{2.9}$$

with the quenching cross section σ_{STED} and the photon flux density Φ_{STED} (number of photons per area and time). Half of the population is quenched at the saturation intensity

$$I_{\text{S}} = \frac{(k_{\text{exc}} + k_{\text{fl}})\,h\nu_{\text{STED}}}{\sigma_{\text{STED}}} = \frac{\sigma_{\text{exc}}\,h\nu_{\text{STED}}}{\sigma_{\text{STED}}\,h\nu_{\text{exc}}}I_{\text{exc}} + \frac{k_{\text{fl}}\,h\nu_{\text{STED}}}{\sigma_{\text{STED}}}, \tag{2.10}$$

where $h\nu_{\text{STED}}$ is the energy of a red photon and $h\nu_{\text{exc}}$ the energy of a green photon. This saturation intensity is determined by fitting expression (2.9) to the depletion curves obtained at different excitation intensities which are similar to the one presented in Figure 2.9. I_{S} depends linear on the excitation intensity as can be seen in Figure 2.10. Each data point is the mean value of three measurements.

The errors are composed of the standard deviation of the three measurements as well as 5% relative uncertainty for the power measurement and determination of the spatial peak intensity respectively. A linear fit using equation (2.10) provides the saturation intensity for vanishing excitation intensity from the y-axis intercept as well as the ratio between the excitation and quenching cross sections from the slope. The value for the excitation cross section identified from this measurement is $\sigma_{\mathrm{exc}} = (8.5 \pm 1.1) \cdot 10^{-17}\,\mathrm{cm}^2$ which agrees with the value reported in the literature [61].

This measurement can be used as calibration to recalculate the saturation intensity for vanishing excitation from the saturation intensity determined for a specific excitation intensity. For example at an intensity of $I_{\mathrm{exc}} = 85\,\mathrm{kW/cm}^2$, the correction factor is 0.85 ± 0.06.

In this manner three depletion curves for every wavelength were recorded at an excitation intensity of $I_{\mathrm{exc}} = 85\,\mathrm{kW/cm}^2$. Each curve was fitted with expression (2.9). The depletion cross sections σ_{STED} were determined from the corrected saturation intensities. In a similar way stimulated emission cross sections of single dye molecules had been determined using pulsed laser sources [62]. The results are plotted in Figure 2.11. Here again each data point is the mean value of the three measurements. The errors are composed of the standard deviation of the three measurements as well as the uncertainty of the correction factor and 5%
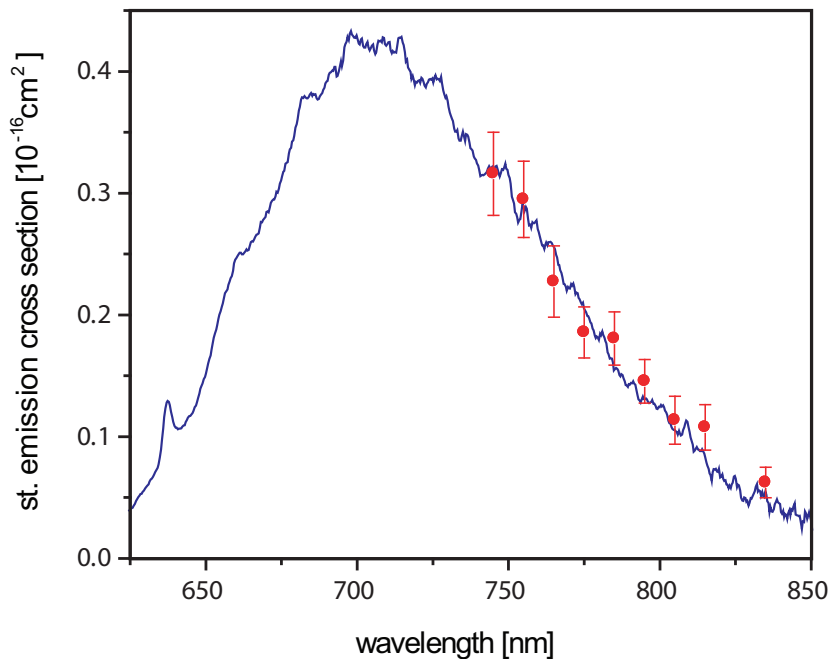

Figure 2.11: Stimulated emission cross section spectrum (blue line) and quenching cross section determined from depletion curve obtained for different wavelength (red circles). Both measurements agree well with each other and follow the same spectral dependence which proves that stimulated emission is the quenching mechanism for NV color centers.

relative uncertainty for the power measurement and determination of the spatial peak intensity respectively.

These values for the depletion cross section are compared to the stimulated emission cross section spectrum. This is determined from the emission spectrum $E(\lambda)$ of a single NV center which is normalized to its quantum yield $(Q = \int E(\lambda) \, d\lambda = 1)$ [53] using equation (2.2), with the refractive index of diamond $n = 2.417$ and the fluorescence lifetime $\tau = 11.6\,\mathrm{ns}$ of a NV center in bulk diamond. The emission spectrum of a single NV following excitation at $532\,\mathrm{nm}$ was recorded with a calibrated (both wavelength and intensity) high sensitive spectrometer (QE65000, Ocean Optics, Dunedin, Fl, USA) in confocal detection.

Both independent measurements correspond well with each other. The values as well as the spectral dependence of the quenching cross section agrees with the stimulated emission cross section determined from the emission spectrum. While this is not a direct proof for stimulated emission, from this agreement one can conclude that stimulated emission is with high probability responsible process for fluorescence inhibition of NV color centers.

This study shows that the fluorescence of NV color center can be actively and reversibly controlled by light and also that the underlying mechanism is most likely stimulated emission. If the optical transition would not be due to stimulated emission, sub-diffraction imaging would still be viable, because the NV centers show efficient fluorescence quenching. In chapter 4 this transition is utilized for STED microscopy of NV color centers demonstrating nanometric resolution using all far-field optical means.

Chapter 3

Heat as an alternative to fluorescence

As discussed in the previous chapter, a definite optical transition between two distinguishable states A and B is the essential prerequisite for far-field optical nanoscopy. Usually these states A and B are a fluorescent (bright) state and a non-fluorescent (dark) state. Thus the fluorescence signal provides the imaging contrast. Fluorescence had been used as contrast mechanism with good cause: it is a very sensitive method because it is background free. The fluorescence photons can be filtered spectrally, spatially, and temporally and therefore discriminated from almost any source of background. However, it is a requirement for the dye to show efficient fluorescence. There is a much larger group of chromophores which can be excited by light, but do not show spontaneous emission. Finding an alternative imaging contrast, which is only based on absorption rather than fluorescence would expand the concept of nanoscopy to a much larger group of markers (Fig. 3.1). In the following chapter it is investigated whether the generation of heat through absorption could also function as an imaging contrast. Thus it would extend the concept of nanoscopy to the possible use of markers with a purely absorbing state (A) and a non-absorbing state (B) like for example chromophoric compounds.
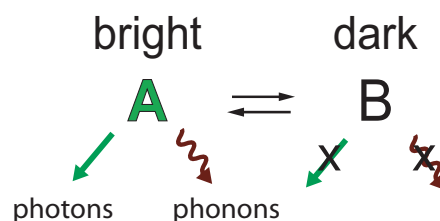

Figure 3.1: Two distinguishable states A and B as well as an optical transition between them is essential for nanoscopy. The property which makes them discernible can be spontaneous emission of photons but can also be any other optically detectable signal, for example phonons which can be measured through a rise in temperature.

Absorption had been typically measured by the change in transmission. However, the transmission change has to be quite large to be detectable because it has to exceed the laser noise of the excitation beam ($\approx$ 1-5 %). If only a very small portion of the photons get absorbed, the transmission signal appears to be constant. This is the case in microscopy where only a few chromophores (absorbers) are located in the focus. Besides reducing the number of photons in the excitation beam, absorption yields a dissipation of the absorbed energy to the surroundings of the chromophore through non-radiative decay pathways. This induced heat can be measured optically by utilizing the refractive index change due to the local rise in temperature. This can be done by exploiting the thermal lens effect [63] or an interference contrast [64]. Recently a heterodyne detection scheme has been proposed by Cognet and Lounis [65]. Light of a red-shifted probe beam is scattered from the refractive index profile which is introduced by absorption. This scattered field is detected through its beatnote with the probe field which makes it possible to detect very small temperature changes [66].

3.1   Temperature change as a contrast mechanism

Let's consider an absorbing sphere of radius R which is much smaller than the optical wavelength embedded in a homogeneous medium with thermal diffusivity $K = \kappa/c_{\text{V}}$, thermal conductivity κ and heat capacity per volume c_{V}. The equation for heat conduction in a three dimensional medium is given by [67]:

$$\frac{1}{K}\frac{\partial T(r,t)}{\partial t} = \nabla^2 T(r,t), \tag{3.1}$$

where T is the temperature at a given position $r = \sqrt{x^2 + y^2 + z^2}$ at time t and the Laplace operator $\nabla^2 = \frac{\partial^2}{\partial x^2} + \frac{\partial^2}{\partial y^2} + \frac{\partial^2}{\partial z^2}$.

This equation is solved by:

$$T(r,t) = \frac{Q}{8(\pi \kappa t)^{3/2}} \exp\left(\frac{-r^2}{4Kt}\right). \tag{3.2}$$

This is the solution of an instantaneous point source of strength $Q = E_{\text{heat}}/c_{\text{V}}$ with introduced heating energy E_{heat}.

If a constant heating power P_{heat} is applied, this expression has to be integrated from time $t = 0$ when the heating started until time t

$$\Delta T(r,t) = \frac{P_{\text{heat}}}{8(\pi \kappa)^{3/2}} \int_0^t \frac{1}{(t-t')^{3/2}} \exp\left(\frac{-r^2}{4K(t-t')}\right) \mathrm{d}t' \tag{3.3}$$

$$= \frac{P_{\text{heat}}}{4\pi \kappa r}\left(1 - \text{erf}\left(\frac{r}{\sqrt{4Kt}}\right)\right) \tag{3.4}$$

for $t \to \infty$ this expression reduces to $T(r) = \frac{P_{\text{heat}}}{4\pi\kappa r}$. Thus the temperature distribution for a constant supply of heat which spreads outwards in the infinite medium is given by $1/r$. This reflects the situation of a continuous laser beam exciting a point-like absorber like for example a chromophore.

To be able to use lock-in detection to filter out the small signal introduced by absorption, the heating beam has to be modulated. In this way a periodic varying heat source is realized. Following the same calculation as before for such a periodic point source with $P_{\text{heat}}(1+\cos(\omega t))$ and modulation frequency ω yields:

$$\Delta T(r,t) = \frac{P_{\text{heat}}}{4\pi\kappa r} \left(1 + \exp\left(-\frac{r}{r_{\text{th}}} \right) \cos\left(\omega t - \frac{r}{r_{\text{th}}} \right) \right), \qquad (3.5)$$

where $r_{\text{th}} = \sqrt{2K/\omega}$ is a characteristic length for heat diffusion.

The change in refractive index is given by $\Delta n = \frac{\partial n}{\partial T}\Delta T$. Therefore the scattered field is stronger, the larger $\frac{\partial n}{\partial T}$ of the embedding medium, the inverse of the thermal conductivity $1/\kappa$ and the absorbed heat P_{heat} are. The region of changing refractive index can be understood as a scattering object for the probe beam, whereas the modulation frequency and the thermal diffusivity K determine the sizes of this effective scattering object.

Table 3.1 lists the thermal properties of common media used in microscopy. Biological samples consist mainly of water. However, methanol offers a three times lower thermal conductivity and more than twice as large change in refractive index per degree Kelvin than water. Therefore it would be preferable to embed fixed cells in methanol. Also immersion oil has very good thermal properties which could be used for technical samples e.g. for material science.

Medium	κ [W/m K]	ρ [g/cm^2]	C_{V} [J/m^{3}K]	K [m^2/s]	dn/dT [1/K]
Water	0.6	1	$4.18{\cdot}10^6$	$1.4{\cdot}10^{-7}$	$9{\cdot}10^{-5}$
Methanol	0.21	0.79	$2.5{\cdot}10^6$	$8{\cdot}10^{-8}$	$-4{\cdot}10^{-4}$
Oil	0.1	0.92	$1.65{\cdot}10^6$	$6{\cdot}10^{-8}$	$3\text{-}4{\cdot}10^{-4}$

Table 3.1: Thermal properties of water [68, 69], methanol [70, 69] and immersion oil [71].

3.2 Experimental setup

In Figure 3.2 a schematic diagram of the experimental setup is depicted. The 532 nm light of a CW laser (Verdi, Coherent Inc., Santa Clara, CA, USA) is modulated by an acousto-optical modulator (AOM, AA.MTS.110/A3-VIS, AA Acousto Optics, France). This heating beam is combined by a dichroic mirror with a CW red probe-beam of a Ti:sapphire laser (MaiTai, Spectra Physics, Mountain View, CA, USA) or of a CW diode laser at 785 nm (Omicron, Rodgau-Dudenhofen, Germany). Both beams are collinearly directed through a 1.4 numerical aperture

oil immersion lens (Leica mircosystems, Wetzlar, Germany) and focused onto the same spot in the sample. A polarizing beam splitter (PBS) together with a quarter wave plate extracts the reflected light and the back-scattered light. In a second scheme a second objective (NA=0.95, Leica mircosystems, Wetzlar, Germany) is used to collect the transmitted beams. The reflected and transmitted probe light are filtered by bandpass filters (AHF Analysentechnik, Tübingen, Germany) and detected with a photodiode. A lock-in amplifier (Model 7265, Signal Recovery, Wokingham, UK) extracts the signal of the scattered fields at the modulation frequency. A microscopy image was obtained by scanning the sample with respect to the focal spot using a piezo stage (Nanoblock, Melles Griot, Cambridge, UK).
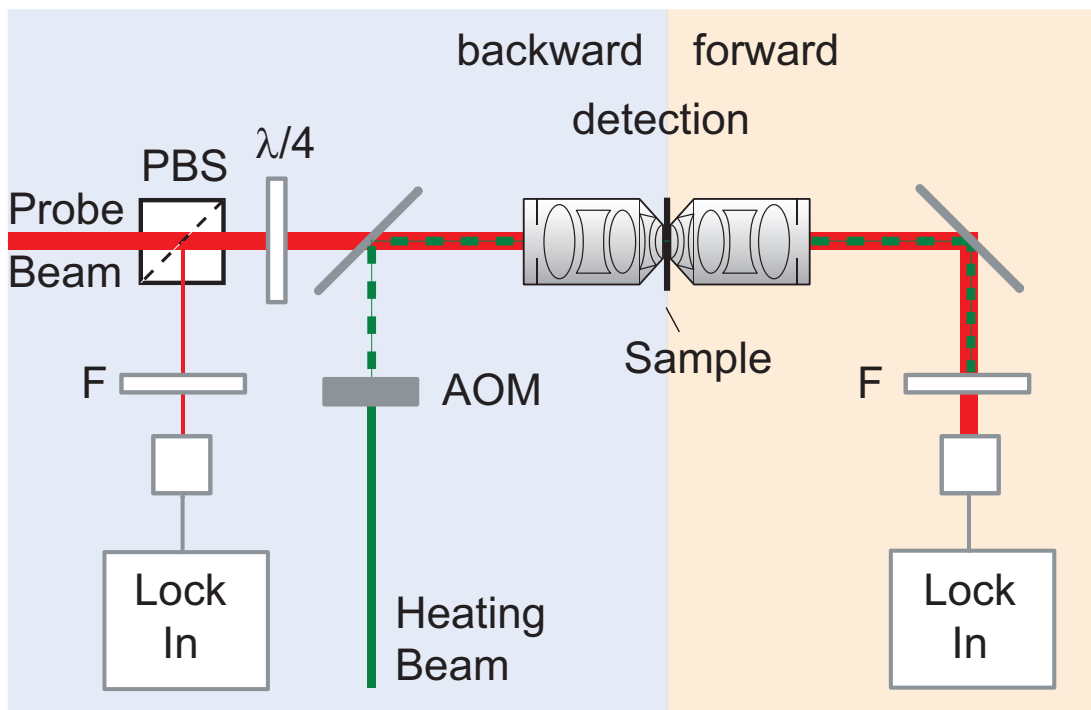

Figure 3.2: Setup for absorption imaging. A backward and a forward detection scheme were realized. F: filters, PBS: polarizing beam splitter, AOM: acousto-optic modulator.

3.3 Results

First the setup was characterized using gold nanoparticles. Next saturable absorber dyes were tested for their suitability as markers for absorption imaging. Finally the results of imaging biological cells are presented.

3.3.1 Gold particles

To test the abilities of the setup, gold nanoparticles were used. They are quite suitable because of their stability and their efficient absorption. A 2 nm gold

particle has an absorption cross section of $\sigma_{\mathrm{exc}} = 5 \cdot 10^{-15}\,\mathrm{cm}^2$ at a wavelength close to the plasma resonance [65]. This is one magnitude larger than that of a dye molecule. They also exhibit a fast electron-phonon interaction of about one picosecond. These properties make them very efficient absorbers.

To prepare the samples 2 nm gold particles (Plano GmbH, Wetzlar, Germany) were applied onto coverslips previously treated with Poly-L-lysine (0.1% (w/v) in water) and then mounted with immersion oil. An image of two gold nanoparticles is shown in Figure 3.3a. It was recorded with 10 ms integration time of the lock-in amplifier and 25 ms pixel dwell time to record the image with 15 mW green light power at 40 kHz modulation frequency and 20 mW at 745 nm of the Ti:sapphire laser. With these parameters a signal to noise ratio (SNR) of 20:1 was achieved.

The scattered signal is linearly proportional to the heating power as well as the power of the probe beam. Therefore this technique has the ability of 3D sectioning as confocal microscopy, because both light fields have to be present to generate a signal. Because scattering is a coherent process the image formation is not simply the convolution of the objects with the point spread function (PSF) as for an incoherent process like fluorescence. The amplitude as well as the relative phase between the scattered light fields at the image plane contribute to the image. However, the FWHM of a single scatterer can be approximated by the FWHM of the multiplication of the focal light distributions of the excitation and the probe beams. The measured FWHM of $\Delta r = 205\,\mathrm{nm}$ of the gold bead images in Figure 3.3 fits well the expected value of $\Delta r = 190\,\mathrm{nm}$ which results from $\Delta r_{\mathrm{exc}} = 228\,\mathrm{nm}$ and $\Delta r_{\mathrm{probe}} = 332\,\mathrm{nm}$.

To improve the sensitivity of this method, one can optimize the absorption and thermal properties of the sample or reduce the noise signal. The noise level plays a crucial role for this technique because the small signal of the scattered field is buried in the laser noise. With the lock-in detection it is possible to reduce the noise level to detect the small amount of scattered light. In terms of noise reduction it is preferable to measure at high modulation frequencies because the laser noise decreases with a higher frequency. However, for high modulation frequencies, the thermal spot is smaller as explained before, and therefore also the signal level. Thus, at a certain point, a higher frequency does not yield a higher SNR. Therefore a probe laser with good noise characteristics even for relatively low frequencies (kHz-range) is preferable.

Using the Ti:sapphire laser in pulsed mode heated up the surroundings of the gold beads so much that it produced a huge signal and destroyed the fixation of the beads. This made a controlled measurement impossible. Therefore the laser was forced to CW operation by preventing the mode locking through reflection of a small portion of the light back into the laser. This increased the noise level by an order of magnitude compared to the unperturbed pulsed mode. The laser noise in CW mode was 3-6% rms (root mean square). The use of a noise eater (LS-PRO, BEOC, Brockton, MA, USA) to reduce this intensity noise fluctuation or changing to an argon-krypton laser (Innova Sabre, Coherent Inc., Santa Clara,

CA, USA) did not significantly reduce the noise level. The low noise diode laser at 785 nm from Omicron features a laser noise of 0.1% rms. This is a factor 50 lower than that of the used Ti:sapphire laser. Employing the lock-in amplifier at 40 kHz with 5 ms integration time, yield a noise level of $3 \cdot 10^{-6}$ compared to the full signal. Thus with this technique a signal which is five orders of magnitude smaller than the full signal level of the laser beam can still be recorded with an SNR of 3:1.
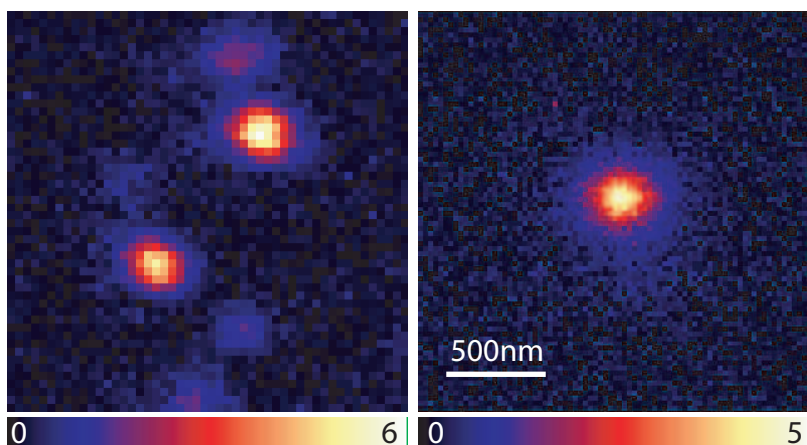

Figure 3.3: Left: Image of 2 nm gold beads using a Ti:sapphire laser as the probe beam. Right: Same measurement with a low-noise diode laser as probe beam. The SNR is the same for the two images, however for the right image almost three orders of magnitude less excitation power was used.

Another way to increase the signal is to change to the forward detection scheme. This can be understood by looking at the angle distribution of the scattered signal. For point-like scatterers – particles much smaller than the light wavelength – the amount of forward scattered light is the same as that for the backscattered light (Rayleigh scattering). That is the case for high modulation frequencies which yield a small region with increased temperature. However, for frequencies in the kHz-range the thermal spot size is comparable to the wavelength of the light. In this case the forward scattered component is dominant (Mie scattering). Therefore collecting the transmitted instead of the reflected light improves the ratio of scattered light to non-scattered light.

The image in Figure 3.3b was recorded in the forward detection scheme with 5 ms integration time of the lock-in amplifier and 25 ms pixel dwell time at $30 \, \mu W$ green light and 100 mW of the diode laser with 20 kHz modulation frequency. Note that the SNR in both images is 20:1, however the heating power for the right image is lower by 500-fold, resulting in an improvement of almost three orders of magnitude.

3.3.2 Chromophores

To convey this imaging contrast to chromophores would be the first step towards non-fluorescent nanoscopy because there are switchable variants like chromophoric compounds. As mentioned earlier, an optical transition between an absorbing and non-absorbing state is necessary for sub-diffraction imaging. However, an inert substance like gold does not show such a mechanism. For chromophoric compounds there is a probability that upon excitation a reaction takes place yielding a product with shifted absorption spectrum, for example from UV to visible. These two conformational states could serve as detectable and non-detectable states for nanoscopy.

Saturable absorber dyes

Dyes which are used as saturable absorbers in passively mode locked dye lasers are strong and stable absorbers [72, 73, 74]. Therefore they are good candidates for a first proof of principle. There are three promising dyes with an absorption spectrum around 530 nm and peak absorption cross section around $4 \cdot 10^{-16} \text{cm}^2$ in alcoholic solvents: DASBTI, HICI and DMETCI (Exciton, Dayton, Ohio, USA).

From these three dyes HICI showed the strongest absorption signal. Therefore further measurements were carried out with this dye. The thermal signal shows an exponential drop due to bleaching in an aqueous dye solution which would be preferable for biological samples (Fig. 3.4). Dissolved in methanol, HICI is more stable and the absorption signal is five times larger than in water. This data was taken with an integration time of 5 ms at $250\,\mu\text{W}$ in the green beam and 10 mW of the red beam with 40 kHz modulation frequency.

To check that the signal is induced by the heating beam, its dependence on the excitation power was measured (Fig. 3.5a). The behavior is almost linear. The slight saturation of the signal with a saturation intensity of $P = 7.5\,\text{mW}$
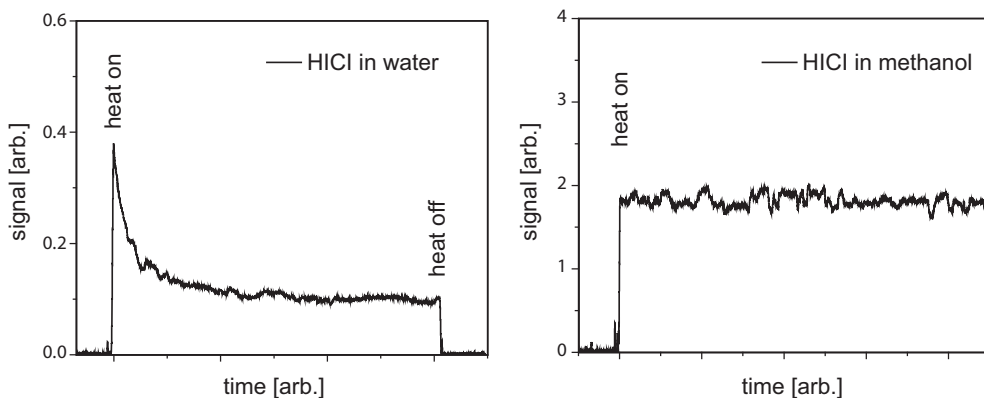

Figure 3.4: Left: Heating signal from HICI dissolved in water over time. It clearly shows bleaching. Right: Same measurement in methanol. Note that the signal is stable and five fold improved.

is probably due to excitation saturation which is reasonable for an excitation cross section of $4 \cdot 10^{-16} \text{cm}^2$ and an excited state lifetime of about $\tau = 50 \, \text{ps}$ [72]. It is also interesting to measure how the signal changes with the modulation frequency which is shown in Figure 3.5b. The laser noise spectrum has typically a 1/f behavior [75]. This would represent a line with a slope of minus one. If the signal is dropping faster than that, increasing the modulation frequency cannot improve the SNR further.
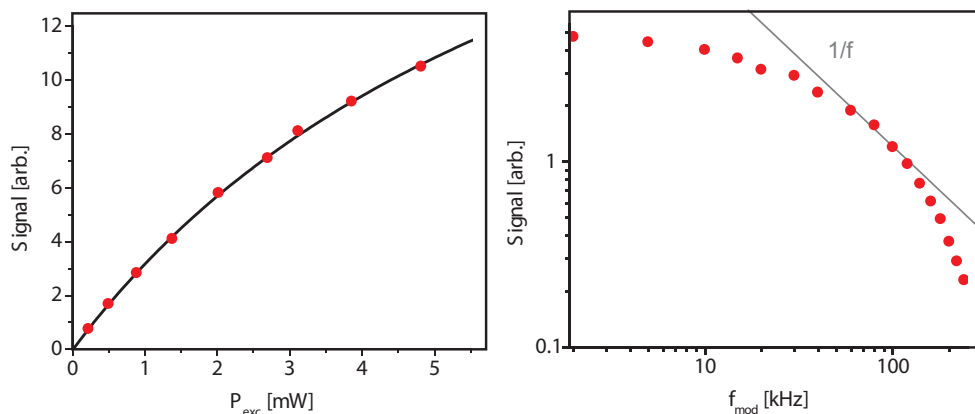

Figure 3.5: Thermal signal of HICI in methanol. Left: The dependence on the heating power is almost linear. Right: The thermal signal decreases with increasing modulation frequency because the area of elevated temperature is smaller for higher frequencies.

Chromoproteins

Another class of chromophores were studied in respect of their suitability as absorbing probes: chromoproteins. With the discovery [76] and isolation of the DNA [77] of GFP (green fluorescent protein), a whole new class of light microscopy markers was created [78]. The big advantage is that the label is synthesized endogenously by the cells. By inserting the DNA of the chromoprotein fused to the DNA sequence encoding the protein of interest, it is expressed as a fusion construct. Therefore, invasive staining techniques such as immunofluorescence can be avoided.

GFP and related derivatives show a non-changing absorption and emission spectrum. In contrast, the protein asFP595 found in the year 2000 by Lukyanov in sea anemones [79] can be switched between a fluorescent state and a non-fluorescent state by light. This protein has been successfully used in high-resolution microscopy [15]. However, there are many more suitable chromoproteins, which show only absorption. Therefore it would be desirable to find a method to visualize these dark proteins.

3.3.3   Cells

A dark non-switchable (#912, Yeast Database) and a good switchable (#508) variant of asFP595 [80] were expressed and located into the mitochondria of yeast cells (*Saccharomyces cerevisiae*) which are the "power plants" of the cell. In yeast cells they form a tube like structure with a diameter of about 200-300 nm. These cells were imaged with the absorption microscopy technique and compared to wild type yeast cells as a control. Figure 3.6 shows a bright field image of three yeast cells and two thermal images of the same cells at different z-positions. The images were taken with 5 ms integration time at 2 mW excitation light and 5 mW at 785 nm of the probe Ti:sapphire laser at 40 kHz modulation frequency. The mitochondrial network can be clearly recognized with a signal level 20-fold above the background. Also the ability of 3D-sectioning is clearly shown by the two images with 500 nm separation in the z-direction. However, the signal stemming from the cell as well as the nucleus, which can be seen in the thermal image, is only 6 or 3 fold weaker than the mitochondrial signal determining the actual background level. Similar images were obtained for all three cell lines especially also for the wild type cells which did not express the chromoproteins. This means the signal is not induced by absorption of the inserted proteins but rather from absorption of intrinsic chromophores. These results were little encouraging for specific staining with chromophoric proteins.
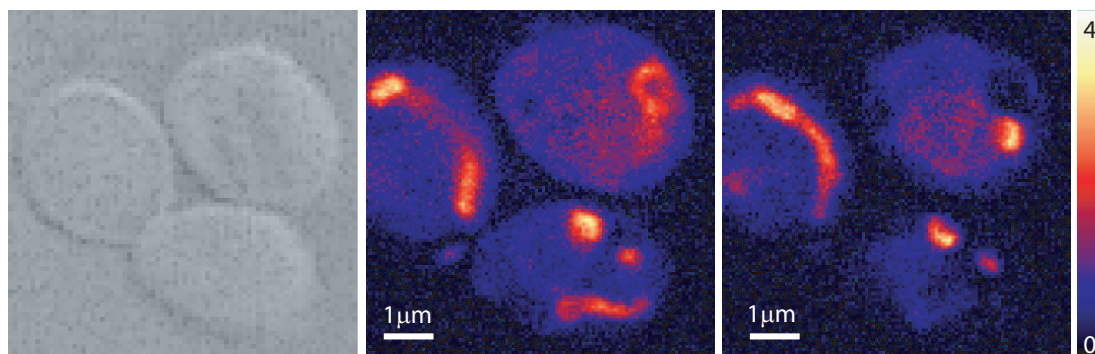

Figure 3.6: Left: Bright field image of three yeast cells. Middle and right: Absorption images of mitochondria of these cells. Both images were taken from the same cells at different z-positions.

The saturable absorber dye HICI showed promising results in solution. The next step was to bring it into biological cells and visualize the dye distribution with the thermal technique. PtK2 mammalian cells were fixed and incubated with the HICI dye solution. After several rinsing steps the sample was checked under a bright field microscope (DM 6000 B, Leica, Wezlar, Germany). The pink color of the HICI dye was clearly seen in the endoplasmic reticulum of the cell. Again the stained cells were compared to a non-treated control group. Figure 3.7 shows the thermal images of different regions of the same PtK2 cell. Again similar images were obtained for the unstained cells. The imaging contrast arises from

absorbing substances which are intrinsically incorporated in the mitochondria. Similar results were obtained by Lasne et al [81].
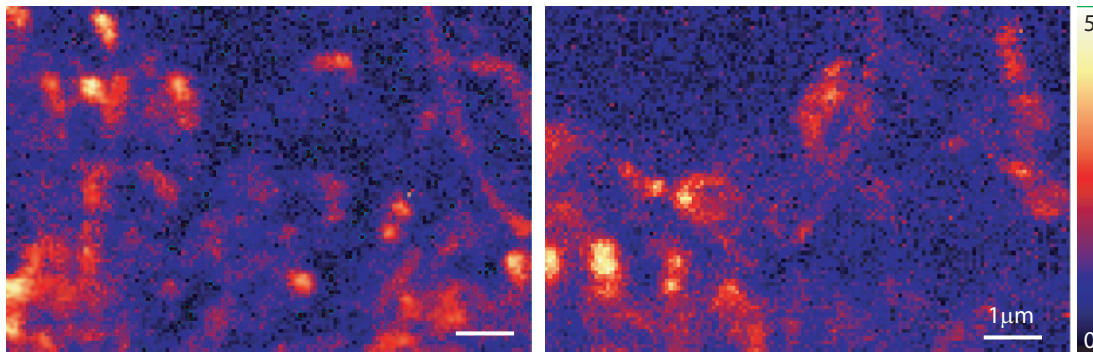

Figure 3.7: Absorption images of mitochondria in a PtK2 cell (full size 60-120 μm). The two images of different regions of the same cell were taken at different z-positions.

3.4   Discussion

A chromophore with negligible spontaneous emission has an excited state lifetime in the picosecond range due to the fast internal conversion. Therefore the excited state decays two to three orders of magnitude faster than a chromophore with efficient fluorescence and a typical lifetime of a few nanoseconds. This means that many more photons per time interval can be absorbed under saturation conditions which opens up the possibility of fast scanning. Also, bleaching mechanisms should be suppressed due to the short excited state lifetime. The probability of excited state absorption or inter system crossing into a metastable state is smaller the shorter the lifetime of the excited state gets. Therefore their photostability can be higher than for fluorescent dyes. These should be clear advantages for an imaging concept using non-fluorescent dyes.

However, the big advantage of fluorescence imaging is that it is a background free measurement. It is indeed a highly inefficient process: only a few photons are absorbed, only some of these, depending on the quantum yield, are transferred to fluorescence photons, which are then emitted isotropically into the three-dimensional space. Therefore the detection efficiency is very low. Still every single detected photon contributes directly to the signal, because unwanted signals can be blocked by spectral, spatial and/or temporal filtering. Very sensitive photon detectors such as avalanche single photon counting devices make it possible to detect even single fluorescent molecules. For these reasons it is a very sensitive technique which makes it a very successful tool.

Besides fluorescence, also scattered light can be used as an imaging contrast. Scattering by particles in the focus, for example polystyrene spheres or metal particles, is used for tracking [82]. This method is not limited by photobleaching. However, the scattered amplitude scales with R^6 because it depends on the

number of objects squared, with R being the radius of the particle. This restricts this method to relative large particles. In thermal imaging also a scattered field serves as signal, however the scatterer is optically produced by a different beam through absorption. This process varies with R^3 because it just depends linearly on the number of objects, which scales with the volume. The absorber of nanometric size is visualized by detecting a much larger "particle", the region of temperature change. By choosing the modulation frequency, it is possible to enlarge the region of increased temperature to the size of the diffraction-limited focal spot. Furthermore, the additional step of using a second beam allows the separation from background signals. In this way it is possible to detect gold particles of diameter down to 2 nm with low-cost CW laser sources and standard lock-in technique.

Using the thermal method to image biological samples shows that there is an intrinsic signal stemming from an absorbing species located in the mitochondria of the cell. Also other cell compartments produce fluctuations which increase the noise level. This reveals a significant background from endogenous absorption in cells which limits the method's specificity.

Despite these problems for biological imaging, there are more general drawbacks of the technique due to the time constants inherent to the heating process. The fast internal conversion to the ground state cannot be transfered to an increase in the imaging speed because the slowest time constant is that of heat diffusion. The time scale of this technique which utilizes refractive index change in the whole Airy disk is conceptually limited by the time it takes for the conduction of heat from the small heat source spreading out in the whole focal region. For an instantaneous point source, the temperature at a distance r from the source has its maximum at the time $t = r^2/6K$ [67]. This maximum is reached in water ($K = 1.4 \cdot 10^{-7}$ m^2/s) at a distance of $r = 100$ nm after $t \approx 12$ ns. This is the minimal timescale for the underlying process. For a non-background free detection scheme using a lock-in amplifier the measuring time is also limited by the modulation frequency and the integration time which is at current state of the art at least 100 μs.

For these reasons, contrast mechanisms other than the slow process of heat diffusion, which is also the source of troublesome background signals, should be considered. A possibility could be a method developed by W. S. Warren which measures the signal of excited state absorption of chromophores using also a lock-in amplifier to filter out the small absorption signal [83, 84]. It was shown very recently that also stimulated emission can be used to visualize dark molecules [85]. The drawback in both cases is the high intensity which is required to induce a sufficient transmission change.

Chapter 4

Nanoscopy of diamond color centers

In search of an extremum in material property, diamond is often found at the top of the list. It is the hardest known material, has the largest thermal conductivity and the widest optical band gap. Therefore diamond is not only a precious gem stone, but also very valuable to many fields in science. In this chapter it is shown that diamond is especially a very interesting material for nanoscopy. In this context, however, not the crystal properties are important. Impurities, which build fluorescent systems inside the crystal lattice, and their properties make the difference. First, the fundamentals of STED and GSD microscopy are derived. The experimental results are discussed in comparison to the theory in the subsequent sections.

4.1 Fundamentals of STED and GSD microscopy

If several objects are located in a region smaller than the diffraction limit, they cannot be separated by conventional far-field optical imaging. They would appear as one blurred spot (see Figure 4.1c). This spot is composed by the convolution of the point spread function (PSF) of the optical system with the objects' distribution.

   If the objects are distinguishable for example by color, they can be separated even at closer distances than the diffraction limit by measuring this property e.g. by using filters in case of different colors. However, up to now, no effective way has been found to sufficiently realize many distinguishable markers. In case the objects share identical properties, the only way to tell them apart is to record them sequentially in time, if they fall within one Airy disk. Therefore, as mentioned in the introduction section 1, a light-driven transition between a detectable state A and a non-detectable state B of the object is needed to make sure that during a measurement the other objects are switched off. There are two ways to detect the objects one after the other: targeted read-out where the coordinate
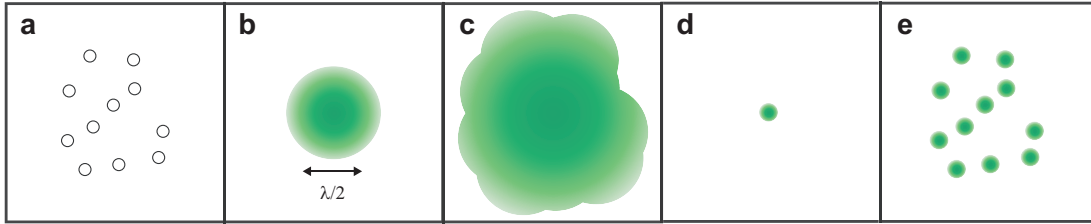
Figure 4.1: A conventional optical image (**c**) is the convolution of the distribution of objects (**a**) with the diffraction limited PSF (**b**). The objects are clearly separated (**e**) for a five time smaller PSF (**d**).

at which the fluorophore can be in state A is defined by some way or stochastic read-out where individual fluorophores are randomly switched on (transferred to A) [20]. For the targeted scanning mode, the transition between A and B has to be saturable. If the intensity of the light, which drives the transition A → B features a zero e.g. has a doughnut-shaped distribution, fluorophores located at the outer rim of this distribution are transferred to the dark state B. The saturation behavior ensures that even in the region close to zero intensity the quenching process is strong enough to confine any fluorophore to state B. This guarantees that fluorophores in state A are only located at a small spot around the minimum. Therefore the PSF is smaller than the original diffraction limited spot (Fig. 4.1d). How much smaller it is depends on the efficiency of the switching process which in turn depends on the light intensity as well as on properties of the fluorophore like the cross section of the transition or the rate of spontaneous decay to state B. Employing this concept shows that the resolution is not limited by diffraction anymore. It has become a selectable parameter of the experiment.

STED microscopy

In STED microscopy, state A is the first excited electronic state and B is the electronic ground state of a fluorophore [86]. Excitation transfers the fluorophore from B → A and leads to spontaneous emission. The de-excitation (STED) beam transfers the fluorophore back to the ground state via stimulated emission from where it cannot fluoresce anymore. Thus stimulated emission serves as the saturable optical transition (A → B) in this scheme. When the quenching rate k_{STED} is much faster than the spontaneous decay of fluorescence k_{fl}, the excited fluorophores are transferred to state B before they are able to fluoresce. Thus STED depletes the population of state A which essentially means that the fluorophores are bound to the dark state B. The depletion of A with increasing STED intensity and the resulting effective PSF is different for pulsed or continuous wave (CW) excitation and de-excitation light [87]. Therefore they are discussed separately.

Pulsed mode

In the pulsed case the excitation pulse and the depletion pulse can be separated in time. After the excitation pulse, the normalized population of the first excited state is N_1. It is assumed that the vibronic relaxation is so fast that all fluorophores in the excited state are in their lowest vibronic level by the time the STED pulse arrives. This population decreases by spontaneous decay with fluorescence lifetime τ_{fl} and the induced decay by the depletion (STED) beam with the rate k_{STED}:

$$\dot{N}_1 = -(k_{\text{fl}} + k_{\text{STED}})N_1, \qquad (4.1)$$

with $k_{\text{fl}} = 1/\tau_{\text{fl}}$.

This holds under the assumption that the STED beam does not excite the fluorophore and the vibronic relaxation to the lowest vibronic level of the ground state is fast in comparison to the STED pulse duration. If the pulse duration of the STED pulse τ is much shorter than the fluorescence lifetime, the contribution of k_{fl} to the decay of the excited state can be neglected while the STED pulse is present. Solving the differential equation (4.1) leads then to:

$$N_1(t) = N_1(0)e^{-k_{\text{STED}}t} = N_1(0)e^{-\sigma\Phi_{\text{STED}}t}, \qquad (4.2)$$

where σ is the quenching cross section and Φ_{STED} the photon flux density (number of photons per area and time).

Evaluation of expression (4.2) after time τ results in the population of N_1 which is left after the STED pulse:

$$N_1(\tau) = N_1(0)e^{-\sigma\Phi_{\text{STED}}\tau} = N_1(0)e^{-\sigma\widehat{\Phi}_{\text{STED}}}, \qquad (4.3)$$

with the photon flux density in one pulse $\widehat{\Phi}_{\text{STED}}$ (number of photons per area and pulse).

This population $N_1(\tau)$ is proportional to the detected fluorescence signal, because the excited state can only decay by spontaneous transition after the STED pulse is gone. The suppression factor η of this depletion effect is defined as the ratio of this fluorescence signal to the obtained fluorescence without the STED beam:

$$\eta = \frac{N_1(\tau)}{N_1(0)} = e^{-\sigma\widehat{\Phi}_{\text{STED}}} = e^{-\ln 2 \frac{I_{\text{STED}}}{I_{\text{S}}}}. \qquad (4.4)$$

Half of the population is quenched at the STED saturation intensity I_{S} which is a property of the fluorophore and the involved transition. This shows that the depletion behavior in the pulsed mode is an exponential decay in the simplified case.

To exploit this quenching mechanism for imaging, STED is implemented in a scanning fluorescence microscope. The excitation light is focused onto the

sample through an objective lens which also collects the fluorescence photons. The image is constructed by scanning the focus with respect to the sample or vice versa. Typically the fluorescence is focused onto a pinhole in a confocal arrangement. Note that for sub-diffraction imaging the pinhole is not essential, but is however often very useful for background reduction. The confocal PSF $h_c(r)$ is the probability $h_{exc}(r)$ to excite a fluorophore at a position r multiplied by the probability $h_{det}(r)$ to detect its fluorescence through the pinhole:

$$h_c(r) = h_{exc}(r)h_{det}(r). \tag{4.5}$$

The FWHM of the confocal PSF serves as a reference to which sub-diffraction data is compared to. To obtain an effective STED PSF, the confocal response has to be weighted with the intensity dependent suppression factor $\eta(I)$:

$$h_{eff}(r) = h_c(r)\eta(I). \tag{4.6}$$

A doughnut-shaped intensity distribution can be well approximated by a parabola at positions close to the minimum ε:

$$I_{STED}(r) \approx I_m \left[(2\beta\pi n/\lambda)^2 r^2 + \varepsilon \right], \tag{4.7}$$

with I_m being the maximal intensity at the doughnut crest, n the refractive index and λ the STED wavelength. β ($0 < \beta < 1$) depends on the semi-aperture angle α and quantifies the steepness of the minimum; for a standing wave $\beta = 1$.

The confocal PSF $h_c(r)$ has often a Gaussian profile with its FWHM being d_c. Inserting equation (4.7) into equation (4.6) leads to:

$$h_{eff}(r) = h_c(r) \exp\left(-\ln 2 \frac{I_{STED}(r)}{I_S} \right) \tag{4.8}$$

$$= \exp\left(-\frac{4\ln 2\, r^2}{d_c^2} \right) \exp\left(-\frac{4\ln 2\, I_m(\beta\pi n/\lambda)^2 r^2 + \ln 2 I_m \varepsilon}{I_S} \right) \tag{4.9}$$

$$= e^{-\ln 2\zeta\varepsilon} \exp\left(-4\ln 2 \left(d_c^{-2} + (\beta\pi n/\lambda)^2\zeta \right) r^2 \right). \tag{4.10}$$

with the saturation factor $\zeta = I_m/I_S$.

This shows that the STED PSF in the pulsed mode has again a Gaussian profile with an amplitude lowered by $e^{-\ln 2\zeta\varepsilon}$ which depends on the saturation factor and the depth of the minimum. Its FWHM, which determines the lateral resolution, is given by:

$$\boxed{\Delta r = \frac{d_c}{\sqrt{1 + d_c^2(\beta\pi n/\lambda)^2\zeta}}} \qquad \overset{\zeta \gg 1}{\Longrightarrow} \qquad \boxed{\Delta r \cong \frac{\lambda}{\beta\pi n}\sqrt{\frac{1}{\zeta}}}. \tag{4.11}$$

The resolution scales with the square root of the saturation factor. It also depends on the confocal spot size for small ζ and the steepness of the intensity profile. In the pulsed case the amplitude but not the width is affected by the depth of the minimum. Imperfections of the intensity minimum decrease the signal to noise ratio (SNR), but leave the width of the PSF unaffected. For $\zeta \to \infty$ follows $\Delta r \to 0$, signifying that in theory, the resolution is unlimited.

CW mode

In the CW mode several competing rates are present at the same time. Nevertheless, the derivation goes along the same lines as in the pulsed case. Now the excitation rate k_{exc} has to be taken into account for the time dependent population of the excited state which is then given by:

$$\dot{N}_1 = -(k_{\mathrm{fl}} + k_{\mathrm{STED}})N_1 + k_{\mathrm{exc}}\,N_0. \tag{4.12}$$

For a simple two level system and a normalized overall population, the sum of the population in the ground and excited state equals unity ($N_0 + N_1 = 1$). From the assumption that the system has reached its equilibrium follows that $\dot{N}_1 = 0$:

$$0 = -(k_{\mathrm{fl}} + k_{\mathrm{STED}})N_1 + k_{\mathrm{exc}}(1 - N_1) \tag{4.13}$$

$$\Leftrightarrow N_1 = \frac{k_{\mathrm{exc}}}{k_{\mathrm{exc}} + k_{\mathrm{fl}} + k_{\mathrm{STED}}} \tag{4.14}$$

For the suppression factor η follows:

$$\eta = \frac{N_1}{N_1(k_{\mathrm{STED}} = 0)} = \frac{1}{1 + \frac{k_{\mathrm{STED}}}{k_{\mathrm{exc}} + k_{\mathrm{fl}}}} = \frac{1}{1 + \frac{\sigma_{\mathrm{STED}}}{k_{\mathrm{exc}} + k_{\mathrm{fl}}} \Phi_{\mathrm{STED}}} = \frac{1}{1 + \frac{I_{\mathrm{STED}}}{I_{\mathrm{S}}}} \tag{4.15}$$

The depletion curve in the CW mode has a $1/(1 + \zeta)$ dependence.

To determine the STED PSF (4.6) in the CW case, the expression (4.7) for the spatial intensity distribution and the suppression factor given by equation (4.15) are inserted:

$$h_{\mathrm{eff}}(r) = h_{\mathrm{c}}(r)\frac{1}{1 + \frac{I_{\mathrm{STED}}(r)}{I_{\mathrm{S}}}} \tag{4.16}$$

$$= h_{\mathrm{c}}(r)\frac{1}{1 + \frac{I_{\mathrm{m}}[(2\beta\pi n/\lambda)^2 r^2 + \varepsilon]}{I_{\mathrm{S}}}} \tag{4.17}$$

For high saturation factors $\zeta \gg 1$, the value for the confocal PSF $h_{\mathrm{c}}(r)$ can be approximated by unity, therefore

$$h_{\mathrm{eff}}(r) \cong \frac{1}{1 + \frac{I_{\mathrm{m}}[(2\beta\pi n/\lambda)^2 r^2 + \varepsilon]}{I_{\mathrm{S}}}}. \tag{4.18}$$

For $\varepsilon \to 0$ this is a Lorentzian function.

For a non vanishing intensity in the minimum the signal amplitude drops to $h_{\mathrm{eff}}(0) = 1/(1 + \zeta\varepsilon)$. Calculating the FWHM by equalizing (4.18) with half of this amplitude results in the resolution formula:

$$\boxed{\Delta r \cong \frac{\lambda}{\beta\pi n}\sqrt{\frac{1}{\zeta} + \varepsilon}.} \tag{4.19}$$

Again the resolution scales with the square root of the saturation factor. However, the depth of the minimum ε results not only in a decrease of the signal to noise ratio, but also in a minimal value of the obtainable spot size $\Delta r_{\mathrm{min}} = \lambda(\beta\pi n)^{-1}\sqrt{\varepsilon}$.

GSD microscopy

The same principle of time sequential imaging as described at the beginning of this section holds for ground state depletion (GSD) fluorescence microscopy [14] where the fluorophore is also transferred to a dark state B by a beam featuring a central zero. In the initial proposal [14], the switching off mechanism is realized by shelving the fluorophore in the metastable dark triplet state of a dye molecule $B = T_1$ with a lifetime of micro- to milliseconds. To this end, the fluorophore is excited from the ground state S_0 to the excited state S_1 from where it is caught in T_1 via a non-radiative $S_1 \to T_1$ inter system crossing. This transition is strongly saturated. Therefore remaining ground state fluorophores are confined to the center of the minimum and can be read out by another excitation beam that is regularly focused to the doughnut center. Like in STED microscopy, scanning the co-aligned beams yields an image with improved resolution Δr.

In saturated pattern excitation (SPEM) [88] or saturated structured illumination microscopy (SSIM) [16], the ground state S_0 is also depleted by a saturated excitation, but contrary to the previous scheme, the fluorescence generated by this very same transition is recorded. Effected by an array of line-shaped intensity maxima and minima (rather than a doughnut), the saturated excitation at λ yields narrow line-shaped dark regions of dimension Δr which are steeply surrounded by a fluorescence signal giving a 'negative' imprint of the features to be imaged. In contrast to STED and GSD microscopy, the final image has to be retrieved mathematically, after turning and scanning the line-array in other directions as well. In SPEM or SSIM, it is the 'off' rather than the 'on' state that is confined to Δr in space.

Other related concepts utilize the temporal dynamics of the saturated $S_0 \to S_1$ transition [89] or extract the superresolution information from the higher harmonics generated by a temporally modulated excitation beam [90].

In any case, the essential element of all these concepts is the saturable depletion of the ground state, because the final state elicited by the excitation beam may be multiple or unknown. Moreover, once excited, the fluorophores can be raised to even higher states initiating photobleaching. In fact, photobleaching is the actual challenge of any concept relying on GSD [16, 91]. Conversely, as is shown in section 4.3, if bleaching reactions are quasi absent as in diamond color centers, GSD offers most elegant implementation of far-field optical nanoscopy.

For the implementation of GSD microscopy as realized here, the same states (ground and excited) are used as in STED microscopy. The difference is that the transition from the dark state B to the bright state A is saturated not A→B as in STED microscopy. It is a switching on mechanism rather than a switching off. Therefore the same derivation can be followed with reversed roles of the ground and the excited state.

The time dependent population of the fluorescent excited state with only an

excitation beam is given by

$$\dot{N}_1 = -k_{\mathrm{fl}} N_1 + k_{\mathrm{exc}} N_0. \tag{4.20}$$

Again, for the pulsed case, the fluorescence decay can be neglected if the pulse duration of the excitation pulse is shorter than the excited state lifetime. Following the same calculation as before with $N_0 + N_1 = 1$, the excitation saturation factor η is obtained by:

$$\eta = 1 - e^{-k_{\mathrm{exc}} t} = 1 - e^{-\sigma \widehat{\Phi}_{\mathrm{exc}}} = 1 - e^{-\ln 2\, I_{\mathrm{exc}}/I_{\mathrm{S}}}, \tag{4.21}$$

with the excitation cross section σ, the photon flux density per pulse $\widehat{\Phi}_{\mathrm{exc}}$ and the saturation intensity I_{S} at which half the population is excited. This is the inverted behavior as for STED because now the depletion of the ground state and not of the excited state is saturated.

For CW excitation equation (4.20) becomes at equilibrium condition:

$$0 \;=\; -k_{\mathrm{fl}} N_1 + k_{\mathrm{exc}}(1 - N_1) \tag{4.22}$$

$$\Leftrightarrow \; N_1 \;=\; \frac{k_{\mathrm{exc}}}{k_{\mathrm{exc}} + k_{\mathrm{fl}}} = 1 - \frac{1}{1 + \frac{k_{\mathrm{exc}}}{k_{\mathrm{fl}}}} = 1 - \frac{1}{1 + \frac{I_{\mathrm{exc}}}{I_{\mathrm{S}}}}. \tag{4.23}$$

This is also the inverted behavior as in the STED case showing the underlying principle is the same only with interchanged roles of the states.

For indirect GSD microscopy only one laser beam, the one for excitation, with a doughnut-shaped intensity distribution is needed. In this configuration all fluorophores are switched on except the ones located at the center of the beam. Thus fluorescence is recorded at every position but at $r < \Delta r$ resulting in a negative image. Instead of a signal peak at a fluorophore's position, a drop (hole) in signal is recorded. This modality differs from the original GSD method where the dye molecules are shelved in the (dark) triplet state. However, both implementations share the principle of ground state depletion to prepare the fluorophores in a definite state.
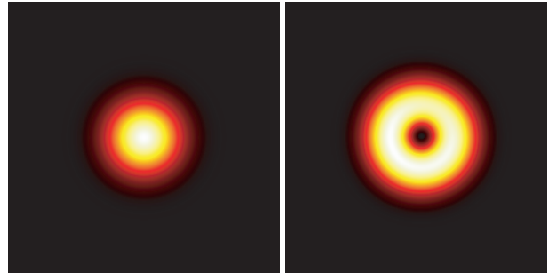

Figure 4.2: Confocal PSF of a diffraction limited Gaussian (left) and doughnut-shaped spot (right).

The effective point spread function (PSF) in this case is given by

$$h_{\text{eff}}(r, I) = h_{\text{det}}(r)\eta(I). \tag{4.24}$$

The detection PSF $h_{\text{det}}(r) \leq 1$ describes the image formation by the confocal pinhole, which is not a requirement for this technique, but is very useful, especially in this scheme, for background reduction. In the linear excitation regime the PSF mirrors the ring-shaped intensity distribution of the excitation beam (see Figure 4.2). Note that the hole of the PSF is a little smaller than the FWHM of the Gaussian spot. Therefore already smaller structures than obtained in confocal imaging can be visualized after deconvolving the negative image even under linear excitation conditions. However, this kind of recording is still within the diffraction limit. It is basically the same concept which is used in so-called structured illumination. There the excitation light is arranged in an array of lines forming an intensity pattern with maxima and minima produced by standing waves. The FWHM of those lines is about twice as small as the diffraction limit [92]. With this scheme it is therefore possible to retrieve information with twice the resolution of standard wide field imaging. However, the image has to be reconstructed mathematically from several images of this line pattern at different angles. Raster scanning the PSF of Figure 4.2b would correspond to a confocal version of "structured illumination".

For the calculation of Δr under strong saturation conditions $\zeta \gg 1$, the influence of the detection PSF in equation (4.24) can be neglected

$$h_{\text{eff}}(r, I) \cong \eta(I(r)). \tag{4.25}$$

The FWHM is determined for pulsed or CW excitation for $\zeta \gg 1$ to

$$\Delta r_{\text{pulsed}} \cong \lambda(\beta\pi n)^{-1}\sqrt{\frac{1}{\zeta}} \qquad\qquad \Delta r_{\text{CW}} \cong \lambda(\beta\pi n)^{-1}\sqrt{\frac{1}{\zeta} + \varepsilon}. \tag{4.26}$$

These are the same values as for the STED technique only that Δr is now the width of a dip and not a peak.

4.2   STED microscopy of NV centers

The concepts of nanoscopy presented in the previous section 4.1 were investigated on nitrogen vacancy (NV) defects within diamond crystals. The NV center consists of a substitutional nitrogen atom and a charged vacancy which forms a fluorescent system with six participating electrons. One can think of it like a molecule trapped inside the crystal. A detailed discussion of their properties can be found in section 2.3.2.

By imaging NV color centers in diamond, a text book like implementation of STED microscopy has been realized. The presented resolution of up to 6 nm is the highest achieved so far in far-field optical nanoscopy.
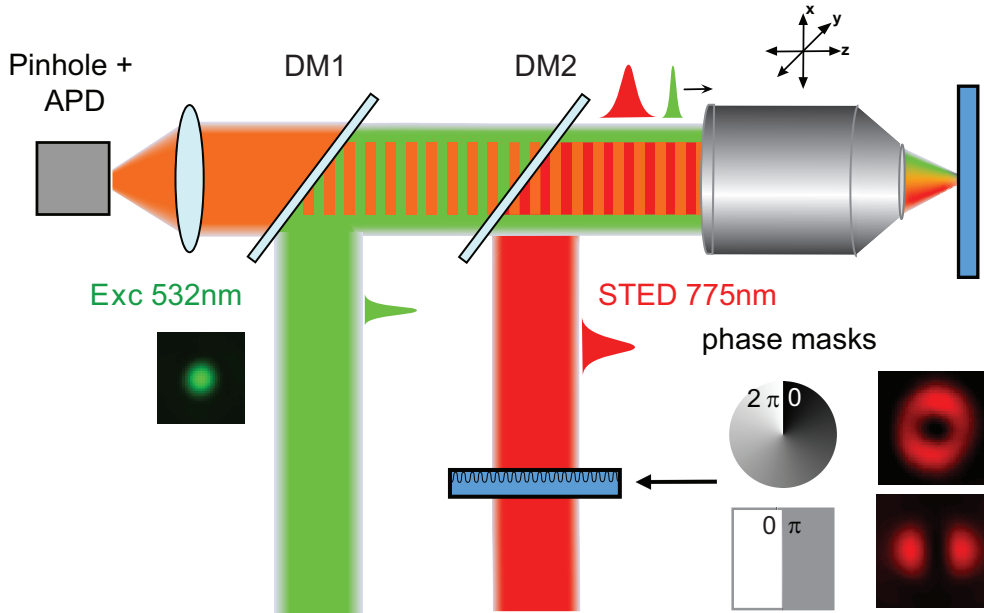
Figure 4.3: The setup is a confocal microscope with an additional red-shifted beam with a phase plate producing an intensity profile featuring a zero at the focus. A helical phase plate yields a doughnut-shaped profile for 2D-resolution enhancement and a π-step phase plate a profile with a valley along one direction for 1D-resolution enhancement (lower right). The two beams are superimposed by dichroic mirrors (DM1 and DM2).

4.2.1 Setup

A schematic sketch of the experimental setup is depicted in Figure 4.3. Excitation at 532 nm was achieved using a 60 ps pulsed laser diode (Picoquant, Berlin, Germany), which was triggered by the pulses of the STED beam provided by a laser system operating at $\lambda = 775$ nm and emitting 3.2 ns pulses at 8 MHz (IPG Photonics, Oxford, MA, USA). To achieve a temporal overlap of the two laser pulses, a fixed delay (BNC cable) and a home-built electronic delay with a variable range of 20 ns was used. The overlap was monitored by time-correlated single photon counting (Becker & Hickel, Berlin, Germany) and by measuring the fluorescence depletion efficiency directly in the diamond sample. The synchronized pulses were combined using dichroic mirrors (AHF Analysenthechnik, Tübingen, Germany) and collinearly directed through a 1.46 numerical aperture oil immersion lens (Leica mircosystems, Wetzlar, Germany) which also imaged the fluorescence onto a confocally arranged aperture of a counting avalanche photodiode (Perkin Elmer, Waltham, MA, USA). Background noise was reduced to 120 counts/s by gated detecting within a 40 ns window of the 125 ns interpulse span after the STED pulse. The two beam waist was chosen to be slightly larger than the aperture of the objective lens (5.7 mm) to realize an approximately flat intensity profile at the aperture. The cylindrical doughnut focal spot used for 2D-resolution enhancement was produced by inserting a glass waveplate (RPC

Photonics, Rochester, NY) inducing an azimuthal linear helical phase ramp from 0 to 2π radians on the initially flat wavefront of the STED beam. Radially opposing parts of the beam receive a phase shift of π radians resulting in destructive interference in the center at the focal spot. In these experiments both the excitation beam and the STED beam were circularly polarized. For one dimensional resolution enhancement, the excitation and the STED beam were linearly polarized and a phase-shift rendering the y-oriented line-shaped valley was produced by inserting a home-built achromatic phase-shifter consisting of two optical flats. The flats are tilted with respect to each other under a very small angle in the plane perpendicular to the beam direction. Therefore the optical path is slightly shorter through the more upright glass plate. The overall angle of the two glass plates with respect to the laser beam can be adjusted until the relative path difference between the two flats equals a multiple of half the wavelength. Now one half of the beam takes up a phase shift of π radians with respect to the other part resulting in destructive interference along a line through the middle of the focus. In this case, the polarization of both beams was oriented along the direction of the line-shaped valley. Scanning the sample with respect to the beams was realized by a 3D-piezo-stage (Physik Instrumente, P-733.3DD, Karlsruhe, Germany) with $0.1\,\text{nm}$ position accuracy and 0.03% linearity.

The images in Figures 4.6 and 4.7 were taken from chemical vapor deposition (CVD) grown diamond sample of type IIa with a higher density of NV centers than the crystal used for the measurements shown in Figures 4.5 and 4.9.

4.2.2   Results

The fluorescence of NV color centers can be quenched through a red-shifted beam which is applied right after the excitation. It was shown in section 2.3.2 that the underlying depletion process is stimulated emission. How effective this fluorescence inhibition can be is demonstrated in Figure 4.4 showing the fluorescence of a single center as a function of I_{STED}. The intensity values refer to spatial and temporal peak intensities assuming an aberration free focusing and rectangular laser pulses, while the transmission of the objective lens was 70% at $775\,\text{nm}$. A transmission of 95% has to be considered at the interface between the immersion oil and the diamond crystal. The time-averaged power of the excitation light was $40\,\mu\text{W}$.

A steep single exponential drop of the fluorescence with increasing I_{STED} is observed. This shows a perfect STED behavior as anticipated from expression (4.4). Extracting $I_{\text{S}} = 4.6\ \text{MW/cm}^2$ yields $\sigma = 1.2 \times 10^{-17}\,\text{cm}^2$ which agrees with the value determined from the emission spectrum in section 2.3.2. This almost rectangular curve (Fig. 4.4) shows that only for a small intensity region the NV center can be considered in the bright state ^{3}E. For higher STED intensities it is dark. In conclusion, NV centers can be effectively switched off by light as shown in figure 4.4.
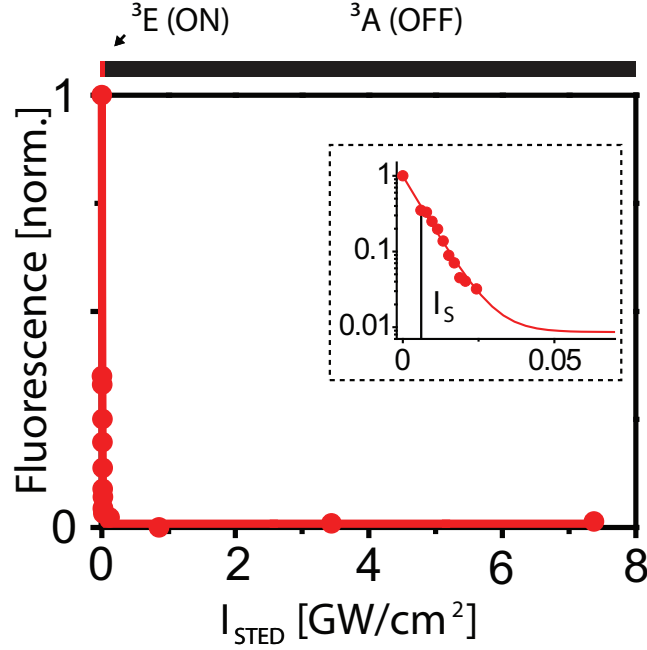
Figure 4.4: The steep fluorescence depletion curve shows the abrupt decrease of the population of ^3E with intensity. The inset shows a semi-logarithmic plot which confirms the exponential suppression of the excited state. For $I_S > 20\,\mathrm{MW/cm^2}$, the center can be considered as switched off.

For 2D imaging, the helical phase plate was inserted in the STED beam to produce a ring-shaped intensity distribution in the focus. Figure 4.5 shows a confocal image of an isolated NV center, but near its center, the STED beam is momentarily engaged. Applying $I_{\mathrm{STED}}^{\max} = 3.7\,\mathrm{GW/cm^2}$ produced a spot with a FWHM of 8 nm. In this case, the peak is also reduced by a factor of 3.5 which is due to the non-zero doughnut minimum $I_{\mathrm{STED}}^{\min}(0) = \varepsilon I_{\mathrm{STED}}^{\max}$. The amplitude of the effective STED PSF (4.10) is reduced to $\exp\left(-\ln 2\varepsilon \frac{I_{\mathrm{STED}}^{\max}}{I_S}\right)$. Clearly, such peak reductions become important at large $I_{\mathrm{STED}}^{\max}$ and therefore at high resolution. Evaluation of the measurement using Fig. 4.4 yields $\varepsilon = 7 \times 10^{-4}$. Note that the effective focal area decreases 777-fold.

High resolution & high precision

Figure 4.6 compares a confocal image with the corresponding STED image, recorded at $I_{\mathrm{STED}}^{\max} = 1.4\,\mathrm{GW/cm^2}$. While the confocal reference lacks any detail, its STED counterpart resolves each NV defect. The similar brightness and sparse occurrence in the crystal allows the conclusion that the isolated dots represent single NV defects. The images consist of 75×65 pixels, each $4\,\mathrm{nm} \times 4\,\mathrm{nm}$ in size, recorded with 5 ms dwell time. Despite the fact that each center is clearly resolved in the STED image, it is quite noisy. To reduce statistical error (the number of counts given in the color table of Fig. 4.6), the analyzed
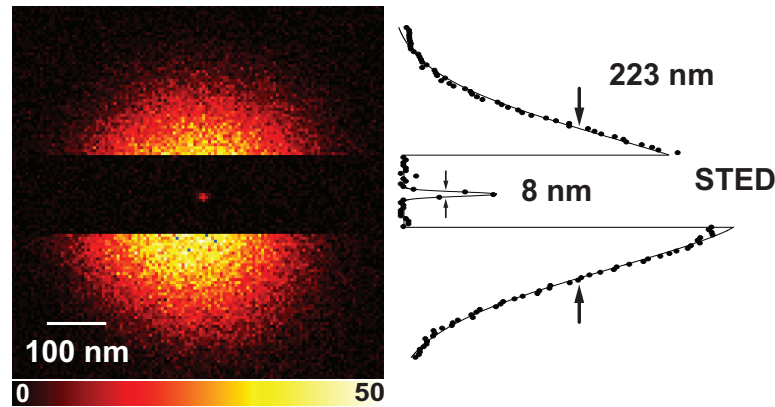
Figure 4.5: Applying $I_{\mathrm{max}} = 3.5\,\mathrm{GW/cm^2}$ shrinks a confocal spot of $223\,\mathrm{nm}$ diameter (FWHM) down to $8\,\mathrm{nm}$.

STED image of Figure 4.7a is comprised of the sum of 97 consecutively recorded STED images with the parameters stated above. Alignment of the recording was ensured by introducing subpixel translational shifts which maximize the spatial correlation between the images [93]. This exclusively corrects translational drift between consecutive images. The central positions of the defects in the registered images are stochastically distributed with a variance close to the expected localization accuracy, supporting the notion that no further substantial corrections are required in this case. The centroids were determined by Gaussian fits. A representative of such a fit is depicted in Figure 4.8. Representing the effective PSF, the images of individual centers reveal $\Delta x = 18.3\,\mathrm{nm}$ and $\Delta y = 16.0\,\mathrm{nm}$ as the resolution under the conditions employed. Note that the resolution gain
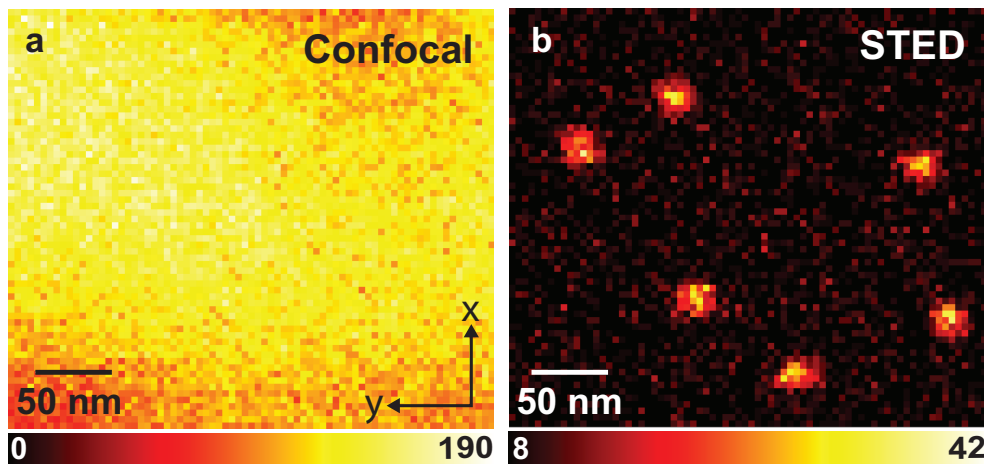

Figure 4.6: While the confocal image is entirely blurred, the STED image from the very same region contains resolved NV centers.
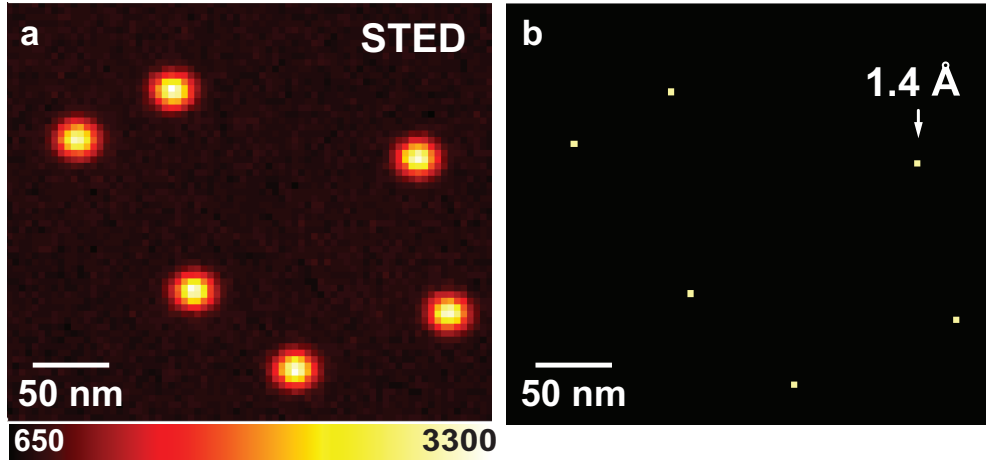
Figure 4.7: To reduce statistical error, the displayed and analyzed STED image (a) is comprised of the sum of 97 consecutively recorded STED images. The similar brightness and sparse occurrence in the crystal allows us to conclude that the isolated dots represent single NV defects. (b) The collected statistics of image (a) results in a position precision of 1.4 Å.

derives just from the optical preparation of the states ^{3}E and ^{3}A.

The STED recording inherently resolves individual NV centers because they are all further apart from each other than Δx or Δy. When scanned over the sample together with the excitation beam, the doughnut-shaped STED beam allows only a single NV center to fall within the doughnut minimum; all others are switched off. Thus STED resolves the NV centers individually and hence they are sequentially registered in time.

Once all the centers are resolved, increasing the resolution further is no longer required, when one is interested in the exact position of each center in the crystal lattice. Their position can be calculated from the centroid of their sub-diffraction-sized spot [94]. The precision of this calculation depends on the effective PSF,
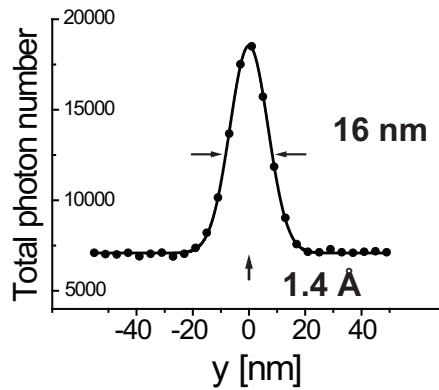

Figure 4.8: Y-profile of the effective STED-PSF in Figure 4.7a exhibits a FWHM of $y = 16.1$ nm. The coordinate of each center can be calculated with 0.14 nm precision.

on the number of collected photons, and on the background [95, 96]. A spatially homogeneous background of 1.6 counts/ms was measured throughout the imaged region, as indicated in the images. Under these conditions and the assumption that scanning errors are negligible, the xy-coordinates of each center can be determined with a precision better than 2 Ångström. This is three orders of magnitude below the diffraction limit (Fig. 4.7b). The information provided in Figure 4.7b should be compared with that contained in the confocal recording (Fig. 4.6a) which fails to render any information about the number and location of the color centers. The distance between the centers in the upper left corner projected in the xy-plane is 67.9 ± 0.1 nm. This distance would correspond to 194 lattice constants (0.35 nm) and the precision is about half a lattice constant. By extending STED into the third dimension, one can also incorporate depth information. Thus, provided that care is exerted to avoid scanning distortions and drift, STED microscopy is able to map NV centers with nanometric resolution and subnanometer precision.

No bleaching

It had been shown that NV centers are very photostable under moderate excitation power [47]. The measurement depicted in Fig. 4.9 shows that this outstanding photostability is maintained under the intense STED beams, as evidenced in consecutive STED recordings. The total fluorescence signal in each frame (Fig. 4.10) shows virtually no change in brightness and in resolution (here < 25 nm). The recording time for all images was the same causing the STED images to be darker due to a $\approx$ 100-fold reduction in focal area. From this it follows that the peak brightness of single centers is virtually equal in the STED and confocal recordings. This means the minimum intensity is less than 1% of the peak intensity. Figure 4.9 shows also the absence of blinking, which is a
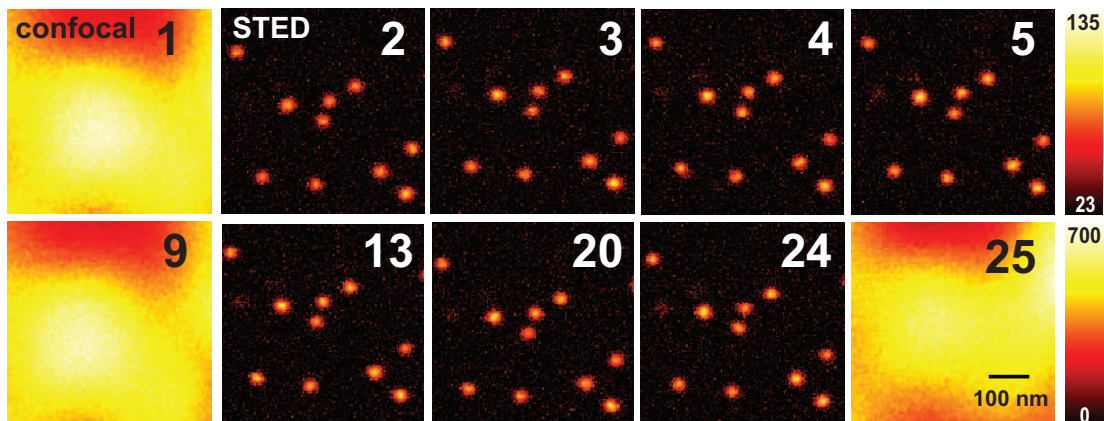

Figure 4.9: Consecutive confocal and STED recordings (as indicated) of the same crystal region showing virtually no change in brightness and in resolution (here < 25 nm). The color map in the upper panel refers to the STED images the one in the lower panel to the confocal images.
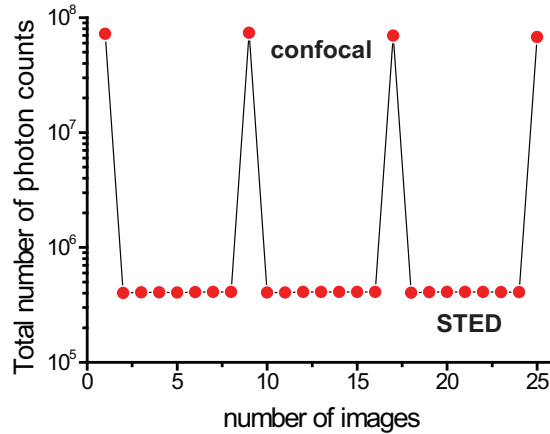
Figure 4.10: Total fluorescence signal in each image frame of Figure 4.9.

big challenge when imaging with quantum dot labels. While demonstrating optical nanoscopy without photobleaching, Fig. 4.9 highlights that with diamond nanoparticles as markers [51, 52], STED could afford (biological) fluorescence nanoscopy with countless recordings.

Maximizing the resolution

Recording images akin to those in Figs. 4.7 and 4.9 is impractical with near-field optics, because being located $> 3 \, \mu$m beneath the surface of the crystal, the color centers cannot be accessed by a tip. Besides being noninvasive and able to access the interior of the crystal, when compared to near-field optics which was applied to the imaging of NV center in powder diamond crystals [97], STED microscopy is easier to put into practice, control and operate, and provides substantially higher resolution. Likewise, alternate nanoscopy strategies that sparsely switch individual emitters (from a dark state to a state emitting a bunch of photons allowing their localization [98, 17, 18, 19]) are hard if not impossible to implement with NV color centers. This is because at room temperature, blinking or metastable switching between a bright and a dark state is nearly absent. Hence, NV centers are ideal probes for STED and STED microscopy is ideal for their imaging. This supposition is likely to apply to many other color centers in crystals.

Employing the phase mask for 1D resolution enhancement results in a focal STED beam spot with a y-oriented central zero-line with steep peaks $I_{\text{STED}}^{\text{max}}$ along the x-axis. Increasing $I_{\text{STED}}^{\text{max}}$ to $8.6 \, \text{GW/cm}^2$ squeezes the FWHM of the PSF from $\Delta r = 223 \, \text{nm}$ down to $6 \, \text{nm}$ (Figure 4.11a). The increase in resolution follows the anticipated inverse square-root law (4.11). An effective PSF of a single NV center is shown in Figure 4.11b. The line profile is representative of eight consecutive x-scans over the same NV defect. The Gaussian fit perfectly matches the data as expected from the expression for the effective STED PSF (4.10). The eight fits revealed an average measured FWHM of the scans of $5.8 \, \text{nm}$ with a standard
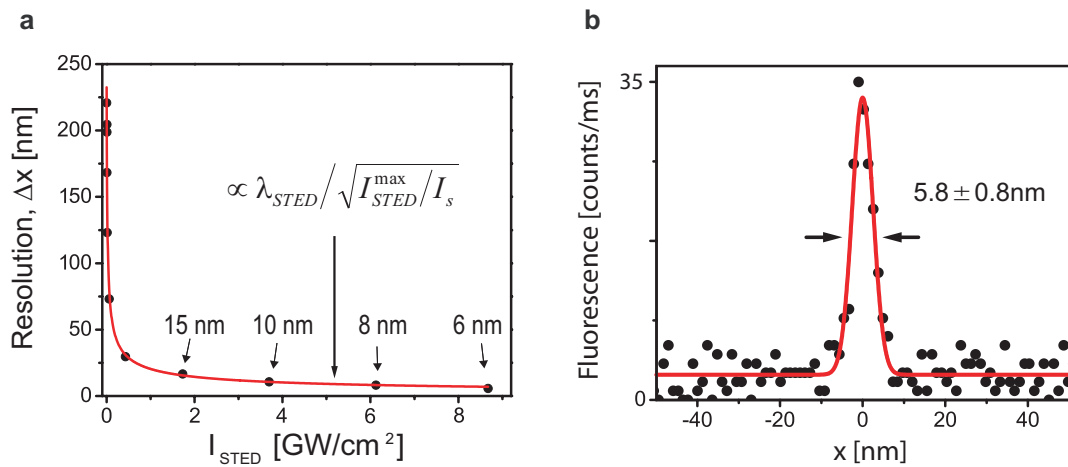
Figure 4.11: (a) The measured decrease of the lateral FWHM Δr from 223 nm down to 6 nm scales inversely with the square-root of the intensity of the STED beam (red-line). Note that all data were taken from the very same single NV defect. (b) Line profile of the effective PSF along the x-axis, demonstrating all-physics-based far-field optical resolving power of 5.8 ± 0.8 nm.

deviation of 0.8 nm. This value is 133-fold below the wavelength of the laser beam and represents a new regime of obtainable all-physics-based resolution using conventional optics.

This data shows that this experiment is a perfect implementation of STED matching well the theory. The presented single digit resolution is the highest achieved so far in far-field light microscopy.

Fluorescent nano-diamond crystals

STED microscopy of NV centers may not only be an important tool for studies on solids, but may also contribute to biological imaging. There is an ongoing interest of using diamond nanocrystals of sizes down to several nanometers as fluorescent
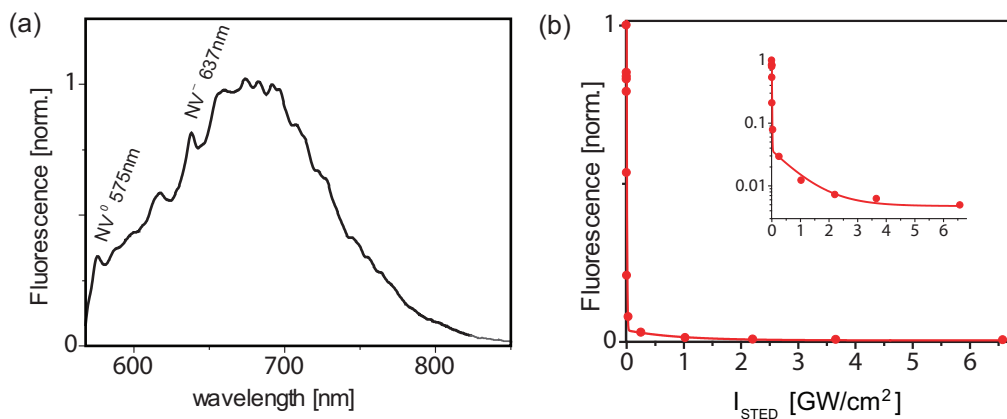

Figure 4.12: Spectrum (a) and depletion curve (b) of diamond nanocrystals.

marker for biolabeling [51, 52]. Different production procedures [99, 100] as well as surface treatments [101, 102] to attach a linker to the nanoparticle are examined. Despite the achievements made so far, obstacles like aggregation or heterogeneity in luminescence properties still have to be overcome.

In Figure 4.12a, the fluorescence spectrum of a 35 nm sized nanocrystal is shown. From the zero phonon lines (ZPL) at $\lambda = 575$ nm and $\lambda = 637$ nm can be infered that it contains NV^0 as well as NV^-. The fluorescence lifetime has multiple components and varies from nanoparticle to nanoparticle. This might be due to energy transfer processes of centers in close proximity. The depletion curve for some of the nanocrystals is not a single exponential function. It contains a very steep component resulting in a saturation intensity of 4.4 MW/cm^2 which fits well with the one for bulk diamond centers. However, 5% of the fluorescence is only quenched at an intensity 100 times higher than that (Fig. 4.12b).

In the STED image the nanocrystals are clearly separated with a resolution down to $\Delta r \approx 16$ nm, while it is impossible to draw any conclusion from the confocal image (Fig. 4.13). The 35 nm-sized nanoparticles were applied onto coverslips previously treated with Poly-L-lysine (0.1% (w/v) in water) and mounted with de-ionised water. The heterogeneity in brightness of the nanocrystals is due to the different number of NV color centers inside the particles. Some particles in the image have a halo around them of the size of the confocal PSF. This is due to the double exponential decay of fluorescence (Fig. 4.12b). Despite the inhomogeneity in photophysical properties, nanocrystals show comparable performance in resolution and photostability as the bulk diamond samples.
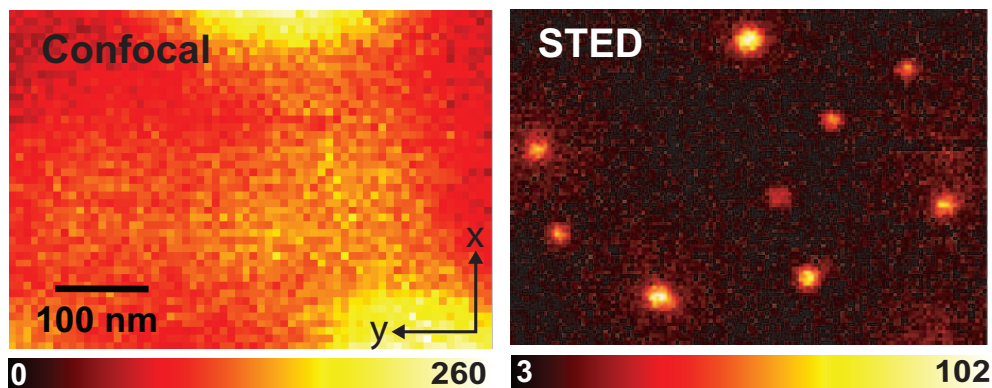

Figure 4.13: Confocal and STED image of 35 nm fluorescent nanocrystals incorporating different number of NV center.

4.3   GSD microscopy of NV centers

In STED microscopy the red-shifted beam ensures that all fluorophores are virtually all the time in the ground state except those right at the center of the doughnut. This situation is inverted in GSD microscopy: no fluorophore is in the ground state except those close to the minimum. To this end, the NV centers are driven into excitation saturation. For fluorescent dyes this would result in extensive photobleaching from which other implementations of GSD are suffering [16, 91]. Because of their enormous photostability, NV centers seem to be a perfect candidate for GSD microscopy.

In this section two schemes are presented: indirect and direct GSD. For indirect GSD the absence of fluorescence at the doughnut minimum gives the imaging contrast resulting in a negative image. In direct GSD a positive image is obtained by interrogating the population of the ground state by a second excitation beam.

4.3.1   Indirect GSD

The advantage of the indirect GSD scheme is that the experimental effort is minimal. Only one laser beam is required. It controls the population of the ground state and also drives the fluorescence transition. The disadvantage is that the recorded image is a negative one. A spatially confined drop in signal represents an object. To regain the actual distribution of fluorophores, the negative image has to be deconvoluted with the effective PSF under the same conditions.
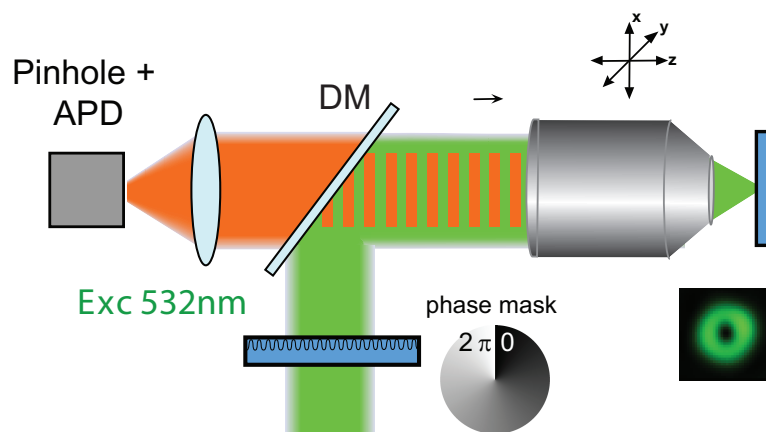

Figure 4.14: Confocal microscope with red detection and green (532 nm) excitation path merged by a dichroic mirror (DM). A helical phase ramp converts the focal Airy disk of the excitation beam into a doughnut (lower small panel). Images are obtained by scanning the sample with respect to the beams.

Setup

The setup is a confocal microscope featuring an oil immersion lens with a semi-aperture angle of $\alpha = 75°$ (1.46 NA, Leica Microsystems, Wetzlar, Germany), focusing a $\lambda = 532\,\mathrm{nm}$ CW laser beam (Verdi, Coherent Inc., Santa Clara, CA, USA) into a type IIa diamond grown by chemical vapor deposition. The fluorescence was collected by the same lens and detected after passing a dichroic filter and a confocal pinhole of 0.3 Airy disks of the emitted light which was chosen to optimize the contrast. The diamond was mounted on a 3D-piezo scanning stage (Physik Instrumente, P-733.3DD, Karlsruhe, Germany) with a position accuracy of 0.1 nm and a linearity of 0.03%.

For such high intensities of green light which are used for this experiment, the amount of autofluorescence stemming from the immersion medium is enormous despite confocal rejection. Even the so called "fluorescence free" variants showed no substantial improvement. Using 2,2'-thiodiethanol (TDE) [103] as immersion medium minimized the background to a reasonable count rate. Therefore, the immersion oil was replaced by TDE with a 2% water fraction to match the refractive index of glass ($n = 1.51$) to avoid abberations.

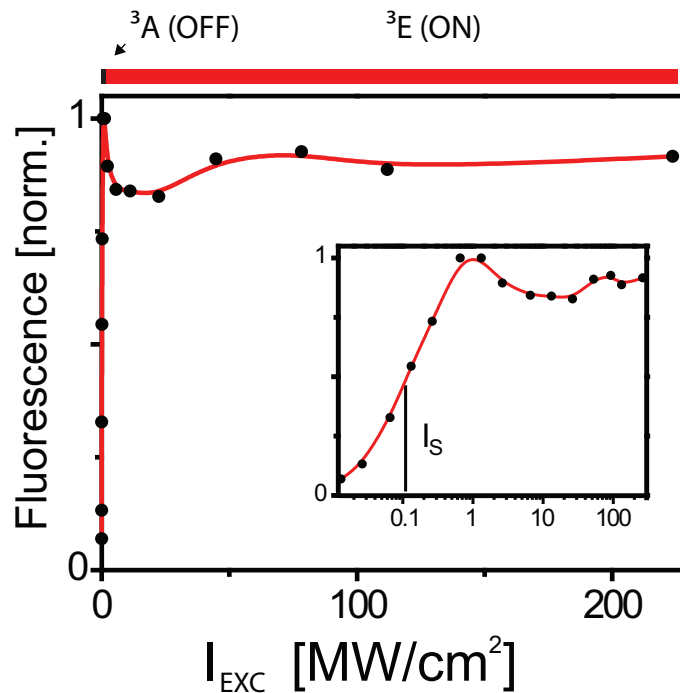Figure 4.15: The fluorescence signal shows a strong saturation behavior with increasing light intensity. This demonstrates the depopulation of the ground state resulting in an almost digital switching behavior between an On- and an Off-state. The inset depicts a semi-logarithmic plot with the saturation intensity I_S which is defined at half of the maximum signal. The solid line connects the data points to guide the eye.

An optical On-switch

Fig. 4.15 shows the normalized fluorescence $\eta(I)$ of the same NV center for $0 < I < 224\,\text{MW/cm}^2$. As a result, $\eta(I)$ exhibits a steep onset and a plateau due to the depletion of state ^{3}A. $\eta(I) = 0.5$ is obtained for $I_\text{S} = 110\,\text{kW/cm}^2$. For intensities smaller than three time I_S, $\eta(I)$ equals $1/(1 + I/I_\text{S})$ as expected from expression (4.23). For $I > 1000\,I_\text{S}$ the NV centers spend only $< 0.1\%$ of their time in the ground state, yet they are photostable. The plateau of $\eta(I)$ is slightly modulated due to intensity dependent rates to one or more dark states [57], but the decisive factor is that the centers can be effectively switched on by light. Hence, applying an $I(r)$ with a local zero, such as a doughnut or a standing
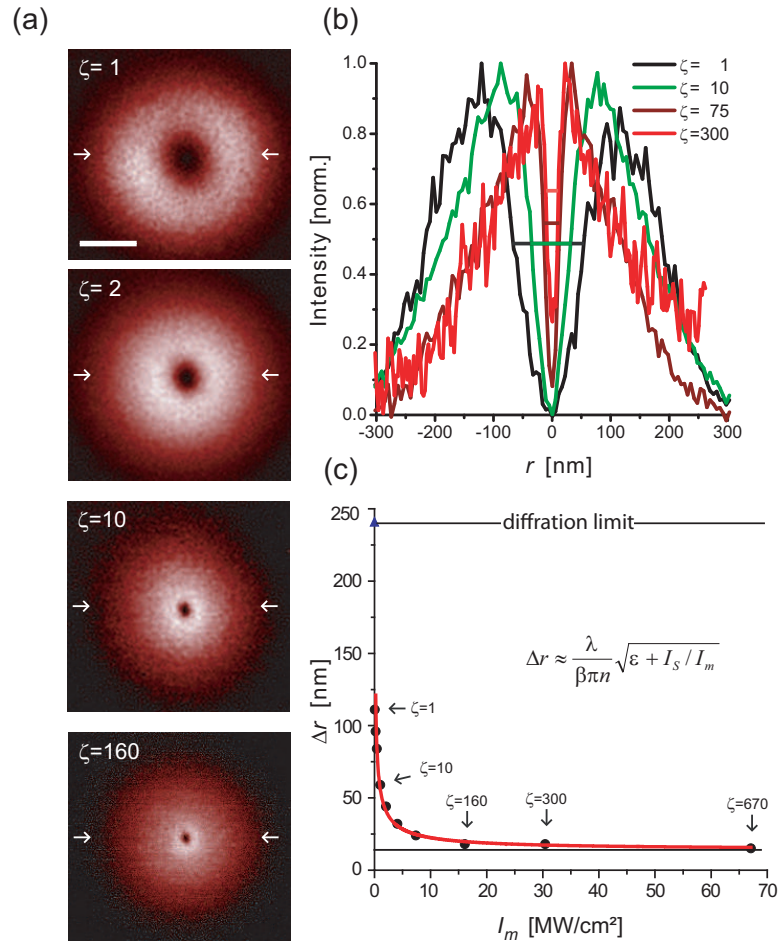
Figure 4.16: Effective point-spread-function (PSF) of the 'negative' GSD modality probed by single color centers. a) Increasing the saturation factor $I_\text{m}/I_\text{S} = \zeta$ renders PSFs with decreasing dark central area Δr; b) normalized line profiles through the PSFs; c) Δr scales inversely with the square-root of the excitation intensity c). In continuous wave GSD microscopy, the minimum depth $\varepsilon = 0.004$ obtained in an experiment limits the resolution to $15\,\text{nm} \approx \lambda/35$. Scale bar in a) is $150\,\text{nm}$.

Figure 4.17: Inverse GSD nanoscopy of densely packed color centers in diamond. a) Raw 'negative' fluorescence image recorded at $I_\mathrm{m}/I_\mathrm{S} = 160$, exhibiting the center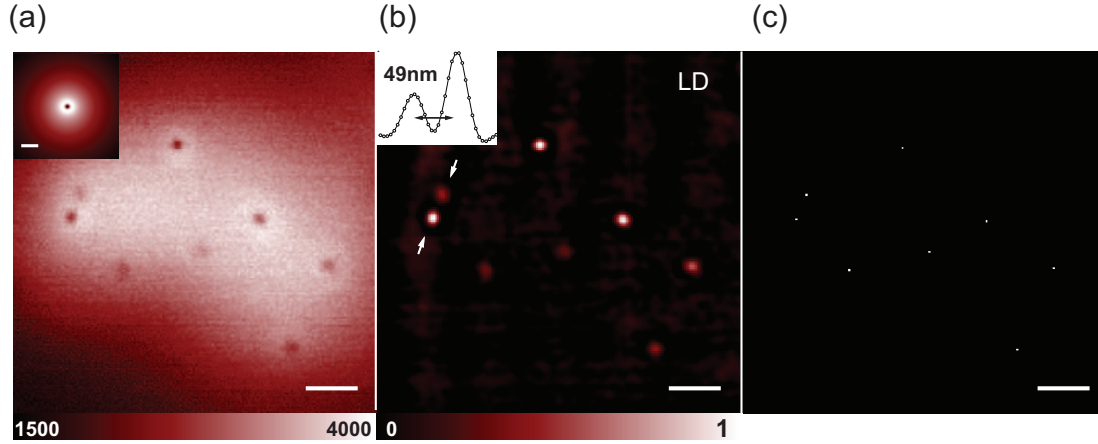s as intensity dips. The FWHM of an isolated dip reveals a focal plane resolution of $\Delta r = 14\,\mathrm{nm}$. Linear deconvolution with the calculated PSF (inset) renders a positive image (b). Although the information is contained in (a), correct mapping of the position and brightness of the centers requires the deconvolution. Given that (b) represents individual centers, calculation of their centroid refines their coordinate to $\approx 1\,\mathrm{nm}$ precision. Scale bar is $150\,\mathrm{nm}$.

wave, provides a steep gradient between the off- and on-states in space.

To test the validity of equation (4.26), the images shown in Figure 4.16 of single NV centers were recorded, i.e. the effective PSF $h_\mathrm{eff}(r, I_\mathrm{m})$ as a function of the saturation factor $I_\mathrm{m}/I_\mathrm{S} = \zeta$. The extent Δr of the central region in which the NV centers remain in the ground state scales down with increasing $I_\mathrm{m}/I_\mathrm{S}$. The determination of the doughnut minimum from the profiles for $I_\mathrm{m}/I_\mathrm{S} = 160$, 300, and 670 yield $\varepsilon = 0.004$. Measuring the fluorescence of a single defect excited with an intensity in the linear regime inside the crystal ($n = 2.42$) gave $\beta = 0.35$ for the doughnut minimum. Fitting the measured Δr with equation (4.16) exhibits excellent agreement between the equation and the experiment. The narrowest PSF features $\Delta r = 15\,\mathrm{nm} \approx \lambda/35$.

Next densely packed NV centers located ≈ 5 microns below the crystal surface were imaged using $I_\mathrm{m}/I_\mathrm{S} = 160$ (Fig. 4.17a). As anticipated, the defects are witnessed as nanosized dark spots in an extended bright area. Mandatory deconvolution with $h_\mathrm{eff}(r, I_\mathrm{m})$ renders the actual image (Fig. 4.17b). Given that all imaged centers are discerned and that the recording is not compromised by scanning distortions, the coordinates of each center can be refined by computing the centroid of each spot [94, 95, 104], here to a precision of $\approx 1\,\mathrm{nm}$.

Pulsed versus CW

In section 4.1 it has been shown that in case of a pulsed excitation beam the resolution is not directly limited by the quality of the zero. Also an exponen-
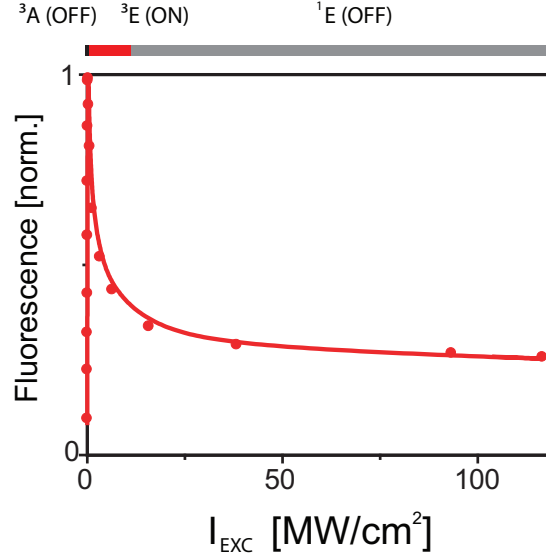
Figure 4.18: For pulsed excitation, the fluorescence signal shows also a strong saturation behavior with increasing light intensity. However, for high excitation intensities, the fluorescence signal decreases until it levels out at about 30% of the maximum value. The solid line connects the data points to guide the eye.

tial function has a steeper slope than $1/(1 + x)$. For these reasons one would expect even better results for a pulsed excitation mode. To explore this in the experiment, the CW laser was replaced by a pulsed 532 nm laser source with a pulse duration of 150 ps and 20 MHz repetition rate. The normalized fluorescence signal of a single defect with increasing excitation power is depicted in Figure 4.18. The intensity values are time averaged and spatial peak values. Half of the maximum signal is reached for $I_S = 38\,\text{kW/cm}^2$. This is in good agreement with the value determined in the CW case considering the conversion factor of the temporal pulse spacing $\tau = 50\,\text{ns}$ divided by the fluorescence lifetime $\tau_{fl} = 11.6\,\text{ns}$. The steep rise at low intensities corresponds to a single exponential function, as expected from expression (4.21). However, for high intensities, the fluorescence signal drops to only 30% of its maximal value. This is due to intensity dependent crossing rates to one or more darks states. This effect is more pronounced for the pulsed laser than for the CW source where the reduction was $\approx 10\%$ (Fig. 4.15).

This behavior is very favorable for negative imaging, because it realizes a small fluorescence signal at the outer part of the doughnut. The detected number of photons is reduced and thus also the noise level which is the bottle neck of negative imaging. The resolution however is determined only by the steep onset. Figure 4.19 shows the fluorescence signal of a doughnut-shaped excitation spot with different intensities. The dip shrinks down with increasing intensity and also the size of the bright ring decreases. In this way the patterns are self-similar meaning that the shape nearly stays the same; only the scale is changing.

The FWHM scales inversely with the square-root of the intensity I_m (Fig.
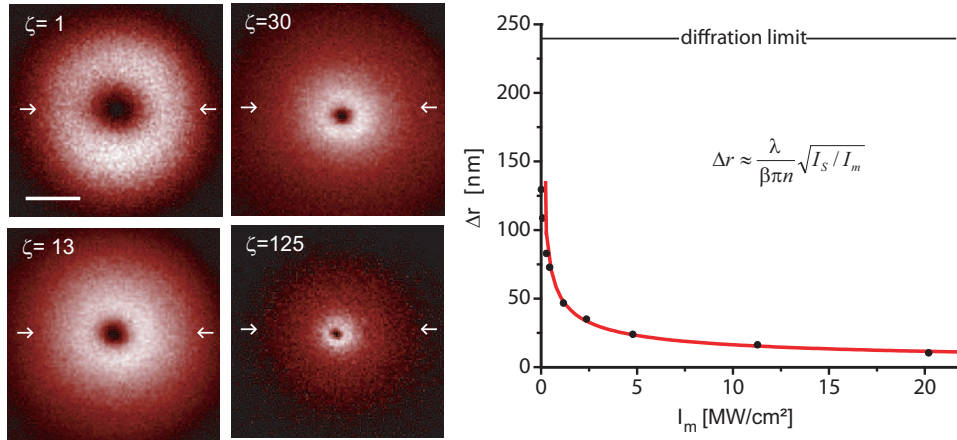
Figure 4.19: Effective point-spread-function (PSF) of pulsed excitation. Left: Increasing the saturation factor $I_{\mathrm{m}}/I_{\mathrm{S}} = \zeta$ renders PSFs with decreasing dark central area Δr. Right: Δr scales inversely with the square-root of the excitation intensity approaching 10 nm in this experiment. Scale bar is 150 nm.

4.19) down to a resolution of $\Delta r = 10$ nm. Fitting equation (4.26) with $\beta = 0.38$ and $I_{\mathrm{S}} = 31\,\mathrm{kW/cm}^2$ to the measured Δr validated again the increase in resolution in proportion to $\sqrt{I_{\mathrm{m}}/I_{\mathrm{S}}}$. The discrepancy in the saturation intensities can be explained by a misalignment of the beam with respect to the NV center or aberrations of the excitation focus.

Figure 4.20 shows three images of the same region inside the crystal at different excitation intensities. The resolving power clearly increases with higher intensity. In the second and third image bright rings around the holes are visible stemming from the drop in the saturation curve for high intensities. The resolution of about 17 nm is of the same order as in the CW case. The reason that the image quality is not improved is due to drift problems which are apparent in Figure 4.20. The fluctuations, which are more severe for higher intensities, limit the performance.
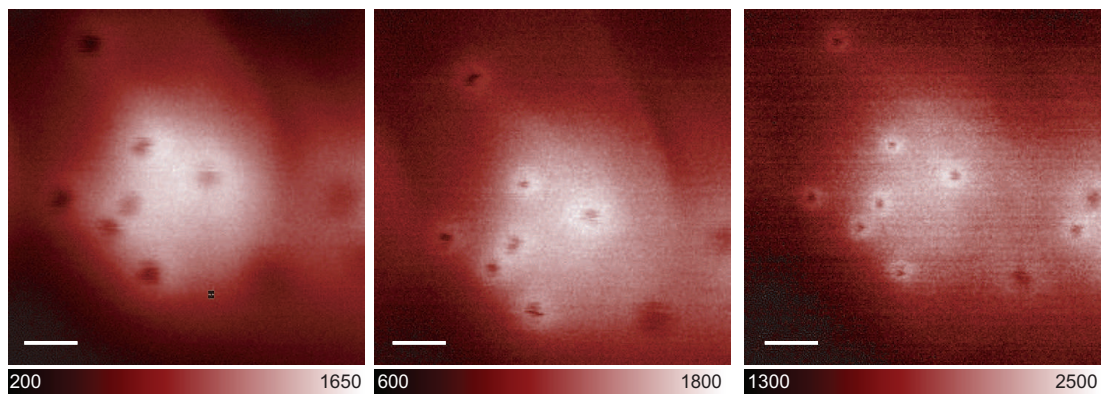

Figure 4.20: Negative images recorded at different intensities $2.4\,\mathrm{MW/cm}^2$, $7.2\,\mathrm{MW/cm}^2$, $14.4\,\mathrm{MW/cm}^2$ of the pulsed excitation beam. Scale bar is 150 nm.

This could be due to the higher peak intensities in the pulsed case.

Even though the advantages of the pulsed mode are not realized in the experiment due to other factors (such as drift), a saturation behavior as it is shown here is very interesting. If one finds a configuration such that the fluorescence signal vanishes for high intensities, that would be the perfect configuration for negative imaging. This would suppress the fluorescence signal everywhere except at a small region around the center yielding a much better signal to noise ratio.

4.3.2   Direct GSD

The second GSD version renders the image directly. To this end, a second excitation beam is employed to probe the fluorophore that, being located at the doughnut minimum, have remained in the ground state. By filtering out the fluorescence of these color centers from the full signal a positive image is produced and a mathematical reconstruction becomes unnecessary.

Setup

A regularly focused second excitation beam is added to the setup of indirect GSD, which is described in chapter 4.3.1. The wavelength $\lambda = 561\,\mathrm{nm}$ was opted (instead of $532\,\mathrm{nm}$) because this wavelength is conveniently coupled into the excitation path by an additional dichroic mirror (Fig. 4.21) and closer to the excitation maximum of the NV centers. To obtain an useful image, the fluorescence from the centers, excited by this yellow probe beam, has to be separated from the fluorescence signal produced by the doughnut-shaped excitation beam. Otherwise both signals would contribute to the image and thus any useful information would be lost. Modulating the probe beam at $1\,\mathrm{kHz}$ with a beam chopper and recording the elicited fluorescence with a lock-in amplifier ($10\,\mathrm{ms}$ time constant; Model 7265, Signal Recovery, Wokingham, United Kingdom) extracted the
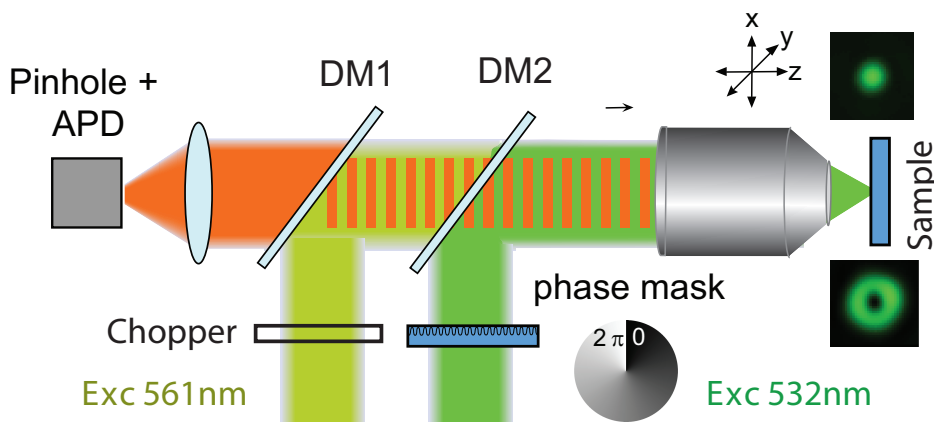

Figure 4.21: Modified setup for direct GSD microscopy. Same setup as in Figure 4.14 with additional laser beam at 561nm which is modulated by a chopper wheel.

signal from the Δr-sized region at the doughnut minimum.

For this measurement the lock-in amplifier is not as essential as for the experiments presented in chapters 2 and 3, because the fluctuations in the recorded fluorescence signal are stemming from photon shot noise which noise spectrum is white meaning it has no spectral dependence. Therefore the lock-in amplifier does not improve the noise level because the signal is already only limited by shot noise. However, the rapid modulation eliminates unwanted effects, like signal changes due to drift, which act on slower time scales. Moreover, the phase sensitive detection performed by the lock-in amplifier would allow, in case the wanted signal exceeds the noise level, to distinguish whether the recorded signal is due to a wanted signal with fixed phase or uncorrelated noise with random phase with respect to the reference.
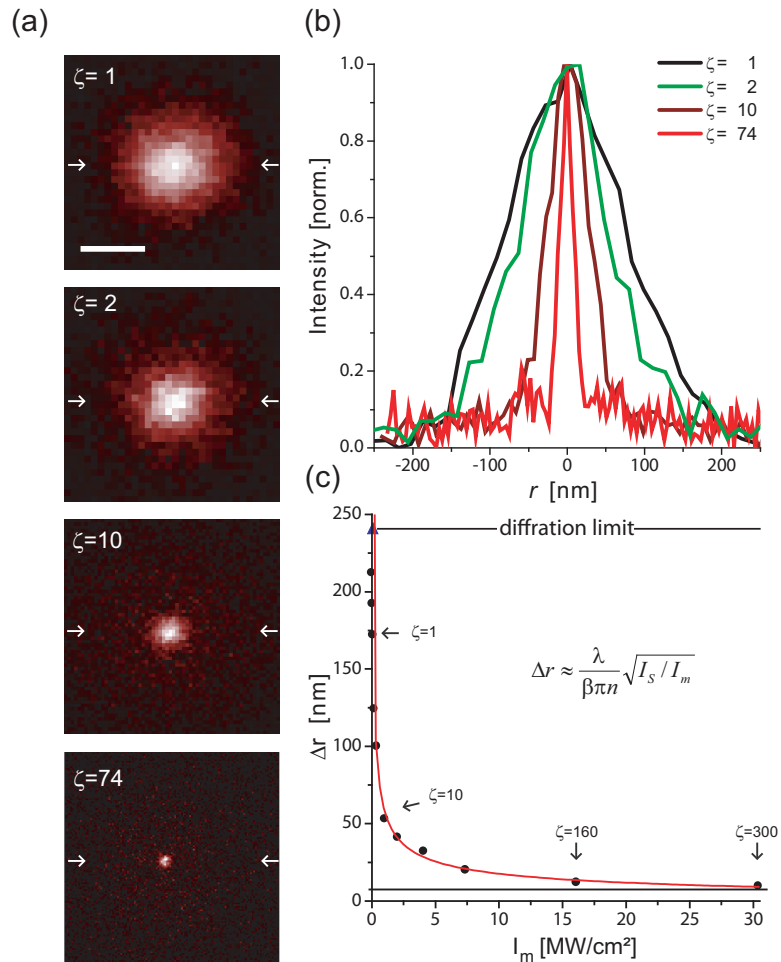

Figure 4.22: Direct GSD effective PSFs probed by single color centers. a) Increasing $I_{\mathrm{m}}/I_{\mathrm{S}} = \zeta$ renders PSFs with decreasing FWHM Δr, as quantified in b) by the normalized line profiles. c) Δr scales inversely with $\sqrt{I_{\mathrm{m}}/I_{\mathrm{S}}}$ approaching 9.5 nm in this experiment. Scale bar in (a) is 150 nm
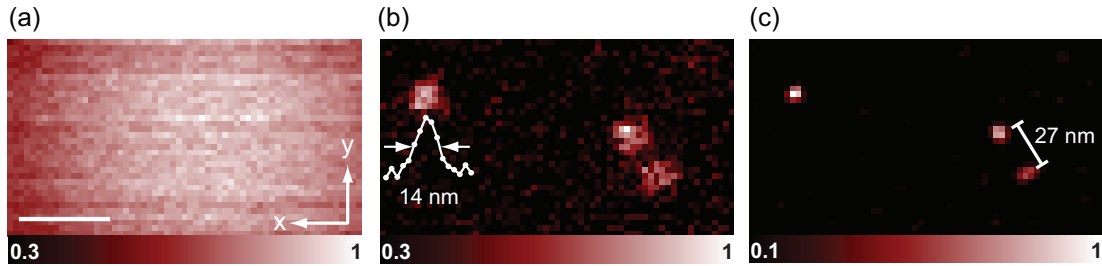
Figure 4.23: Direct GSD nanoscopy of diamond color centers. While the a) confocal image ($\Delta r \approx 212$ nm) is featureless, the 14 nm spatial resolution of the corresponding direct GSD image shown in b) reveals three color centers; two of them are 27 nm apart. c) Image after positivity-constrained deconvolution. Scale bar is 150 nm.

Results

The effective PSF is written as $h_{\text{eff}}(r, I_{\text{m}}) = h_{\text{det}}(r)[1 - \eta(I(r))]$, with a FWHM Δr given by equation (4.26). Imaging individual NV centers (Fig. 4.22) resulted in positive images which revealed the experimental PSF. Fitting equation (4.26) with $\beta = 0.35$ and $\varepsilon \approx 0$ to the measured Δr validated again the increase in resolution proportional to $\sqrt{I_{\text{m}}/I_{\text{S}}}$.

Figure 4.23 compares a confocal recording with its GSD counterpart delivering direct images at $\Delta r = 14$ nm. The GSD image is the sum of three subsequent recordings with a pixel dwell time of 25 ms. The 15-fold increase in focal plane resolution over confocal ($\Delta r = 212$ nm) directly discerns individual NV centers located only 27 nm apart without any data processing (Fig. 4.23b). Yet applying a nonlinear Richardson-Lucy deconvolution [105] further improves the contrast in the image (Fig. 4.23c).

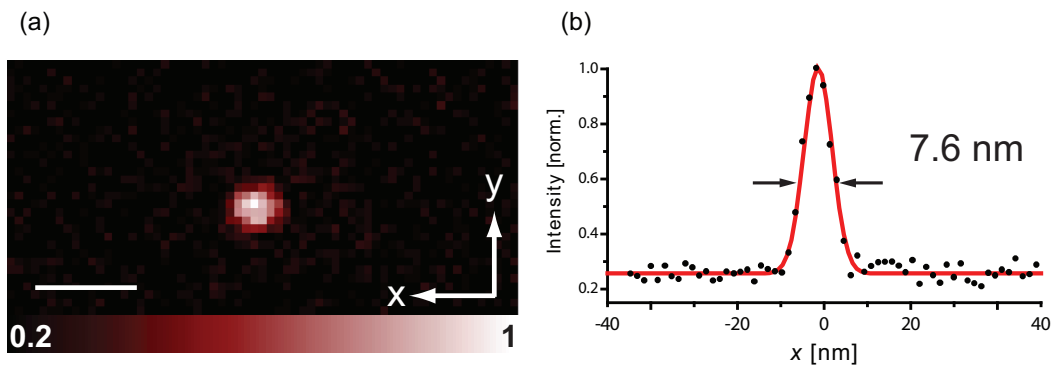The limits set by ε can be lessened by replacing the CW beam with pulses

Figure 4.24: Effective PSF in direct GSD nanoscopy optimized. a) Image of a single NV center obtained by summing 7 consecutive recordings; b) line profile along x-axis proves resolution potential of $\Delta r = 7.6$ nm as an upper limit. Scale bar is 20 nm.

shorter than the lifetime of the targeted excited state. In this case the fluorescence on-switching by GSD follows $\exp(-I/I_{\mathrm{S}})$, as in ideal STED. Pulsed illumination also affords higher I_{m} at moderate average power. However, these high peak intensities involve also unwanted effects such as drift as shown in the previous subsection. ε can also be minimized by removing aberrations, as was exerted for recording the direct GSD image (Fig. 4.24) of a single NV center at $I_{\mathrm{m}}/I_{\mathrm{S}} = 910$. Representing an effective PSF of $\Delta r = 7.6\,\mathrm{nm}$, the image proves the ability of direct GSD to image with single digit nanometer resolution.

4.3.3 Discussion

Due to the way it is produced, the doughnut actually assumes a tubular shape extending in the z-direction [106]. Consequently, increasing I_{m} also imparts larger intensities in the z-direction. In the negative imaging case, defects located above and below the focal plane are then increasingly captured by the doughnut, meaning that the axial resolution deteriorates. Moreover, since the I_{m} in a particular xy-plane decreases with increasing z, Δr decreases accordingly. Given that the features are single centers, their z-position can be derived from the defocus, especially if the doughnut bears a z-dependent aberration such as astigmatism. In contrast, featuring a confocal detection path, the direct GSD modality discriminates the focal plane approximately with a depth of λ, thus providing 3D imaging like a confocalized STED setup. However, unlike the latter, the direct GSD modality can be operated with a single wavelength because it employs just excitation, i.e. on-switching. Unfortunately, this convenience also poses challenges because weakly fluorescent objects are difficult to discern from bright neighbors with inherently large absolute noise levels. STED microscopy has an advantage in this regard, because decreasing the on-state area by off-switching affords measurement against low background.

Chapter 5

Conclusion and outlook

This work demonstrates a resolving power of down to 6 nm in the optical far-field obtained with STED and GSD microscopy of densely packed diamond color centers. Corresponding to $\lambda/135$, it is currently the highest resolution achieved with focused light in unprocessed recordings. Furthermore, the NV color centers remain photostable even under the intense laser light employed for these techniques. This implies the possibility to image at the nanoscale with no change in brightness or resolution for virtually unlimited number of recordings, which before was believed to be impossible.

To establish the parameters for achieving highest resolution, the mechanisms for fluorescence switching were studied for a range of fluorophores ranging from dyes and fluorescent proteins over semiconductor nanocystals to crystal color centers. The process responsible for the optically induced transition between the utilized bright and dark state, an essential prerequisite for sub-diffraction resolution, was clarified for all these systems. In case of the fluorescent dyes and proteins employed in STED microscopy, clearly stimulated emission is the responsible mechanism, while for Mn-doped quantum dots the fluorescence is modulated through excited state absorption. The nitrogen vacancy (NV) color center in diamond was identified as a fluorescent system which is very promising for high resolution recordings due to its enormous photostability and the effective control over its fluorescence by stimulated emission. STED microscopy yields images of these color centers with nanometric resolution and Ångström precision. Thus STED provides a tool for obtaining position information of these color centers with atomic accuracy. At present, in the field of quantum computing, with the goal to realize Q-bit arrays, strong efforts are made to implant NV centers directed at well defined positions in diamond crystals [59, 60]. The imaging techniques presented in this thesis are currently the only methods available for the characterization of such samples.

The imaging and resolution measurements of NV color centers demonstrated a nearly ideal implementation of STED and GSD microscopy. The experiments met the theoretical predictions for these concepts and could be verified on single

centers even at high intensities, due to their brightness and photostability.

Furthermore, it was shown that a temperature increase produced by absorption can provide an imaging contrast mechanism to visualize strong absorbers. The experimental findings, however, were not encouraging enough to apply this technique to nanoscopy of biological specimens. For example, a large endogenous background signal stemming from mitochondria was observed while the signal of the inserted chromophores was not sufficient above background. This technique may find its niche in long-time particle tracking using gold nanoparticles which are very strong absorbers and stable. Nonetheless, fluorescence microscopy has the compelling advantage of background-free detection. Once diamond nanocrystals of a few nanometers in size are realized with specific labeling, a new class of fluorescent markers will be available which should enable fluorescence imaging without bleaching at the nanoscale.

The limits of nanoscopy have not yet been reached. Applying a shorter STED wavelength entailing a larger stimulated emission cross section should increase the resolution even further. Minimizing the intensity of the doughnut center ($\varepsilon \ll 10^{-4}$) should enable a further "spot sharpening" by more than a factor of 10, which may reach or even surpass the dimensions of the electron cloud. In this case, the dipole approximation would no longer hold, and thus open up the fascinating prospect of sensing the size of the cloud and its immediate environment. It would also be desirable to investigate STED on nitrogen vacancy centers subject to magnetic and microwave fields. In particular, reading out nitrogen vacancy centers and hence local magnetic fields on the nanoscale should be easier with STED and conventional lenses than with nanosized optical tips. Thus, STED microscopy may greatly simplify nanoscale magnetic imaging [50, 49]. It will also be interesting to apply STED nanoscopy to other color centers and crystals. The achieved and future gains in all-physics-based resolution should also open novel experimental avenues in applied and fundamental quantum optics.

Appendix A

Lock in detection

Each measurement has the goal to determine a physical property with the best accuracy. To improve the signal to noise ratio (SNR) one can improve the signal (e.g. better adjustment) or decrease the noise level (e.g. cooling or shielding). If these possibilities are exhausted, a phase sensitive measurement can be used to improve the SNR [107]. The prerequisite for that is a modulation of the signal with a fixed frequency and phase $s(t) = A_s \sin(\omega_s t + \phi_s)$. A phase sensitive instrument functions as a narrow frequency filter which isolates the signal and suppresses the noise components. A lock-in amplifier is an electronic device which realizes such a phase sensitive measurement. With this kind of tool it is possible to detect signals which are by many orders of magnitude smaller than the noise level.

Basic principle

A lock-in amplifier basically consists of a pre-amplifier, a phase shifter, a phase sensitive detector and a low pass filter (Fig. A.1). The pre-amplifier can be adjusted and is used to amplify small signals to exploit the full voltage range of the lock-in output.

The phase sensitive detector is the key element of the lock-in amplifier. It multiplies the signal with the reference signal $r(t) = A_r \sin(\omega_r t + \phi_r)$:

$$
\begin{aligned}
r(t) \cdot s(t) &= A_r A_s \cdot \sin(\omega_r t + \phi_r) \cdot \sin(\omega_s t + \phi_s) \\
&= A_r A_s [\cos((\omega_r + \omega_s)t + \phi_r + \phi_s) - \cos((\omega_r - \omega_s)t + \phi_r - \phi_s)] \\
&= A_r A_s [\cos(\omega_+ t + \phi_r + \phi_s) - \cos(\omega_- t + \phi)]
\end{aligned}
$$

with $\omega_+ = (\omega_r + \omega_s)$, $\omega_- = (\omega_r - \omega_s)$ and $\phi = (\phi_r - \phi_s)$.

The signal component which frequency matches the reference frequency is transferred to zero frequency yielding a DC signal. This signal can be filtered out by the low pass filter. For an infinitely sharp filter this would correspond to a perfect Fourier transformation extracting the amplitude of the signal of interest. Because in reality one cannot integrate forever, the bandwidth is finite. Thus the
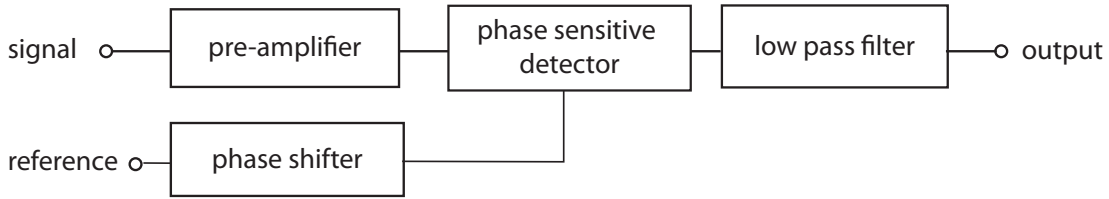
Figure A.1: Schematic diagram of a lock-in amplifier.

noise components which fall within the bandwidth of the low pass filter around ω_r are contributing to the measured signal. It follow from the above expression that the output signal is proportional to the phase $U_{\text{out}} \propto \cos(\phi)$. To achieve maximal output signal the phase shifter has to be set or rather controlled to $\phi = 0$. Depending on the noise sources the noise components are not equally distributed over the spectrum. Therefore the reference frequency can be chosen from a spectral region with low noise to improve the SNR significantly. The SNR is improved with rising time constant of the low pass filter $\tau = R \cdot C$ which yields an SNR $\propto \sqrt{\tau}$.

In case the modulated signal is not a sinus wave e.g. a rectangular signal, the modulation is composed of many frequency components. The Fourier series of a rectangular wave is:

$$s(t) = \frac{4}{\pi} \sum_{n=0}^{\infty} \frac{1}{2n+1} \sin((2n+1)\omega t) \tag{A.1}$$

The lock-in detector extracts the frist harmonic of the signal. The effective voltage would be $U_{\text{eff}} = \frac{4}{\pi\sqrt{2}}$. If the Peak-to-Peak value of the rectangular signal equals 1 V, the voltage at the lock-in output is going to be half of the effective voltage which would be 450 mV.

Appendix B

Mn-doped ZnSe quantum dots

Quantum dot (QD) nanocrystals are an important class of fluorescent markers as they have the advantages of enhanced photostability, high quantum yield, and macromolecular size [42]. Furthermore, the ability to tune the QD fluorescence, either by changing their size [42] or by doping [108], allows for multiplexed imaging.

Upon QD excitation an electron is elevated from the valance band to the conduction band creating an electron hole pair (exciton). Because the emission photons are produced by recombination from the lowest level of the conduction band, the emission and excitation spectra overlap. Therefore, it is not possible to quench QD fluorescence by stimulated emission due to excitation by the STED beam.

However, it is possible to control the properties of the nanocrystals by doping. In Figure B.1 the energy levels and spectra of doped ZnSe quantum dots (NN-Labs, Fayetteville, AR, USA) are depicted. For this material a small amount of manganese ions Mn^{2+} is incorporated into the lattice of the host semiconductor.
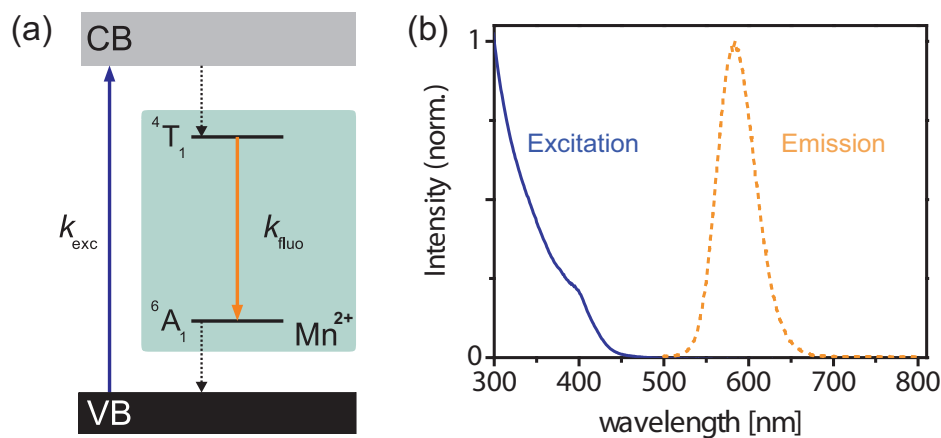

Figure B.1: Energy diagram of Mn-doped ZnSe quantum dots (a) and their excitation as well as emission spectrum (b).

The host semiconductor absorbs light and transfers the energy to the atomic levels of the dopant which than emit the fluorescence photons. The luminescence transition from $^4T_1$ to $^6A_1$ near 590 nm has an energy difference smaller than the bandgap of the host material yielding a pronounced Stoke's shift. These spectral properties seem to be promising for their application to STED microscopy. Figure B.2 shows the fluorescence decay which shows three decay regimes of 2 μs, 21 μs, and 90 μs.

It has been shown that it is possible to directly control the fluorescence of these Mn-doped ZnSe quantum dots to implement subdiffraction imaging [43]. The underlying quenching mechanism is not stimulated emission. The process is based on excited state absorption as described in subsection 2.3.1.
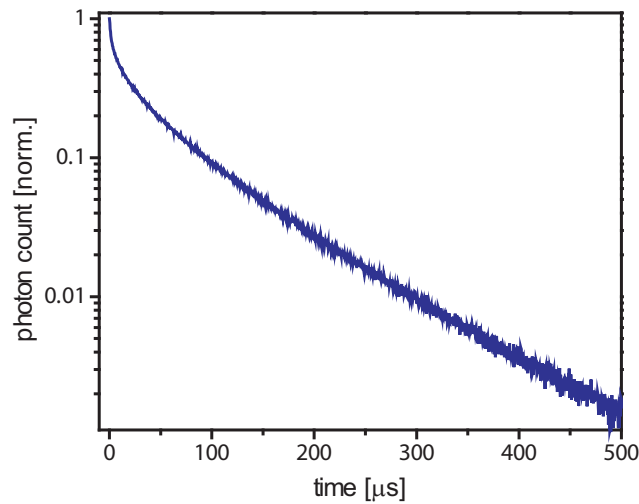

Figure B.2: Semi-logarithmic plot of the fluorescence decay for Mn-doped ZnSe quantum dots.

Appendix C

Stimulated emission cross section

To obtain the stimulated emission cross section three independent measurements have to be carried out: the fluorescent lifetime τ_{fl}, the fluorescence quantum yield Q and the wavelength dependence of the fluorescence $E(\lambda)$. This function is normalized that the integral over all wavelengths is equal to the quantum yield:

$$Q = \int E(\lambda)\,\mathrm{d}\lambda, \tag{C.1}$$

$E(\lambda)$ determines the probability that the fluorophore emits in a given wavelength interval $\mathrm{d}\lambda$. The rate for spontaneous emission P_{fl} for a given wavelength is the product of this function and the decay rate of the excited stated of the fluorphore $k_{\mathrm{fl}} = 1/\tau_{\mathrm{fl}}$:

$$P_{\mathrm{fl}}(\lambda)\,\mathrm{d}\lambda = 1/\tau_{\mathrm{fl}} E(\lambda)\,\mathrm{d}\lambda. \tag{C.2}$$

This rate can also be described as the product of the density of photon states in free space $\rho(\lambda)\,\mathrm{d}\lambda$ and a expression $M(\lambda)$ which only depends on parameters characteristic to the molecule, such as the internal density of states and the transition matrix [23, 109]:

$$P_{\mathrm{fl}}(\lambda)\,\mathrm{d}\lambda = M(\lambda)\rho(\lambda)\,\mathrm{d}\lambda. \tag{C.3}$$

The gain of photons by stimulated emission $\mathrm{d}N_{\mathrm{ph}}/\mathrm{d}t$ with a given wavelength is equal to the same molecular function $M(\lambda)$ times the number of photons $N(\lambda)$ incident on the fluorophore times the volume density of excited fluorophores n_1:

$$\frac{\mathrm{d}N_{\mathrm{ph}}(\lambda)}{\mathrm{d}t} = M(\lambda)N_{\mathrm{ph}}(\lambda)n_1. \tag{C.4}$$

Substituting,

$$\frac{\mathrm{d}N_{\mathrm{ph}}(\lambda)}{\mathrm{d}t} = \frac{E(\lambda)}{\tau_{\mathrm{fl}}\rho(\lambda)}N_{\mathrm{ph}}(\lambda)n_1. \tag{C.5}$$

The density of photon states in free space is given by

$$\rho(\lambda) = 8\pi n^3/\lambda^4, \tag{C.6}$$

where n is the index of refraction. The gain in photons by stimulated emission per unit length is given by the cross section times the number of incident photons times the volume density of excited fluorophores:

$$\frac{\mathrm{d}N_{\mathrm{ph}}(\lambda)}{\mathrm{d}x} = \sigma_{em}(\lambda)N_{\mathrm{ph}}(\lambda)n_1. \tag{C.7}$$

Thus, the relation for the stimulated emission cross section and experimentally measurable quantities, using

$$\frac{\mathrm{d}N_{\mathrm{ph}}(\lambda)}{\mathrm{d}t} = v\frac{\mathrm{d}N_{\mathrm{ph}}(\lambda)}{\mathrm{d}x}, \tag{C.8}$$

where v is the propagation velocity, which equals c/n, where c is the velocity of light in vacuum, is

$$\sigma_{\mathrm{em}}(\lambda) = \frac{\lambda^4 E(\lambda)}{8\pi c n^2 \tau_{\mathrm{fl}}}. \tag{C.9}$$

From this expression follows that the fluorescence spectrum declines faster to longer wavelengths than that of the stimulated emission cross section due to the wavelengths dependence to the power of four. This can be seen clearly in Figure C.1. This is favorable for STED microscopy because often the STED wavelength is chosen from the red spectral region to avoid excitation due to the STED beam and to leave a large detection window.
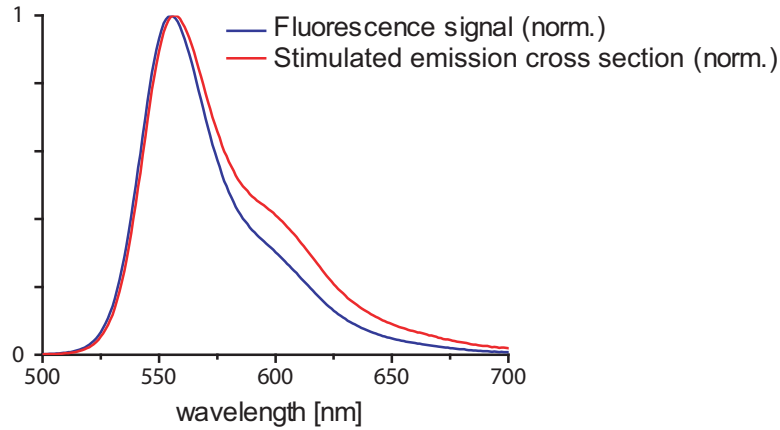

Figure C.1: Wavelength dependence of the fluorescence signal and the stimulated emission cross section of the dye ATTO 532.

Bibliography

[1] Einstein, A. *The motion of elements suspended in static liquids as claimed in the molecular kinetic theory of heat.* Annalen der Physik, **17**(1905)(8):549–560.

[2] Abbe, E. *Beiträge zur Theorie des Mikroskops und der mikroskopischen Wahrnehmung.* Archiv für mikroskopische Anatomie, **9**(1873):413–468.

[3] Knoll, M. and Ruska, E. *Das Elektronenmikroskop.* Zeitschrift für Physik, **78**(1932):318–339.

[4] Synge, E. *A suggested method for extending microscopic resolution into the ultra-microscopic region.* Philosophical Magazine, **6**(1928):356.

[5] Ash, E. A. and Nichols, G. *Super-resolution aperture scanning microscope.* Nature, **237**(1972):510–512.

[6] Lewis, A., Isaacson, M., Harootunian, A., and Murray, A. *Development of a 500 Å resolution light microscope.* Ultramicroscopy, **13**(1984):227–231.

[7] Pohl, D. W., Denk, W., and Lanz, M. *Optical stethoscopy: Image recording with resolution $\lambda/20$.* Applied Physics Letters, **44**(1984):651–653.

[8] Hell, S. W. *Microscopy and its focal switch.* Nature Methods, **6**(2008)(1):24–32.

[9] Hell, S. W. and Wichmann, J. *Breaking the diffraction resolution limit by stimulated emission: stimulated emission depletion fluorescence microscopy.* Optics Letters, **19**(1994)(11):780–782.

[10] Hein, B., Willig, K., and Hell, S. W. *Stimulated emission depletion (STED) nanoscopy of a fluorescent protein - labeled organelle inside a living cell.* Proceedings of the National Academy of Sciences of the United States of America, **105**(2008)(38):14271–14276.

[11] Schmidt, R., Wurm, C. A., Jakobs, S., Engelhardt, J., Egner, A., and Hell, S. W. *Spherical nanosized focal spot unravels the interior of cells.* Nature Methods, **5**(2008)(6):539–544.

[12] Westphal, V., Rizzoli, S. O., Lauterbach, M. A., Kamin, D., Jahn, R., and Hell, S. W. *Video-rate far-field optical nanoscopy dissects synaptic vesicle movement.* Science, **320**(2008)(5873):246–249.

[13] Donnert, G., Keller, J., Wurm, C. A., Rizzoli, S. O., Westphal, V., Schönle, A., Jahn, R., Jakobs, S., Eggeling, C., and Hell, S. W. *Two-color far-field fluorescence nanoscopy.* Biophysical Jounal, **92**(2007)(8):L67–69L.

[14] Hell, S. W. and Kroug, M. *Ground-state depletion fluorescence microscopy, a concept for breaking the diffraction resolution limit.* Applied Physics B, **60**(1995):495–497.

[15] Hofmann, M., Eggeling, C., Jakobs, S., and Hell, S. *Breaking the diffraction barrier in fluorescence microscopy at low light intensities by using reversibly photoswitchable proteins.* Proceedings of the National Academy of Sciences of the United States of America, **102**(2005)(49):17565–17569.

[16] Gustafsson, M. G. L. *Nonlinear structured-illumination microscopy: Wide-field fluorescence imaging with theoretically unlimited resolution.* Proceedings of the National Academy of Sciences of the United States of America, **102**(2005)(37):13081–13086.

[17] Betzig, E., Patterson, G., Sougrat, R., Lindwasser, O., Olenych, S., Bonifacino, J., Davidson, M., Lippincott-Schwartz, J., and Hess, H. *Imaging intracellular fluorescent proteins at nanometer resolution.* Science, **313**(2006)(5793):1642–1645.

[18] Rust, M. J., Bates, M., and Zhuang, X. *Sub-diffraction-limit imaging by stochastic optical reconstruction microscopy (STORM).* Nature Methods, **3**(2006):793–796.

[19] Fölling, J., Bossi, M., Bock, H., Medda, R., Wurm, C. A., Hein, B., Jakobs, S., Eggeling, C., and Hell, S. W. *Fluorescence nanoscopy by ground-state depletion and single-molecule return.* Nature Methods, **5**(2008):943 – 945.

[20] Hell, S. W. *Far-field optical nanoscopy.* Science, **316**(2007)(5828):1153–1158.

[21] Dyba, M. and Hell, S. *Focal spots of size $\lambda/23$ open up far-field fluorescence microscopy at 33 nm axial resolution.* Physical Review Letters, **88**(2002):163901.

[22] Westphal, V. and Hell, S. *Nanoscale resolution in the focal plane of an optical microscope.* Physical Review Letters, **94**(2005):143903.

[23] Peterson, O. G., Webb, J. P., Mccolgin, W. C., and Eberly, J. H. *Organic dye laser threshold.* Journal of Applied Physics, **42**(1971)(5):1917.

[24] Lakowicz, J. R., Gryczynski, I., Kusba, J., and Bogdanov, V. *Light quenching of fluorescence - a new method to control the excited-state lifetime and orientation of fluorophores.* Photochemistry and Photobiology, **60**(1994)(6):546.

[25] Gryczynski, I., Kusba, J., Gryczynski, Z., Malak, H., and Lakowicz, J. R. *Effect of fluorescence quenching by stimulated emission on the spectral properties of a solvent-sensitive fluorophore.* Journal of Physical Chemistry, **100**(1996)(24):10135.

[26] Didier, P., Guidoni, L., Schwalbach, G., Bourotte, M., Follenius-Wund, A., Pigault, C., and Bigot, J. Y. *Ultrafast gain dynamics of the green fluorescent protein.* Chemical Physics Letters, **364**(2002)(5-6):503.

[27] Winkler, K., Lindner, J. R., Subramaniam, V., Jovin, T. M., and Vohringer, P. *Ultrafast dynamics in the excited state of green fluorescent protein (wt) studied by frequency-resolved femtosecond pump-probe spectroscopy.* Physical Chemistry Chemical Physics, **4**(2002)(6):1072.

[28] Iketaki, Y., Watanabe, T., Ishiuchi, S., Sakai, M., Omatsu, T., Yamamoto, K., Fujii, M., and Watanabe, T. *Investigation of the fluorescence depletion process in the condensed phase; application to a tryptophan aqueous solution.* Chemical Physics Letters, **372**(2003)(5-6):773.

[29] Iketaki, Y., Watanabe, T., Sakai, M., Ishiuchi, S., Fujii, M., and Watanabe, T. *Theoretical investigation of the point-spread function given by super-resolving fluorescence microscopy using two-color fluorescence dip spectroscopy.* Optical Engineering, **44**(2005)(3):033602.

[30] Iketaki, Y., Watanabe, T., Bokor, N., and Fujii, M. *Construction of super-resolution microscope based on cw laser light source.* Review of Scientific Instruments, **77**(2006)(6):063112.

[31] Watanabe, T., Iketaki, Y., Sakai, M., Ohmori, T., Ueda, T., Yamanaka, T., Ishiuchi, S. I., and Fujii, M. *Analysis of a fluorescence depletion process of Rhodamine 6G in a PMMA matrix induced by nano- and picosecond lasers.* Chemical Physics Letters, **420**(2006)(4-6):410.

[32] Gumy, J. C. and Vauthey, E. *Picosecond polarization grating study of the effect of excess excitation energy on the rotational dynamics of Rhodamine 6G in different electronic states.* Journal of Physical Chemistry, **100**(1996)(21):8628.

[33] Alekseev, V. A., Denisov, L. K., Kozintsev, V. I., Kozlov, N. A., and Sopin, A. I. *Investigation of the temperature dependence of the lasing characteristics of a dye laser with lamp pumping.* Journal of Applied Spectroscopy, **31**(1979)(1):51.

[34] Huth, B. G., Farmer, G. I., and Kagan, M. R. *Temperature-dependent measurements of a flashlamp-pumped dye laser.* Journal of Applied Physics, **40**(1969)(13):5145.

[35] Wieder, I. *Quenching of laser dye fluorescence by absorption from an excited singlet state.* Applied Physics Letters, **21**(1972)(7):318.

[36] Hobbs, P. C. D. *Ultrasensitive laser measurements without tears.* Applied Optics, **36**(1997)(4):903.

[37] Donnert, G., Keller, J., Medda, R., Andrei, M. A., Rizzoli, S. O., Lurmann, R., Jahn, R., Eggeling, C., and Hell, S. W. *Macromolecular-scale resolution in biological fluorescence microscopy.* Proceedings of the National Academy of Sciences of the United States of America, **103**(2006)(31):11440.

[38] Willig, K. I., Rizzoli, S. O., Westphal, V., Jahn, R., and Hell, S. W. *STED microscopy reveals that synaptotagmin remains clustered after synaptic vesicle exocytosis.* Nature, **440**(2006)(7086):935.

[39] Willig, K. I., Kellner, R. R., Medda, R., Hein, B., Jakobs, S., and Hell, S. W. *Nanoscale resolution in GFP-based microscopy.* Nature Methods, **3**(2006)(9):721.

[40] Mauck, M. *Nanoscale resolution in GFP-based microscopy.* Applied Optics, **18**(1979)(5):599.

[41] Thiel, E. R. *Eigenschaften angeregter Rhodamin-Farbstoffe und deren Wirkung im Farbstofflaser.* Habilitationsschrift, Universität Siegen 1995.

[42] Michalet, X., Pinaud, F. F., Bentolila, L. A., Tsay, J. M., Doose, S., Li, J. J., Sundaresan, G., Wu, A. M., Gambhir, S. S., and Weiss, S. *Quantum dots for live cells, in vivo imaging, and diagnostics.* Science, **307**(2005)(5709):538–544.

[43] Irvine, S. E., Staudt, T., Rittweger, E., Engelhardt, J., and Hell, S. W. *Direct light-driven modulation of luminescence from Mn-doped ZnSe quantum dots.* Angewandte Chemie, **47**(2008)(14):2685–2688.

[44] Clausen, R. and Petermann, K. *Mn-2+ as a potential solid-state laser ion.* IEEE Journal of Quantum Electronics, **24**(1988)(6):1114–1117.

[45] Zaitsev, A. M. *Optical properties of diamond: A data handbook.* Springer, Berlin 2001.

[46] Gruber, A., Dräbenstedt, A., Tietz, C., Fleury, L., Wrachtrup, J., and von Borczyskowski, C. *Scanning confocal optical microscopy and magnetic resonance on single defect centers.* Science, **276**(1997):2012–2014.

[47] Kurtsiefer, C., Mayer, S., Zarda, P., and Weinfurter, H. *Stable solid-state source of single photons.* Physical Review Letters, **85**(2000)(2):290–293.

[48] Greentree, A. D., Fairchild, B. A., Hossain, F. M., and Prawer, S. *Diamond integrated quantum photonics.* Materials Today, **11**(2008)(9):22–31.

[49] Maze, J. R., Stanwix, P. L., Hodges, J. S., Hong, S., Taylor, J. M., Capellaro, P., Jiang, L., Gurudev Dutt, M. V., Togan, E., Zibrov, A. S., Yacoby, A., Walsworth, R. L., and Lukin, M. D. *Nanoscale magnetic sensing with an individual electronic spin in diamond.* Nature, **455**(2008):644–647.

[50] Balasubramanian, G., Chan, I. Y., Kolesov, R., Al-Hmoud, M., Tisler, J., Shin, C., Kim, C., Wojcik, A., Hemmer, P. R., Krueger, A., Hanke, T., Leitenstorfer, A., Bratschitsch, R., Jelezko, F., and Wrachtrup, J. *Nanoscale imaging magnetometry with diamond spins under ambient conditions.* Nature, **455**(2008):648–651.

[51] Fu, C. C., Lee, H. Y., Chen, K., Lim, T. S., Wu, H. Y., Lin, P. K., Wei, P. K., Tsao, P. H., Chang, H. C., and Fann, W. *Characterization and application of single fluorescent nanodiamonds as cellular biomarkers.* Proceedings of the National Academy of Sciences of the United States of America, **104**(2007)(3):727–732.

[52] Chao, J. I., Perevedentseva, E., Chung, P. H., Liu, K. K., Cheng, C. Y., Chang, C. C., and Cheng, C. L. *Nanometer-sized diamond particle as a probe for biolabeling.* Biophysical Journal, **93**(2007)(6):2199–2208.

[53] Gaebel, T., Domhan, M., Popa, I., Wittmann, C., Neumann, P., Jelezko, F., Rabeau, J. R., Stavrias, N., Greentree, A. D., Prawer, S., Meijer, J., Twamley, J., Hemmer, P. R., and Wrachtrup, J. *Room-temperature coherent coupling of single spins in diamond.* Nature Physics, **2**(2006):408 – 413.

[54] Clark, C. D. and Norris, C. A. *Photoluminescence associated with 1.673, 1.944 and 2.498 eV centres in diamond.* Journal of Physics Part C, **4**(1971)(14):2223.

[55] Davies, G. and Hamer, M. F. *Optical Studies of 1.945 eV Vibronic Band in Diamond.* Proceedings of the Royal Society of London Series a-Mathematical Physical and Engineering Sciences, **348**(1976)(1653):285–298.

[56] Lin, C. K., Chang, H. C., and Lin, S. H. *Symmetric double-well potential model and its application to vibronic spectra: Studies of inversion modes of ammonia and nitrogen-vacancy defect centers in diamond.* Journal of Physical Chemistry A, **111**(2007)(38):9347–9354.

[57] Manson, N. B., Harrison, J. P., and Sellars, M. J. *Nitrogen-vacancy center in diamond: Model of the electronic structure and associated dynamics.* Physical Review B, **74**(2006)(10).

[58] Jelezko, F. and Wrachtrup, J. *Single defect centres in diamond: a review.* Physica Status Solidi A, **203**(2006):3207–3225.

[59] Meijer, J., Pezzagna, S., Vogel, T., Burchard, B., Bukow, H. H., Rangelow, I. W., Sarov, Y., Wiggers, H., Plumel, I., Jelezko, F., Wrachtrup, J., Schmidt-Kaler, F., Schnitzler, W., and Singer, K. *Towards the implanting of ions and positioning of nanoparticles with nm spatial resolution.* Applied Physics A, **91**(2008)(4):567–571.

[60] Schnitzler, W., Linke, N. M., Fickler, R., Meijer, J., Schmidt-Kaler, F., and Singer, K. *Deterministic ultracold ion source targeting the Heisenberg limit.* Physical Review Letters, **102**(2009)(7).

[61] Wrachtrup, J. and Jelezko, F. *Processing quantum information in diamond.* Journal of Physics-Condensed Matter, **18**(2006)(21):S807–S824.

[62] Kastrup, L. and Hell, S. W. *Absolute optical cross section of individual fluorescent molecules.* Angewandte Chemie, **43**(2004):6646–6649.

[63] Tokeshi, M., Uchida, M., Hibara, A., Sawada, T., and Kitamori, T. *Determination of subyoctomole amounts of nonfluorescent molecules using a thermal lens microscope: Subsingle molecule determination.* Analytical Chemistry, **73**(2001)(9):2112–2116.

[64] Boyer, D., Tamarat, P., Maali, A., Lounis, B., and Orrit, M. *Photothermal imaging of nanometer-sized metal particles among scatterers.* Science, **297**(2002)(5584):1160–1163.

[65] Berciaud, S., Cognet, L., Blab, G. A., and Lounis, B. *Photothermal heterodyne imaging of individual nonfluorescent nanoclusters and nanocrystals.* Physical Review Letters, **93**(2004)(25).

[66] Berciaud, S., Lasne, D., Blab, G. A., Cognet, L., and Lounis, B. *Photothermal heterodyne imaging of individual metallic nanoparticles: Theory versus experiment.* Physical Review B, **73**(2006)(4).

[67] Carslaw, H. S. and Jaeger, J. C. *Conduction of heat in solids.* Oxford University Press, Oxford 1959.

[68] Hawkes, J. B. and Astheimer, R. W. *The temperature coefficient of the refractive index of Water.* Journal of the Optical Society of America, **38**(1948)(9):804–806.

[69] Fujii, M., Zhang, X., Imaishi, N., Fujiwara, S., and Sakamoto, T. *Simultaneous measurements of thermal conductivity and thermal diffusivity of liquids under microgravity conditions.* International Journal of Thermophysics, **18**(1997)(2):327–339.

[70] Bernhardt, A. and P., R. *Design criteria and opterating characteristics of single-mode pulsed dye laser.* Applied Physics B, **26**(1981):141.

[71] Pawley, J. B. *Handbook of biological confocal microscopy.* Springer, New York 1985.

[72] Sibbett, W. and Taylor, J. R. *Picosecond pulse generation in a passively mode-locked green-dye laser.* Optics Communications, **43**(1982)(1):50–52.

[73] Sibbett, W. and Taylor, J. R. *Passive-mode locking of flashlamp-pumped dye-lasers in the 508-583 nm range.* IEEE Journal of Quantum Electronics, **19**(1983)(4):558–561.

[74] French, P. M. W. and Taylor, J. R. *Passively mode-locked continuous-wave Rhodamine-110 dye-laser.* Optics Letters, **11**(1986)(5):297–299.

[75] Fang, R. Z., Vanrheenen, A. D., Vanderziel, A., Young, A. C., and Vanderziel, J. P. *1/f Noise in double-heterojunction AlGaAs/GaAs laser-Diodes on GaAs and on Si-substrates.* Journal of Applied Physics, **68**(1990)(8):4087–4090.

[76] Shimomura, O., Johnson, F. H., and Saiga, Y. *Purification and properties of cypridina luciferase.* Journal of Cellular and Comparative Physiology, **58**(1961)(2):113–.

[77] Prasher, D. C., Eckenrode, V. K., Ward, W. W., Prendergast, F. G., and Cormier, M. J. *Primary structure of the aequorea-victoria green-fluorescent protein.* Gene, **111**(1992)(2):229–233.

[78] Tsien, R. Y. *The green fluorescent protein.* Annual Review of Biochemistry, **67**(1998):509–544.

[79] Lukyanov, K. A., Fradkov, A. F., Gurskaya, N. G., Matz, M. V., Labas, Y. A., Savitsky, A. P., Markelov, M. L., Zaraisky, A. G., Zhao, X. N., Fang, Y., Tan, W. Y., and Lukyanov, S. A. *Natural animal coloration can be determined by a nonfluorescent green fluorescent protein homolog.* Journal of Biological Chemistry, **275**(2000)(34):25879–25882.

[80] Andresen, M., Wahl, M. C., Stiel, A. C., Grater, F., Schafer, L. V., Trowitzsch, S., Weber, G., Eggeling, C., Grubmuller, H., Hell, S. W., and Jakobs, S. *Structure and mechanism of the reversible photoswitch of a fluorescent protein.* Proceedings of the National Academy of Sciences of the United States of America, **102**(2005)(37):13070–13074.

[81] Lasne, D., Blab, G. A., De Giorgi, F., Ichas, F., Lounis, B., and Cognet, L. *Label-free optical imaging of mitochondria in live cells.* Optics Express, **15**(2007)(21):14184–14193.

[82] Sheetz, M. P., Turney, S., Qian, H., and Elson, E. L. *Nanometer-Level Analysis Demonstrates That Lipid Flow Does Not Drive Membrane Glycoprotein Movements.* Nature, **340**(1989)(6231):284–288.

[83] Ye, T., Fischer, M., Yurtsever, G., and Warren, W. S. *Two-photon absorption microscopy of tissue.* 2005 Conference on Lasers and Electro-Optics (CLEO), Vols 1-3, pages 1512–1514.

[84] Dan, F., Tong, Y., Matthews, T. E., Chen, B. J., Yurtserver, G., and Warren, W. S. *High-resolution in vivo imaging of blood vessels without labeling.* Optics Letters, **32**(2007)(18):2641–2643.

[85] Min, W., Lu, S., Chong, S., Roy, R., Holtom, G. R., and Xie, X. S. *Imaging chromophores with undetectable fluorescence by stimulated emission microscopy.* Nature, **461**(2009)(461):1105–1109.

[86] Hell, S. W. *Improvement of lateral resolution in far-field light microscopy using two-photon excitation with offset beams.* Optics Communications, **106**(1994):19–24.

[87] Willig, K. I., Harke, B., Medda, R., and Hell, S. W. *STED microscopy with continuous wave beams.* Nature Methods, **4**(2007)(11):915–918.

[88] Heintzmann, R., Jovin, T. M., and Cremer, C. *Saturated patterned excitation microscopy - A concept for optical resolution improvement.* Journal of the Optical Society of America A, **19**(2002)(8):1599–1609.

[89] Enderlein, J. *Breaking the diffraction limit with dynamic saturation optical microscopy.* Applied Physics Letters, **87**(2005)(9).

[90] Fujita, K., Kobayashi, M., Kawano, S., Yamanaka, M., and Kawata, S. *High-resolution confocal microscopy by saturated excitation of fluorescence.* Physical Review Letters, **99**(2007)(22).

[91] Bretschneider, S., Eggeling, C., and Hell, S. W. *Breaking the diffraction barrier in fluorescence microscopy by optical shelving.* Physical Review Letters, **98**(2007):218103.

[92] Schermelleh, L., Carlton, P. M., Haase, S., Shao, L., Winoto, L., Kner, P., Burke, B., Cardoso, M. C., Agard, D. A., Gustafsson, M. G. L., Leonhardt, H., and Sedat, J. W. *Subdiffraction multicolor imaging of the nuclear periphery with 3D structured illumination microscopy.* Science, **320**(2008)(5881):1332–1336.

[93] Guizar-Sicairos, M., Thurman, S. T., and Fienup, J. R. *Efficient subpixel image registration algorithms.* Optics Letters, **33**(2008)(2):156–158.

[94] Heisenberg, W. *The physical principles of the quantum theory.* Chicago University Press, Chicago 1930.

[95] Bobroff, N. *Position measurement with a resolution and noise-limited instrument.* Review of Scientific Instruments, **57**(1986)(6):1152–1157.

[96] Yildiz, A., Forkey, J. N., McKinney, S. A., Ha, T., Goldman, Y. E., and Selvin, P. R. *Myosin V walks hand-over-hand: single fluorophore imaging with 1.5-nm localization.* Science, **300**(2003)(5628):2061–5.

[97] Kühn, S., Hettich, C., Schmitt, C., Poizat, J. P., and Sandoghdar, V. *Diamond colour centres as a nanoscopic light source for scanning near-field optical microscopy.* Journal of Microscopy, **202**(2001)(1):2–6.

[98] Gordon, M. P., Ha, T., and Selvin, P. R. *Single-molecule high-resolution imaging with photobleaching.* Proceedings of the National Academy of Sciences of the United States of America, **101**(2004):6462–6465.

[99] Chang, Y. R., Lee, H. Y., Chen, K., Chang, C. C., Tsai, D. S., Fu, C. C., Lim, T. S., Tzeng, Y. K., Fang, C. Y., Han, C. C., Chang, H. C., and Fann, W. *Mass production and dynamic imaging of fluorescent nanodiamonds.* Nature Nanotechnology, **3**(2008)(5):284–288.

[100] Boudou, J. P., Curmi, P. A., Jelezko, F., Wrachtrup, J., Aubert, P., Sennour, M., Balasubramanian, G., Reuter, R., Thorel, A., and Gaffet, E. *High yield fabrication of fluorescent nanodiamonds.* Nanotechnology, **20**(2009)(35).

[101] Krüger, A., Liang, Y. J., Jarre, G., and Stegk, J. *Surface functionalisation of detonation diamond suitable for biological applications.* Journal of Materials Chemistry, **16**(2006)(24):2322–2328.

[102] Krüger, A., Stegk, J., Liang, Y. J., Lu, L., and Jarre, G. *Biotinylated nanodiamond: Simple and efficient functionalization of detonation diamond.* Langmuir, **24**(2008)(8):4200–4204.

[103] Staudt, T., Lang, M., Medda, R., Engelhardt, J., and Hell, S. W. *2,2-Thiodiethanol: a new water soluble mounting medium for high resolution optical microscopy.* Microscopy Research and Technique, **70**(2007):1–9.

[104] Rittweger, E., Han, K. Y., Irvine, S. E., Eggeling, C., and Hell, S. W. *STED microscopy reveals color centers with nanometric resolution.* Nature Photonics, (2009):144–147.

[105] Richardson, W. H. *Bayesian-based iterative method of image restoration.* Journal of the Optical Society of America, **62**(1972):55–59.

[106] Harke, B., Keller, J., Ullal, C. K., Westphal, V., Schoenle, A., and Hell, S. W. *Resolution scaling in STED microscopy.* Optics Express, **16**(2008)(6):4154–4162.

[107] Wilmshurst, T. H. *Signal recovery from noise in electronic instrumentation.* Adam Hilger, Bristol and Boston 1985.

[108] Pradhan, N., Battaglia, D. M., Liu, Y. C., and Peng, X. G. *Efficient, stable, small, and water-soluble doped ZnSe nanocrystal emitters as non-cadmium biomedical labels.* Nano Letters, **7**(2007)(2):312–317.

[109] Peterson, O. G. *Methods of experimental physics*, volume 15, Part A. Academic Press, New York 1979.

List of publications

1. E. Rittweger, B. R. Rankin, V. Westphal, S. W. Hell, *Fluorescence depletion mechanisms in super-resolving STED microscopy*, Chemical Physics Letters **442**, 483-487 (2007)

2. E. Rittweger, K. Y. Han, S. E. Irvine, C. Eggeling, S. W. Hell, *STED microscopy reveals crystal colour centres with nanometric resolution* Nature Photonics **3**, 144-147 (2009)

3. E. Rittweger, D. Wildanger, S. W. Hell, *Far-field fluorescence nanoscopy of diamond color centers by ground state depletion* European Physics Letters **86**, 14001-p1 - 14001-p6 (2009)

4. S. Irvine, T. Staudt, E. Rittweger, J. Engelhardt, S. W. Hell, *Direct Light-Driven Modulation of Luminescence from Mn-Doped ZnSe Quantum Dots* Angewante Chemie **47**, 2685-2688 (2008)

5. D. Wildanger, E. Rittweger, L. Kastrup, S. W. Hell, *STED microscopy with a supercontinuum laser source* Optics Express **16**, 9614 - 9621 (2008)

6. K. Y. Han, K. I. Willig, E. Rittweger, F. Jelezko, C. Eggeling, S. W. Hell, *Three-Dimensional Stimulated Emission Depletion Microscopy of Nitrogen-Vacancy Centers in Diamond Using Continuous-Wave Light* Nano Letters **9**, 3323 - 3329 (2009)

7. S. W. Hell, E. Rittweger, *Light from the dark* Nature **461**, 1069-1070 (2009)

Acknowledgments

I would like to thank all people who contributed in one way or the other to the success of this work:

Prof. Stefan W. Hell for the opportunity to work in this very interesting and interdisciplinary field and for providing an outstanding working environment. He contributed to this thesis with many discussions and fruitful ideas.

Prof. J. Wolfrum for his interest in my work and for being the second referee of this thesis.

Dr. Volker Westphal for his assistance during my first years and his expert knowledge on electronics.

Brian Rankin for his collaboration during the pump-probe measurements and being a kind lab partner.

Dr. Scott Irvine for working with me on STED experiments as well as the Q-Dot study and for his sense of humor.

Kyu Young Han for the possibility to use his setup for parts of the spectroscopy and for being a part of the diamond "family".

Dominik Wildanger for his collaboration on the GSD measurements and for making the time in the laboratory very enjoyable.

Dr. Lars Kastrup, Dr. Christian Eggeling and Dr. Jan Keller for many valuable discussions and supplying data analysis software.

André Stiel and Rebecca Medda for providing the biological samples.

Dr. Fedor Jelezko for kindly providing the CVD diamond samples.

Dr. Andreas Schönle for the lab software "Imspector".

Dr. Jan Keller, Rebecca Medda, Jaydev Jethwa for kindly proof-reading the manuscript and their helpful comments.

Our great mechanical and optical workshops for manufacturing numerous components for the different setups.

All my colleagues from the NanoBiophotonics department for creating an enjoyable atmosphere both within and outside the lab.

My fiancé Bastian for our partnership as well as his moral support and encouragement.

My parents for their constant support without any ifs and buts.